Plasmonics in Metal Insulator Cavities

Thesis by

Lyuye Lin

In Partial Fulfillment of the

Requirements for the Degree of

Istituto Italiano di Tecnologia (IIT), Genova

Dipartimento di Chimica e Chimica Industriale (DCCI),

Università Degli Studi Di Genova, Genova

2021

Supervised By:

Prof. Roman Krahne, Prof. Remo Proietti Zaccaria (Istituto Italiano di Tecnologia)

Prof. Marina Giordano (Università Degli Studi Di Genova)

Abstract

Subwavelength multilayer metal-insulator nanostructures with tuneable resonances have been widely used for various applications in optoelectronics and photonics, due to their unique dispersion relation of the dielectric permittivity. In this thesis, we firstly studied the optical properties and the resonance modes of the metal/insulator/metal (MIM) metamaterial system by spectroscopic ellipsometry and COMSOL Multiphysics calculations based on finite element methods. Our calculation results show that MIM systems with vertical or lateral gratings can both support the multiple cavity modes that form the epsilon-near-zero (ENZ) resonance with an effective dielectric constant close to zero. Their large local density states are beneficial to the Purcell effect enhancement of the spontaneous emission. Moreover, the low-energy multi-cavity modes can be adjusted in the visible range via tuning the insulator thickness. The difference is that the MIM system with lateral grating leads to uncoupled multiple ENZ resonance, while the vertical grating MIM structure owns strongly coupled modes which form ENZ bands.

To demonstrate the usefulness of the emission enhancement of MIM structures in practical applications, multilayer metal-insulator nanostructures are adopted to improve the spontaneous emission of the emitter. Herein, we explored the effects of interface modifications on the overall performance in perovskite LEDs. Firstly, we designed and optimized the flat perovskite LED (PeLED) through systematic analysis of the power loss channels based on the optical mode. All the theoretical analysis is carried out through finite element simulations. Under the assumption of efficient photon generation in the emitting layer with an internal quantum yield of 0.9, the effect of the dipole orientation is analyzed and then thickness of the charge injection and emitter layer was optimized. Finally, we tuned the transparent electrode thickness to get the maximum value of the external quantum efficiency. Moreover, we further studied the influence of

interface modifications happening at the electron-transport interface on the whole performance of perovskite-based flat PeLEDs. Particularly, we explored the integrating of photonic structure, while keeping the optical property of the emitting material. Interesting, our calculations reveal that the specially designed nanopatterning can promote to improve the Purcell factor and the outcoupling efficiency, thereby enhance the external quantum efficiency, related to the nanopattern-free PeLED configuration. In particular, an average enhancement around 100% for the external quantum efficiency was achieved, and thus improving the radiative emission of the PeLED devices. These findings indicated that using morphological patterning to enhance LED performance is realistic method, similar to other light emission technologies.

Finally, a nanoscale optical pressure/temperature nano sensor based on gap-plasmonic nanostructure, composing of the MIM nanopillar arrays covered by a metallic film, is proposed. The gap plasmon frequency is highly sensitive to the distance of the pillars to the Ag film, which allows optical sensing of pressure/ambient temperature/ refractive-index by variation in the colour of the device.

Acknowledgements

I would like to take this opportunity to express my gratitude to those who helped me in various aspects of conducting research and writing this thesis. Without their support and help, this thesis would be impossible to complete.

First of all, I take immense pleasure in thanking my project supervisor professor Roman Krahne for his generosity, friendliness and support all throughout my PhD. At the same time, I am grateful for all the trust, guidance, and freedom. Your enthusiasm for science and your openness to new ideas and perspectives are admirable, as they enable the team to solve every new problem with a vibrant and diverse background and perspectives. So, thank you again for letting me be a member of this wonderful group.

I would like to express my sincere gratitude to my co-tutor professor Remo Proietti Zaccaria for his patient guidance and friendly help in life and scientific works over the past several years. Because of your valuable and effective advice on my research and moral support during my research period, I didn't quit the present work and life here. It was you who picked me up in the airport and helped me find a flat when I first arrived in Italy. You explained a lot about Italian life to me. It was you who offered me valuable opinions about my work, and taught me how to fix the problem. In particular, your encouragement gives me the courage and confidence to face and solve the problems in life and work, every time I start to doubt my ability. Words can't describe how thankful I am. Here, I could only express my gratitude to you with the weak language, thank you for your timely and effective advice during the determination and progress of my research period, thank you for your patient guidance on my writing, I have learned a lot and also develop myself deeply these years.

I would like to thank Dr. Vincenzo Caligiuri for his guidance on the MIM system, Dr. Venkata Naga Sri Renuka Devi Pothuraju for her support on the experiment data of the MIM project. Moreover, I want to express my gratitude to Dr. Fang Chen, thank Dr. Giulia Biff, Dr. Giulia Bruno, Dr. Nadia Pinton, Aniket Patra for their support in the experiment throughout my research on LED.

I am very grateful to Dr. Yingqi Zhao, Dr. Jianan huanng, Dr. Tao Li, Dr. Gaofeng Li, Dr. Xinyuan Zhao, Dr. Mengjiao Wang for motivating me to strive towards my goals,

sharing experiments on research and helping me in life.

I want to thank my husband Dr. Zhifu Feng, for his support and help. In particular, he encouraged me every time I couldn’t stick to it and doubted myself, and helped me tide over the difficulties.

I would also like to thank my family for their support and understanding.

Content

List of Figures

List of Tables

List of Publications

Journal Papers

1. Lin, L.; Proietti Zaccaria, R.; Garoli, D.; Krahne, R. Photonic Cavity Effects for Enhanced Efficiency in Layered Perovskite-Based Light-Emitting Diodes. *Nanomaterials* **2021**, *11*, 2947.

2. Lin, L.; Krahne, R.; Proietti Zaccaria, R. Effect of multilayer nanopatterning in Perovskite Light-Emitting Diodes. (Under review).

Conference Papers

1. L. Lin and R. Krahne. Nanoscale Optical Sensors Based on Gap-Plasmonic Nanostructure. *2021 Fifteenth International Congress on Artificial Materials for Novel Wave Phenomena (Metamaterials)*, 2021, 229-231.

2. L. Lin; R. D. Pothuraju; G. Biffi; R. Proietti Zaccaria; A. De Luca; V. Caligiuri; R. Krahne. Multiple-Metal/Insulator/Metal Cavities as a Platform to Design Epsilon-Near-Zero Resonances. *2020 fourth International Congress on Artificial Materials for Novel Wave Phenomena (Metamaterials)*, 2020.

3. Renuka Devi Pothuraju, Lyuye Lin and Roman Krahne. Microstructuring of Metal-Insulator-Metal nanocavities for spatial Epsilon-Near-Zero response. European Optical Society Annual meeting (EOSAM), 2021.

Chapter 1: Introduction

1.1 Photonic and plasmonic systems for spontaneous emission enhancement

Colloidal semiconductor nanocrystals (NCs) are fascinating optical materials with many attractive characteristics, such as widely adjustable emission wavelength [1], high photoluminescence quantum yield (PLQY) [2,3] and narrow emission spectral bandwidth [4], which depend on the nanocrystal size, shape, and chemical composition in solution. Moreover, the low-cost solution-based fabrication and processing of NCs is also suitable for lightweight and flexible materials [5,6]. Thanks to these unique features, NCs provide a plethora of potential device applications, including light emitting diodes [6-9], continuous lasing [10], solar concentrators [11,12], photodetectors [13,14] and photovoltaic devices [15,16]. Moreover, colloidal quantum dots are primarily specified as a gain material due to their high near-unity quantum yield, large transition dipole moments, strong photostability, and ability to form densely uniform films without impacting the self-quenching phenomena noticed in organic dyes. In the colloidal semiconductor nanocrystal, metal halide perovskites (MHP) with the normal chemical formula ABX3, where A is designated as a monovalent inorganic or organic cation, e.g., Cs, B is referred to as a bivalent metal cation such as Pb2+ and Sn2+, and X is a halide anion, e.g., Cl- and Br-, have appeared as highly promising materials due to their novel optical and electronic properties, and their narrow emission spectrum (full-width at half-maximum (FWHM is around 22 nm) allows them to achieve high colour purity, high brightness, wide bandgap tunability and easy solution-processing capability [17,18]. In the all-inorganic MHP, CsPbBr3 has been widely utilized because of its excellent optical characteristics and green emission scalability [19]. The crystal structure and optical characteristics of the most often investigated lead

bromide-based perovskite are shown in Figure 1.1. Together with attractive optical and electrical features, CsPbBr3 has broadband absorption properties that are especially attractive to the plasmonic community, where coupling the resonant mode of a plasmonic cavity to an emitter's absorbance improves energy transfer, i.e., surface plasmon enhanced absorption (SPEA). Therefore, we adopted the colloidal semiconductor nanocrystal CsPbBr3 as the light emitter to study the photonic cavity effect on the emission efficiency enhancement of the layered perovskite light-emitting diodes and how to take advantage of the photonic nanostructures to enhance the perovskite LED performance.

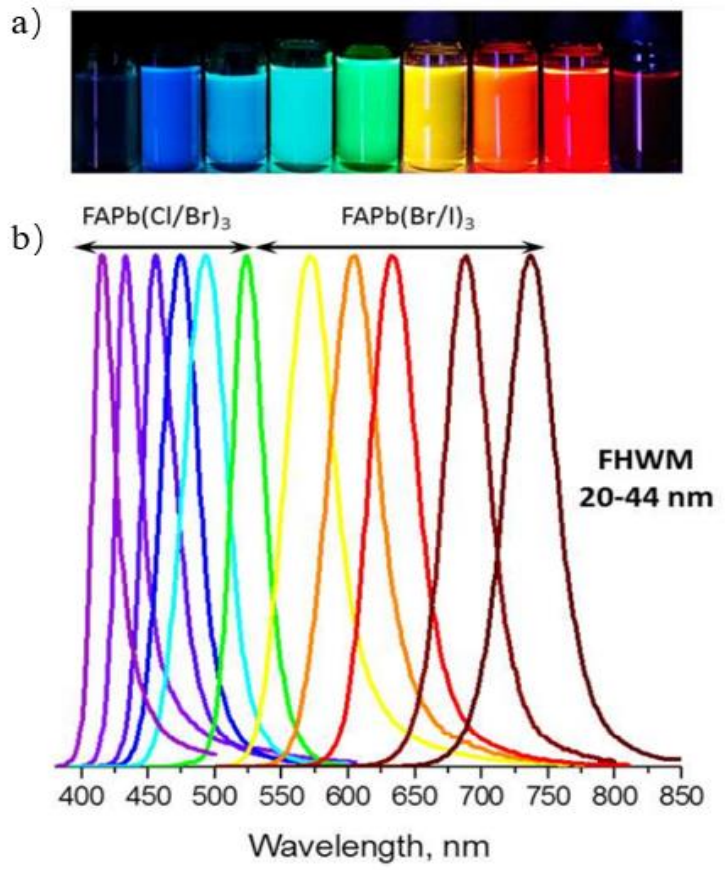

Figure 1.1 a) Digital picture of colloidal solution in toluene taken under UV-light (λ=365 nm). b) Compositional tuning of the PL spectra of the mixed halide NCs (reprinted with permission from ref. [19]. Copyright © 2017, American Chemical Society)

1.1.1 Surface plasmon polaritons

Surface plasmon polaritons (SPPs), excited by light with sufficient momentum matching, are the collective oscillations of conduction electrons at the metal-dielectric interface, whose wavelength is significantly shorter than that of the corresponding photon in free space. SPPs are categorized into two types: localized surface plasmon resonances (LSPRs) and propagating surface plasmon polaritons (SPPs). Figure 1.2a illustrates a classical example of the LSPR based on nanoparticles. When an electromagnetic (EM) wave can propagate along the surface of a metal until energy is lost either through absorption in the material or through radiation into free space, it is a typical propagating surface plasmon polaritons, and the electromagnetic energy and the kinetic energy of unbound electrons contribute to the energy of the following SPP wave, as depicted in Figure 1.2b (left). SPP is spatially confined to the metal-dielectric interface and propagates parallel to the metal-dielectric contact (in Fig.1.2b in the y direction). In these two media, SPP decays evanescently in the direction perpendicular to the interface as illustrated in Figure1.2b (right). The Coulomb interaction between the displaced electrons and the positively charged atomic nucleus further triggers the electron cloud resonance. These two surface plasmon modes provide dramatically increased electromagnetic fields on metal surfaces and have been widely applied in various applications, namely surface enhanced Raman spectroscopy [20,21], hyperthermia [22], biosensors [23] and light controlled medication release [24] just to name a few.

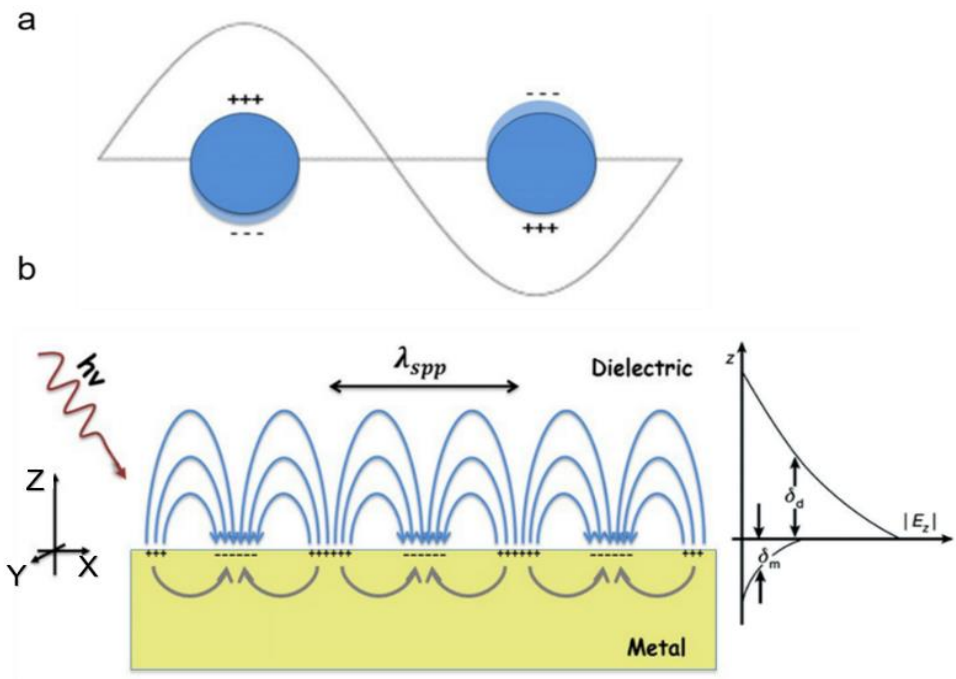

Figure 1.2 Schematic diagrams illustrating (a) the localized surface plasmon and (b) the surface plasmon polaritons: Propagation of SPPs in the x-direction along the metal-dielectric interface(left), and Evanescent field (right) of SPPs (reprinted with permission from ref. (25) Copyright © 2019 The Authors. Published by Elsevier B.V.).

1.1.1.1 SPP at single metal-insulator interface

Figure 1.3 shows the diagram of the SPP propagation at the metal-insulator interface. The dielectric medium 1 occupies half the space (x > 0, insulator) with a positive dielectric constant (ε_d), whereas the conducting medium 2 (x < 0, metal) has a frequency-dependent dielectric constant (ε_m). To analyse the physical characteristics of surface plasmon polaritons, it is necessary to use Maxwell's equation. Without external charge and current densities, Maxwell's equation becomes:

$$\nabla \times \nabla \times E = -\mu_0 \frac{d^2 D}{dt^2} \tag{1.1}$$

As presented in Figure 1.2, the SPP wave propagates in the x-direction and attenuates in the z-direction, and the electric and magnetic fields do not depend on the y components. Derived from Maxwell's Equations, the electric and magnetic fields of an

SPP are spatially and temporally dependent as follows:

$$E = \mathrm{E(X)}e^{-i\omega t + ik_x X - k_{1,2}|Z|} \tag{1.2}$$

$$H = H(X)e^{-i\omega t + ik_x X - k_{1,2}|Z|} \tag{1.3}$$

Where, E(X) and H(X) are the electric field vector and magnetic field vector, ω is the angular frequency of the wave, k_x is the wave vector along the z direction.

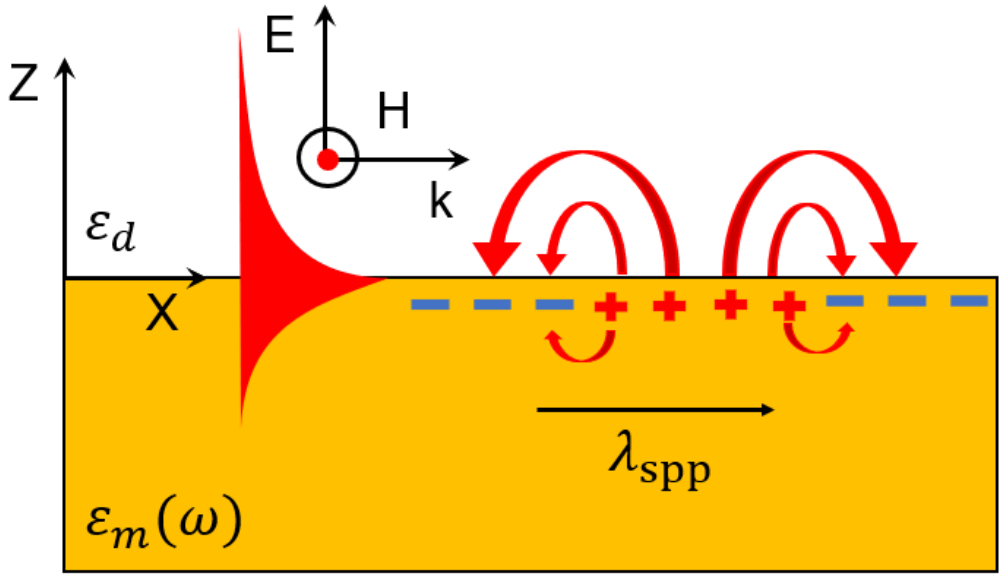

Figure 1.3 SPP at the metal-insulator interface.

The field distribution and dispersion relations, i.e., the frequency dependence of the propagation constant k_x, are determined by solving Maxwell's equations in both mediums. In the case of TM-polarized light (p-polarized), it is feasible to demonstrate that non-trivial solutions are produced in the presence of a non-magnetic medium. However, trivial solutions are achieved for TE polarization. By applying boundary conditions and ensuring the continuity of the electric field, the following condition is discovered:

$$\frac{k_1}{\varepsilon_d} + \frac{k_2}{\varepsilon_m} = 0 \tag{1.4}$$

Here, k_1 and k_2 denote the inverse penetration depths in mediums 1 and 2, individually.

$$k_{1,2} = \sqrt{k_x^2 - \varepsilon_{d,m}\frac{\omega^2}{c^2}} \tag{1.5}$$

Due to the fact that the inverse penetration depths are positive, the above equation can be solved only when one of the dielectric constants ε_d or ε_m is negative. It can be simplified to by exchanging the values of k_1 and k_2 in equation 1.4.

$$\frac{\sqrt{k_x^2 - \varepsilon_d\frac{\omega^2}{c^2}}}{\varepsilon_m} + \frac{\sqrt{k_x^2 - \varepsilon_d\frac{\omega^2}{c^2}}}{\varepsilon_d} = 0 \tag{1.6}$$

After solving the equation, the condition for the existence of SPP is found to be $\varepsilon_d\varepsilon_m < 0$. The preceding equation is solved in terms of k_x, and the following result is obtained.

$$k_x = \frac{\omega}{c}\sqrt{\frac{\varepsilon_d\varepsilon_m}{\varepsilon_d + \varepsilon_m}} \tag{1.7}$$

Equation 1.7 is referred to as the dispersion equation of the SPP wave propagating at the metal-insulator interface. As we know from equations 1.2 and 1.3, the field of one surface electromagnetic wave decays exponentially in both medium. If the values of k_1 and k_2 are both real and positive, their squared values are also positive. But if k_x is negative, the exponentially decaying wave becomes a propagating wave. The frequency-dependent dielectric constant of the metal is denoted by

$$\varepsilon_m = \varepsilon_{m\infty} - \frac{\omega_p^2}{\omega^2} \tag{1.8}$$

Here, ω_p the resonance frequency of free electron cloud called plasma, $\varepsilon_{m\infty}$ is the dielectric constant of the metal, which is a measure of the dielectric constant as the concentration of free electrons approaches zero.

Substituting the value of k_2 simplifies the equation 1.5 to the following expression:

$$k_2^2 = k_x^2 - \varepsilon_{m\infty}\frac{\omega^2}{c^2} + \frac{\omega_p^2}{c^2} \tag{1.9}$$

According to k_1^2 and k_2^2, the dispersion plane is split into three sections based on the behaviour of the electromagnetic wave, whether they are propagating or exponentially decaying, as the dash line shown in Figure 1.3. Because the frequency in this region is higher than the plasma frequency, waves can propagate inside the metal layer due to its

dielectric characteristics. In the area 2, all waves propagate, exhibiting wave propagation in dielectric and exponential behaviour in metal. However, the waves are entirely exponential in zone 3, which indicates that any surface wave dispersion should be confined here. Figure 1.4 illustrates the propagating properties of the SPP at various frequencies. Because SPPs lack a cut-off frequency, they cannot propagate at low frequencies. Thus, SPP can be applied in the visible, infrared, and terahertz regions. At lower frequencies, SPP's asymptote is linear at lower frequencies, while the propagation constant increases rapidly and tends to infinity at some point at higher frequencies. This frequency is referred to as the resonant frequency of the Surface Plasmon Polariton, abbreviated as SPP. However, due to the momentum mismatch, SPP cannot be initiated at the flat metal-insulator interface using a free space photon. The momentum of the photon has to be increased in order to couple it to the SPP. To date, numerous phase matching approaches, such as prism coupling, grating coupling, and excitation through highly focused optical beams, have been developed in order to circumvent this issue.

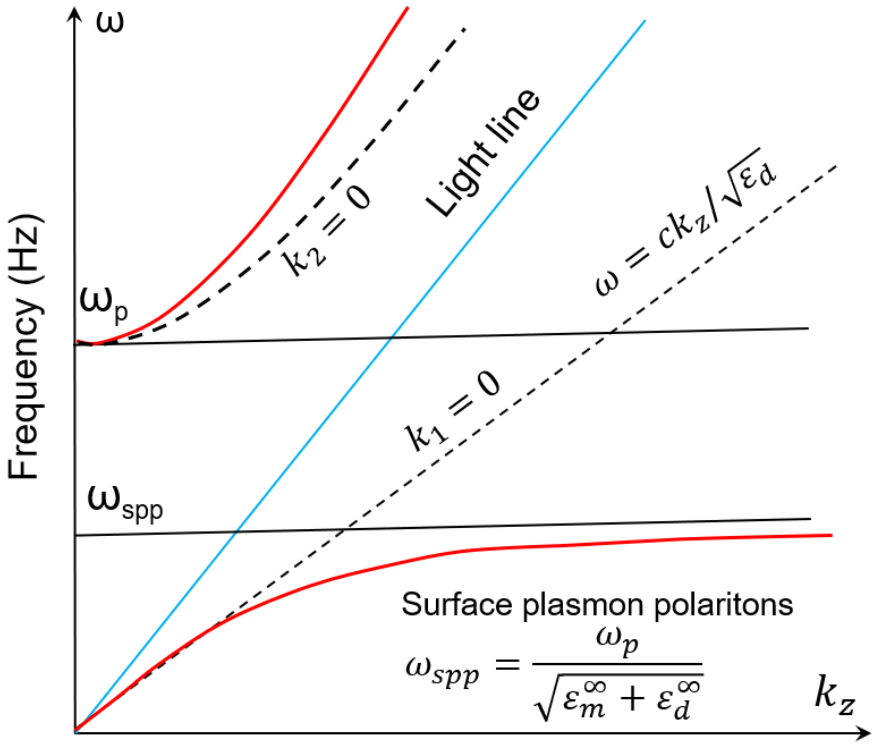

Figure 1.4 Dispersion curve of SPPs at the metal-dielectric interface.

1.1.1.2 Multiple Metal-Insulator Interface

In the metal-insulator multilayer system, SPPs are excited at each interface. But SPPs eventually dissipate after propagating a very short distance (approximately a few meters m), due to the high ohmic losses of metal. SPPs are formed at two interfaces as a result of constructive and destructive interference between modes. The SPPs will couple when the insulating layer is thin enough, resulting in coupling gap SPPs (GSPPs), which are helpful in applications using optical integrated circuits, as shown in Figure 1.5. Numerous metal-insulator configurations fall into two broad categories: insulator-metal-insulator (IMI) waveguides and metal-insulator-metal (MIM) waveguides (MIM). In this thesis, we are only interested in the lowest-order boundary modes given by the TM modes in the MIM system, which are non-oscillating in the z direction, that is, perpendicular to the surface. SPP mode coupling completely depends on the insulator layer thickness. SPP modes propagate freely at the metal-insulator interfaces with a thick enough insulator, and the gap SPP mode is only formed by two SPP modes as the insulator layer become thin. The MIM waveguide has a symmetrical and asymmetrical distribution of the transverse and longitudinal components of the electric field. Plasmonic slot waveguides are MIM waveguides with the above field distribution. The dispersion relation for the plasmonic mode is given by

$$\tanh\left(k_{z,d}\frac{t}{2}\right) = \frac{\varepsilon_d k_{z,m}}{\varepsilon_m k_{z,d}} \tag{1.10}$$

$$k_{z,m(d)}^2 = k_{G-SPP}^2 - \varepsilon_{m(d)} k_0^2 \tag{1.11}$$

Here, $k_{z,m(d)} = \sqrt{k_{G-SPP}^2 - \varepsilon_{m(d)} k_0^2}$ and k_{G_spp} denotes the propagation constant for waves in a plasmonic slot waveguide. With a thinner insulator layer, the propagation length of the GSPP mode is significantly increased, and there are subwavelength lateral restrictions [26]. Therefore, insulator thickness affects the propagation length and electric field distribution of the SPP in the MIM system.

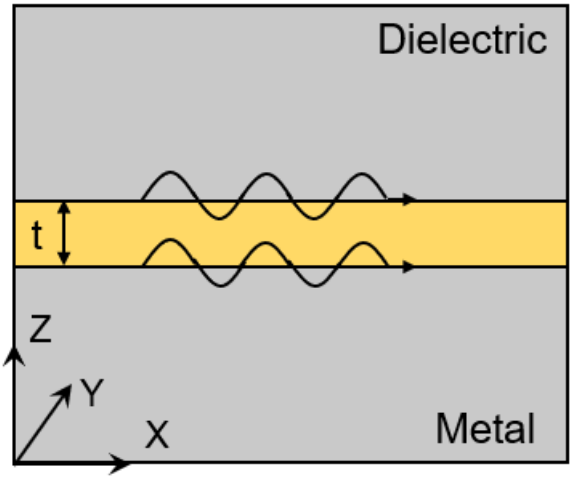

Figure 1.5 SPP excitation in the multilayer structure with thin metal layer embedded between dielectric mediums.

1.1.2 Epsilon Near Zero (ENZ) Mode

Metal films with a thickness thinner than the skin depth can sustain the surface plasmon mode, and its dispersion relationship is close to the plasma frequency, resulting in the being ε is close to zero, namely the ENZ mode. However, ENZ modes are constrained and their dispersion relationship is on the right side of the light line, which can be excited by Kretschmann geometry or grating couplers. However, before Campione and his colleagues [27], there is no clear theoretical description of these modes and the long-range surface properties of these modes. From the red dotted line in Figure 1.6, which shows the ENZ modes in lots of oxides, doped semiconductors, and polar materials, and not in the metals, because of the mismatch between the plasma wavelength and the thickness, ENZ mode may be induced in thin metals below the skin depth. And in the research of Dr. Caligiuri and his colleagues [28], it has been confirmed that the ENZ resonance in the visible light range can be obtained by tuning the MIM film structure. In this work, we utilize spectroscopic ellipsometry achieve the dielectric constant of the complex metal-insulator system, thereby analysing the ENZ cavity modes in the metal-insulator system.

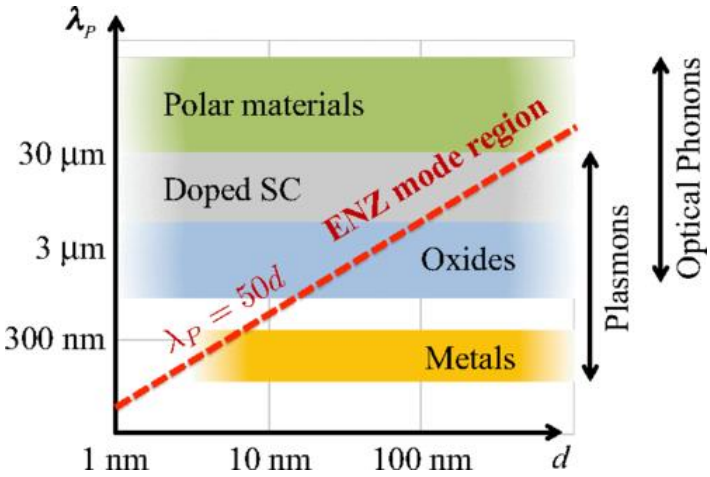

Figure 1.6 Classification of material systems that may support ENZ modes, obtained by mapping the plasma wavelength λ vs. thin layer thickness d (reprinted with permission from ref.27©2015 American Physical Society).

1.1.2.1 Spectroscopic Ellipsometry

Spectroscopic ellipsometry is the primary technique to investigate the optical characteristics of a variety of systems, including plain thin films, multilayer nanostructures, and more complicated systems. Since it was first introduced by Paul Drude in the 19th century [29], ellipsometry has attracted great attention after confirming that it can offer nanoscale sensitivity in the micro/nano electronics field, and its application spans from fundamental science in physical sciences to micro/nano electronics [30], biosensors [31], communication [32], to mention a few. At present, two commercial J. A. Woollam M-2000 ellipsometers covering the wavelength ranges of 210–1000 nm and 370–1690 nm at various angles is very widespread [33]. In our work, spectroscopic ellipsometry is primarily utilized to measure the optical dielectric constant of thin layers and to retrieve the effective dielectric constant of complex structures like epsilon-near-zero multilayer metal-insulator nanostructures (ENZ HMMs).

1.1.2.2.1 Basic principle

The measured signal is the polarization fluctuation caused by the interaction of the light source with the sample (reflection, absorption, scattering, or transmission). The amplitude ratio (Ψ) and the phase shift (Δ) are often used to evaluate the polarization alteration. Due to the fact that the measured approach is based on the optical properties and thickness of specific materials, the ellipsometer (as shown in Figure 1.7) can be used for non-contact measurements of film thickness and optical constants.

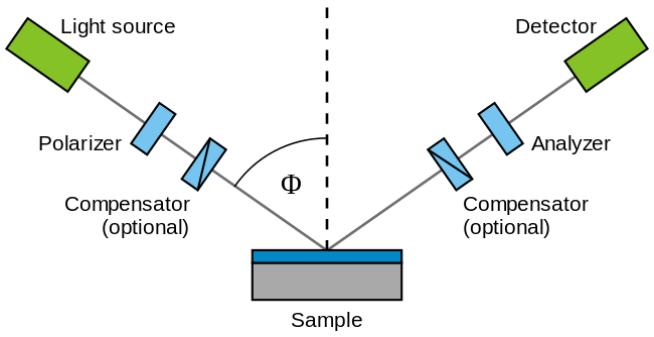

Figure 1.7 Schematic of the ellipsometer (reprinted with permission from ref. (34) Copyright ©2015 American Physical Society).

1.1.2.2.2 Fundamental equation of ellipsometry

In general, the ellipsometer measures two quantities: the amplitude component Ψ and the phase shift Δ, to evaluate the polarization change of the light reflected or transmitted from a system or material. The complex reflection ratio ρ(complex quantity) of a system can be calculated by the amplitude component Ψ and the phase shift Δ, which can also be expressed as the ratio between complex Fresnel reflection coefficients in the p-polarized and s-polarized wave (as shown in Figure 1.8):

$$\rho = \frac{r_p}{r_s} = \tan(\Psi)e^{i\Delta} \tag{1.12}$$

$$\Delta = \Delta_p - \Delta_s \tag{1.13}$$

$$tan\Psi = \frac{|r_p|}{|r_s|} \tag{1.14}$$

Where Δ is the phase shift of the p- and s-waves caused by the reflection, with one value ranging from 0 to 360 (or alternatively, from-180 to 180). The Ψ has a tangent equal to the magnitude of the sample's complex reflection coefficients in the p-to s-direction. The approach is used to investigate the optical property of metal-insulator multilayer systems such as MIMIM planar, MIM nanopillars, and MIM grating in this work.

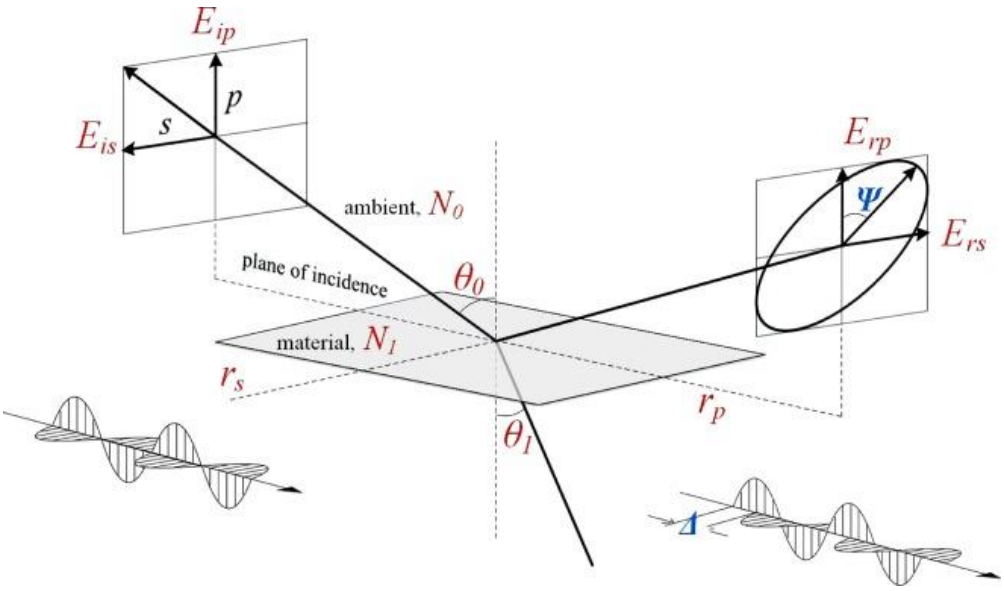

Figure 1.8 A sample ellipsometry measurement (reprinted with permission from ref. (35)).

1.1.3 Spontaneous emission

Spontaneous emission [36] is a process by which a quantum system transitions from an excited state with energy E2 to a lower state with energy E1 (e. g., the ground state), emitting energy in the form of photons, which have angular frequency ω and energy $\hbar\omega$, as shown in Figure 1.9.

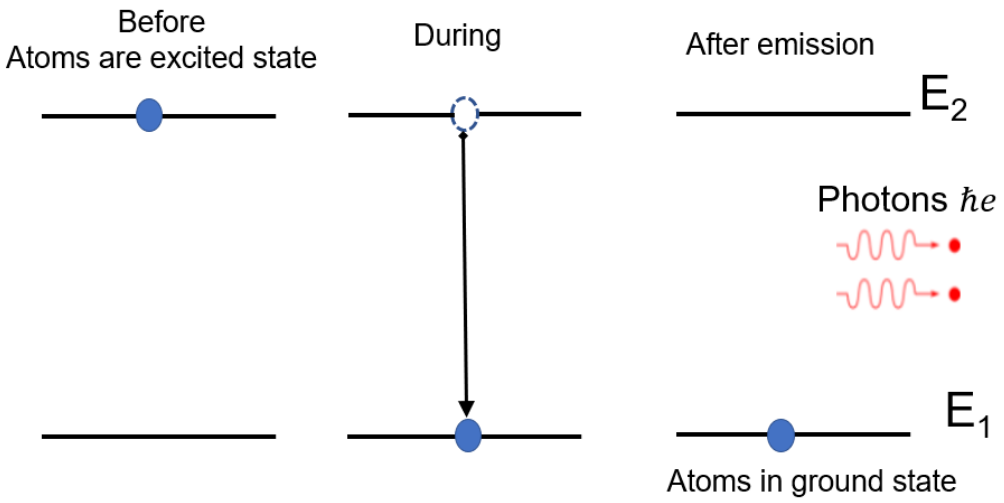

Figure 1.9 An energy level diagram illustrating the process of spontaneous emission.

Depending on how the excitons are generated (electroluminescence, chemiluminescence, etc.), there are different forms of luminescence, such as fluorescence and phosphorescence, which are mainly distinguished by the decay time and their decay time of phosphorescence is much longer than fluorescence. Figure 1.10 illustrates the energy levels, excitation, and relaxation processes of a fluorescent molecule [37]. Excited states and ground states have various energies, which are determined by the equation: $E = \hbar\omega$, where $\hbar$ is the reduced Planck constant and ω is the photon frequency. For a fluorescent molecule, the minimum energy required to excite an electron from a ground state (E_0) to an excited state (E_1) is ΔE. This energy can be attained through light and the transfer of the electron from the ground to excited states. First of all, in the same electronic band, the electron undergoes vibrational relaxation to the lowest level, in which it achieves the singlet state via internal conversion and vibrational relaxation. Internal conversion is a non-radiative process, indicated in Figure 1.10 by one blue dashed arrow, which happens between two identical spin states. As shown in Figure 1.10, the light of a certain wavelength (the upward vertical arrow) is absorbed and excites from the ground state to the excited state

(S0 →S1, S2), while the vibrational relaxation of the electronic state and electromagnetic energy are represented by red and green/blue descending arrows, respectively. And these two transitions are called fluorescence and phosphorescence. In this thesis, CsPbBr3 nanocrystals are used as fluorescent materials to study the spontaneous emission enhancement effect in the plasmonic system.

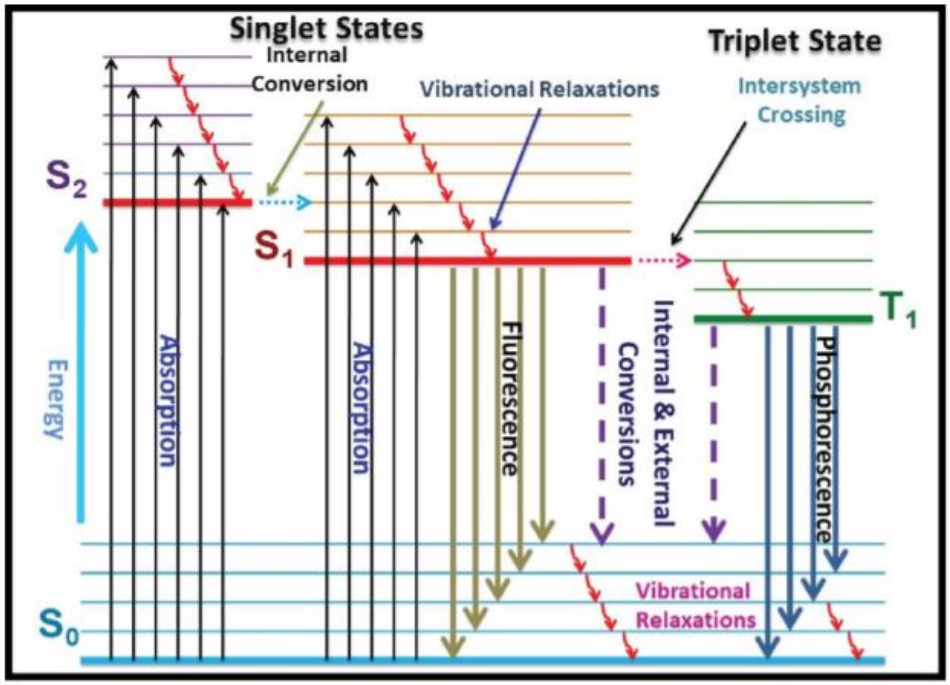

Figure 1.10 Schematics of Jablonski Diagram (reprinted with permission from ref. [37] copyright@optica.org.).

1.1.4 Theoretical calculation of Purcell effect

In the free space, the spontaneous emission is called the inherent radiation characteristic of the fluorophore. If the environment of the quantum system (e. g., dye molecules, quantum dots, etc.) is changed, also their spontaneous emission rate is enhanced. This effect is known as “Purcell effect” [38, 39, 40]. In the past, various approaches were used to achieve the spontaneous emission enhancement of the fluorophore, such as through the employment of spherical cavities, periodic metal-dielectric structures and

plasmonic nanoantenna. One of the most commonly approaches to obtain the Purcell effect is to manipulate the spontaneous emission rate of the dipole emitter in coupled plasmonic modes. [41]. In general, this phenomenon is governed by two mechanisms: surface plasmon enhanced absorption (SPEA) [42] and surface plasmon coupled emission (SPCE) [43]. The former relates to the possibility of increasing the fluorophore's absorbance via a plasmonic absorber, whereas the latter refers to increasing its emission through the resonant characteristics of a plasmonic structure performing as a cavity. This is because the Purcell factor quantifies the enhancement due to the Purcell effect. And then this comes from the combined emitter-environment system.

In the homogeneous dielectric environment, the decay rate for the fluorophore is calculated by the Larmor equation:

$$\Gamma_0 = |\mu|^2 \sqrt{\varepsilon_1}\omega^3/3hc^3 \tag{1.15}$$

Here μ represents the electric dipole moment, ω is the emission angular frequency, and ε_1 is the permittivity for the host material. When the emitting dipole is situated at a distance (d) above the metal layer perpendicular or parallel to the interface, the related Purcell Factor (PF) can be stated as [44, 45]:

$$PF_{\perp} = 1 - \eta_0 + \frac{3}{2}\eta_0 Re \int_0^{\infty} dk_x \frac{1}{k_z}\left(\frac{k_x}{\sqrt{\varepsilon_1}k_0}\right)^3 \left[1 + r_p e^{2ik_z d}\right] \tag{1.16}$$

$$PF_{\parallel} = 1 - \eta_0 + \frac{3}{4}\eta_0 Re \int_0^{\infty} dk_x \frac{1}{k_z}\frac{k_x}{\sqrt{\varepsilon_1}k_0}\left\{1 + r_s e^{2ik_z d} + \frac{k_z^2}{\varepsilon_1 k_0^2}\left[1 - r_p e^{2ik_z d}\right]\right\} \tag{1.17}$$

Where η_0, the internal quantum efficiency of the fluorophore in homogeneous dielectric environment, is close to 1; k_x and k_z denotes the wavevector component parallel or perpendicular to the interface. k_0 represent the magnitude of the wavevector in vacuum. $r_{p,s}$ is the reflection coefficient at the interface for p-polarized or s-polarized wave, respectively. For multilayer substrates, the reflection coefficient $r_{p,s}$must be substituted by that for multilayer interfaces calculated through transfer matrix method [46, 47]. For

isotropic orientation, the average Purcell factor is determined by

$$PF_{iso} = \frac{1}{3}PF_{\perp} + \frac{2}{3}PF_{\parallel} \tag{1.18}$$

The two integrands in Equation (1.16) and (1.17) represent the normalized dissipation power spectra of the dipole emitter's perpendicular and parallel polarizations relative to the dipole's polarization in vacuum [48]. The semi-classical theory is analogous to the quantum mechanics theory in the weak coupling state, where the LDOS enhancement is equivalent to the normalized dipole dissipation power density [49, 50]. The relevant LDOS enhancement is [51],

$$\frac{dP_{\perp}}{du} = \frac{3}{2}\frac{k_0}{k_z}\left(\frac{u}{\sqrt{\epsilon_1}}\right)^3\left[1 + r_p e^{2ik_z d}\right] \tag{1.19}$$

$$\frac{dP_{\parallel}}{du} = \frac{3}{4}\frac{k_0}{k_z}\left(\frac{u}{\sqrt{\epsilon_1}}\right)^3\left\{1 + r_s e^{2ik_z d} + \frac{k_z^2}{\varepsilon_1 k_0^2}\left[1 - r_p e^{2ik_z d}\right]\right\} \tag{1.20}$$

$$u = k_x/k_0\,,\ k_z = k_0\sqrt{\varepsilon_1 - u^2} \tag{1.21}$$

In the range $0 < k_x < k_0$ the normalized dissipated power reflects the contribution of spontaneous emission enhancement to the propagating wave, but in the range higher than$\sqrt{\varepsilon_1}k_0$, both plasmonic modes and other non-radiative components are contained. Only emissions with $k_x < k_{cf}$ can leave the dielectric medium, reaching the far field into a matching observation angle for those propagating waves, k_{cf} is the cutoff wavevector. Measured at the same collecting angle, the radiative enhancement is defined as the ratio of radiative emission from dipole emitters on substrates to those in free space.

$$f_{rad,\perp/\parallel} = Re\int_0^{k_{cf}} dk_x \frac{dP_{\perp/\parallel}}{dk_x} \Big/ \int_0^{k_{cf}} dk_x \frac{dP_0}{dk_x} \tag{1.22}$$

P0 describes the normalized dissipated power for the fluorophore in free space. For isotropic orientation, the average far field radiative enhancement is given by

$$f_{rad,iso} = \frac{1}{3}f_{rad,\perp} + \frac{2}{3}f_{rad,\parallel} \tag{1.23}$$

1.1.5 Electromagnetic simulations of Purcell effect

All the 3D full-wave simulations are fulfilled through the commercial software COMSOL Multiphysics [52], which is based on the finite element method. A hertzian dipole is utilized as the fluorophore in the multilayer system to simulate the light emission of the fluorophore, and the geometry and permittivity of the materials should be the same as in the samples. Integrating power flow through the boundaries provides the total radiated power $P_{i,r}$, the power $P_{i,r,cf}$ under a certain collecting angle into the far field, and the power $P_{i,nr}$ dissipated owing to ohmic loss in the substrate. The Purcell factor and the radiative enhancement can be calculated from simulations with collecting the total power $P_{i,0}$ and the power $P_{i,0,cf}$ within the same collection angle emitted from the same dipole in the absence of cavity substrate:

$$PF_i = 1 - \eta_0 + \eta_0 \frac{P_{i,r}+P_{i,nr}}{P_{i,0}} \ (i = \parallel, \perp) \tag{1.24}$$

$$f_{rad} = \frac{P_{i,r,cf}}{P_{i,0,cf}} \tag{1.25}$$

The simulation results with different dipole orientations should be compatible with the experimental results of the real samples. This full-wave simulation method is not limited to describing the behaviour of uniform substrates, but can also be used for patterned nanostructures.

1.2 Perovskite light emitting diodes

The typical construction of LED devices is constructed of stacked thin films organized in the following sequence: transparent anode/hole transport layer (HTL)/perovskite or emission layer (EML)/electron transport layer (ETL)/cathode, as shown in Figure 1.11 [53]. The hole and electron are injected from the anode and cathode and transported through the transport layers to the emitter layer to recombine. A fraction of the transported electrons and holes combine to generate excitons, emitting photons, whose

energy corresponds to the emitting material's bandgap. To maximize the luminance generated by the PeLED, it is critical to select appropriate materials, such as colloidal nanocrystals with a high quantum yield with materials of transport layers with efficient charge injection and balanced electron and hole transport.

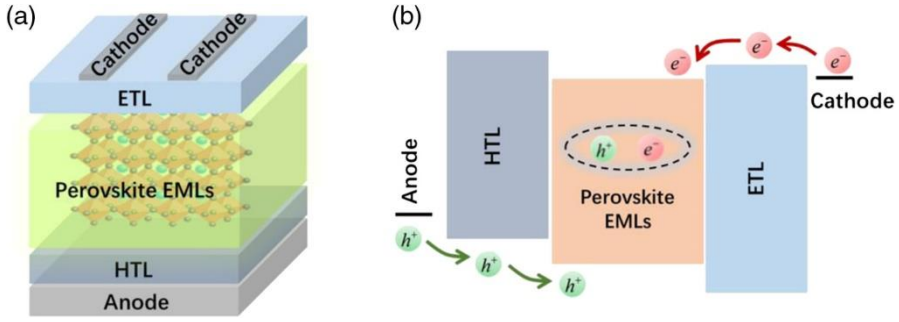

Figure 1.11 (a) Common device structure of p–i–n perovskite LEDs. (b) Carrier injection and transport in p–i–n perovskite LEDs. HTL, hole transport layer; EML, emitting layer; ETL, electron transport layer (reprinted with permission from ref.53, © 2020 Chinese Chemical Society).

In order to design efficient LED devices from an electronic standpoint, the following design rules should be considered: ohmic contact, charge balance, and exciton confinement. However, only a small proportion of light escapes the PeLED device owing to the optically lossy characteristic of an optical microcavity, even at 100% internal efficiency, that is, all injection charge carriers produce photons. Around half of the light emitted is captured by optical modes: such as waveguide modes, surface plasmon polaritons, and absorption [54-56]. Figure 1.12a illustrates the optical structure of an emitting PeLED. The emitted light by the excitons in the EML can be dissipated to surface plasmon polaritons or metal absorption, and it can be confined in the substrate or the PeLED cavity. The optical mode distribution of the PeLED observed in Figure 1.13a is displayed in Figure 1.12b. Because the optical characteristics of PLEDs are determined by the optical interference between the emitter and the metallic reflector,

the distance between the emitter and the metallic reflector is the primary factor affecting optical outcoupling, as shown in Figure 1.12b. In this thesis, to reach the optimum luminous efficiency, we focus specifically on theoretical analysis of the LEDs from a photonic cavity.

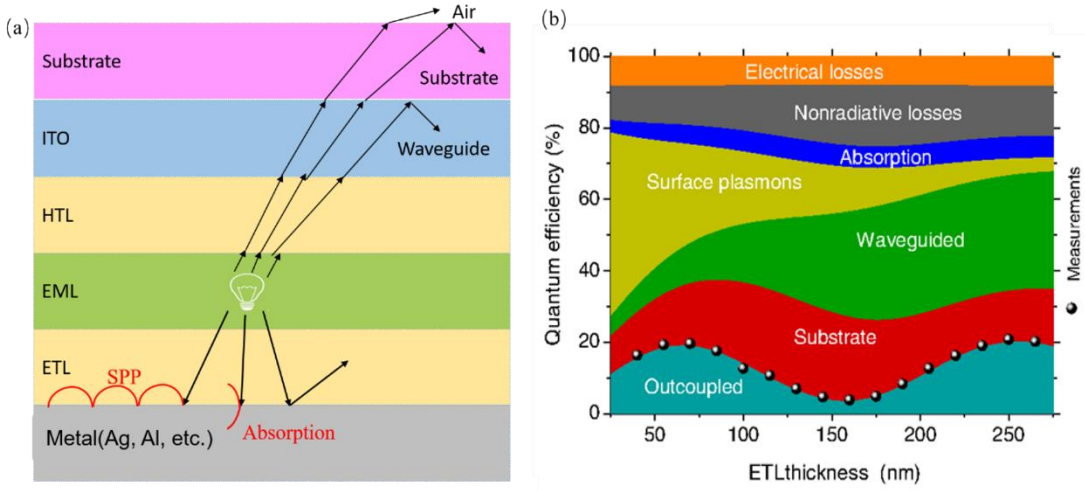

Figure 1.12 (a) schematic illustration of light propagation and loss channels in the perovskite LED devices. (b) The PeLED stack's optical mode distribution as a function of emitter distance from cathode is depicted. The optical properties of the PeLED are determined by the emitter's strong interference with itself (Reprinted with permission from ref. [55] © 2015 Society of Photo-Optical Instrumentation Engineers (SPIE)).

1.2.1 Optical simulation of a PeLED Cavity

A classical dipole model, which was first proposed by Chance, Prock and Silbey (CPS) [53-54], is widely employed to simulate the optical characteristics of LEDs. Excitons are viewed in this model as damped oscillators whose output is affected by reflected electromagnetic fields. The decay rates of damped oscillators are both radiative and non-radiative, and are mainly determined by the photoluminescence quantum yield (PLQY) and the emitter's radiative mechanism, such as fluorescence, phosphorescence, delayed fluorescence, etc. [55-56]. The distance between the dipole (emitter) and the

metallic cathode (z in Figure 1.13), the orientation of the dipole (Θ), and the cavity length (d in Figure 1.13) affect the radiative decay rate. The decay rate related to the optical structure (z, Θ, d) is expressed by the Purcell factor. Even though the Purcell factor can be used to boost the rate at which the emitter's radiation decays, this doesn't have a big effect on emitters with lots of PLQY [57]. In this work, all optical simulations are performed by the commercial software COMSOL Multiphysics based on the finite element method, and the assumptions of this electromagnetic model are [58]:

1) The dipole is positioned in a non-dissipative, isotropic medium (i.e., purely real permittivity).

2) The wavelength of the radiation, as well as the distance between the emitter and the different interfaces, are extremely long in comparison to the dipole's spatial extensions (point dipole approximation).

3) The interface planes could be extended indefinitely.

4) The multilayer stack is nonmagnetic.

5) There are losses resulting from the stack structure from the viewpoint of the radiating dipoles.

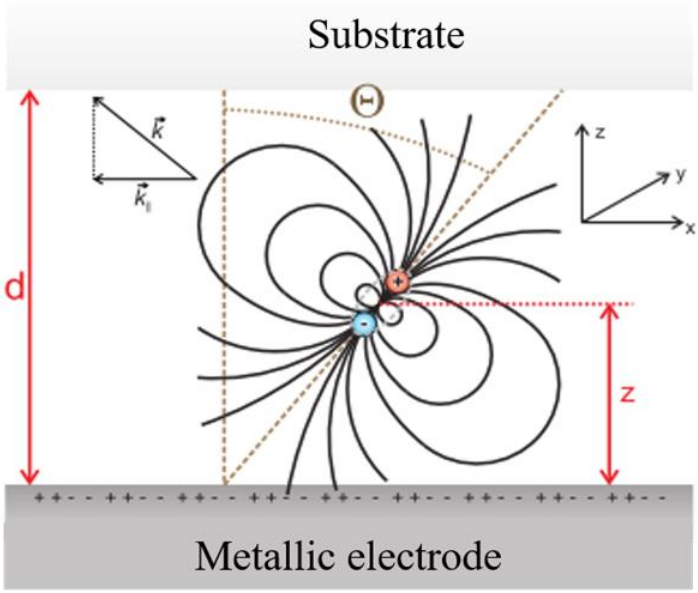

Figure 1.13 Radiative exciton recombination can be regarded as damped driven radiative

dipoles; the reflected electromagnetic field from the metallic cathode drives these damped dipoles. The decay rates of the dipoles include radiative and non-radiative processes, depending on the photoluminescence quantum yield of the emitter. The radiative decay rate can be impacted by the dipole moment orientation with regard to the substrate plane(θ), the emitter distance from the metallic electrode(h), and the cavity length(d) (reprinted with permission from ref. [59] ©1985 American Physical Society).

1.2.2 A dipole near the Metal-Insulator Interface

As stated before, the emission is regarded as a damped harmonic oscillation, and the motion equation for the electronic dipole moment p is as follows [55]:

$$\frac{d^2p}{dt^2} + b_0\frac{dp}{dt} + \omega_0^2 p = \frac{e^2}{m}\overrightarrow{E_r}(\omega) \tag{1.26}$$

Where, ω_0 is the resonant angular frequency without damping, b_0 is the damping coefficient as the dipole transition rate, m is the effective mass, e is the electric charge, and Er is the reflected electromagnetic field at the dipole position. The reflected field is effective on the dipole and oscillates at the same complex frequency $\Omega = \omega - ib/2$, that is

$$p = p_0 e^{-i\Omega \mathrm{t}} = p_0 e^{-\left(\frac{i\omega+b}{2}\right)\mathrm{t}} \tag{1.27}$$

$$E_r = E_0 e^{-i\Omega t} = E_0 e^{-\left(\frac{i\omega+b}{2}\right)t} \tag{1.28}$$

Here， ω and b are the frequency and damping rate, respectively, in the presence of the mirror. By substituting Equations (1.27) and (1.28) into equation (1.26), we obtain:

$$\Delta\omega \approx \frac{b^2}{8\omega} - \frac{bb_0}{4\omega} - \frac{e^2}{2p_0 m\omega} Re(E_0) \tag{1.29}$$

$$b = b_0 + \frac{e^2}{2p_0 m\omega} Im(E_0) \tag{1.30}$$

From Equations (1.29) and (1.30), we know that the normalized damping rate and frequency shift are proportional to the out-of-phase and in-phase components, respectively, of the reflected field. Since all dipole orientations are composed of

perpendicular and parallel dipole components, the aforementioned solution for b yields the dispersive radiated power of the dipole as a function of the reflected electric field at the location of the dipole. Figure 1.14 illustrates an example of the calculated power dissipation of the dipole in a LED device [59].

For both p-polarization and s-polarization, the reflected electric field at the dipole location in the multilayer optical structure can be estimated using the Fresnel reflection coefficient across the boundary. For p-polarization and s-polarization, the Fresnel reflection coefficient between the two dielectric materials is defined as:

$$r_{12}^{p} = \frac{\varepsilon_1 k_{\perp 2} - \varepsilon_2 k_{\perp 1}}{\varepsilon_1 k_{\perp 2} + \varepsilon_2 k_{\perp 1}} \tag{1.31}$$

$$r_{12}^{s} = \frac{k_{\perp 2} - k_{\perp 1}}{k_{\perp 2} + k_{\perp 1}} \tag{1.32}$$

Here, $k_{\perp 1}$ and $k_{\perp 2}$ are the normal component of the wavevector in medium 1 and 2. ε_1 and ε_2 are the permittivity of the two medium 1 and 2.

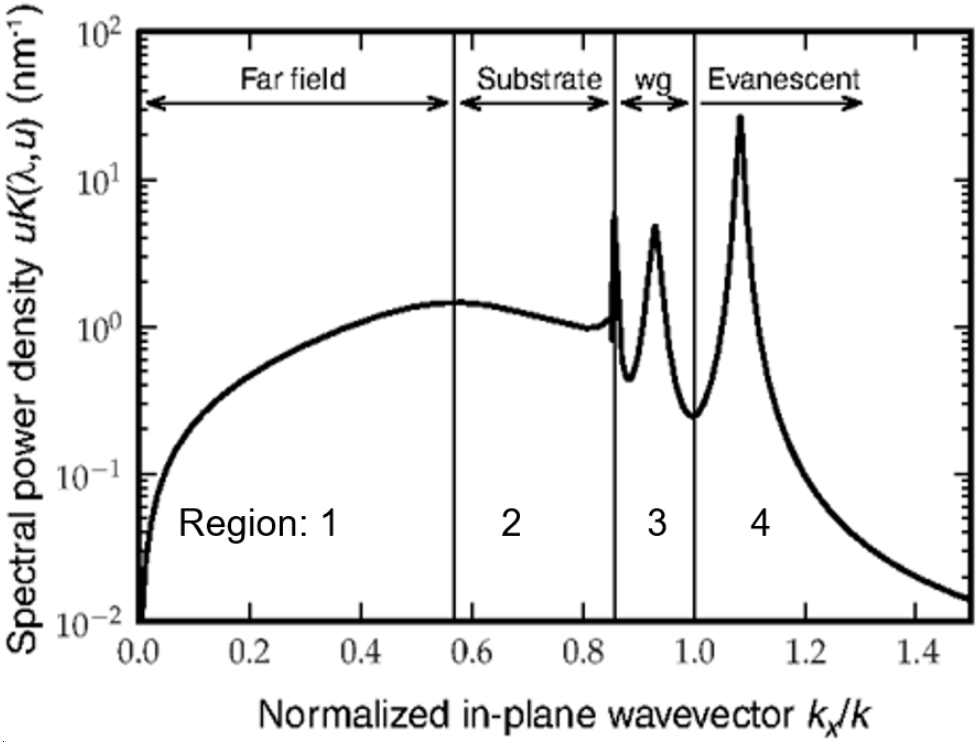

Figure 1.14 According to the magnitude of the radiated in-plane wave vector, the calculated dipole radiation (power loss) may be categorized into four different zones: Section 1, which

describes radiation emitted into the surrounding environment, the so-called "direct emission." Region 2 indicates the "substrate mode." The third and fourth zones denote the "waveguide mode" and "evanescent mode," respectively. The orientation of the emitter dipole and the distance from the metal have a significant effect on the radiation coupling to the surface plasmon and the contribution of the evanescent mode (reprinted with permission from ref. [59] © 2015 Society of Photo-Optical Instrumentation Engineers (SPIE)).

1.2.3 Mode Analysis

After calculating the optical power dissipation of the dipoles with respect to the in-plane wave vector, the optical mode distribution of the LED can be attained according to the kinematic limit, and the optical channels from left to right are: direct emission, substrate mode, waveguide mode and surface plasmon mode, as shown in Figure 1.14, in which the in-plane wavevector in the medium is calculated via $k_{\parallel} = k_0 * n * sin\theta = (2\pi/\lambda) * n * sin\theta$. The region is the direct emission, where the wave vector meets the equation:

$$0 < k_{in} < n_{air} k_0 \tag{1.33}$$

where $k_0 = 2\pi/\lambda$ is the wavevector in the free space, and n_{air} is the refractive index of air. This region represents the fraction of generated photons that escape into the ambient air from the glass substrate.

In this region 2, light is trapped in the substrate because of the total internal reflection at the substrate and air interface, where the wavevector satisfies:

$$n_{air} k_0 < k_{in} < n_{sub} k_0 \tag{1.34}$$

Here, n_{sub} is the refractive index of the substrate. Utilizing a semi-hemispherical lens with the same refractive index as the substrate, the radiation in this area may be efficiently extracted. When k_{in} becomes larger than the wavevector in the glass substrate, partially photons are confirmed in the ITO area because of the total internal reflection at the ITO-Glass interface and will not reach the substrate, therefore

integrating the region 3 of the Figure 1.16, i.e.:

$$n_{sub}k_0 < k_{in} < n_{EML}k_0 \tag{1.35}$$

This would result in the contribution of the "waveguide mode". Here n_{EML} represents the refractive index of the emissive layer (EML), where the dipole is situated. The maximum permissible magnitude of the in-plane wave vector associated with the far-field radiation is $n_{EML}k_0$, because the emitter is in the EML. When the in-plane wave vector exceeds the wave vector's total magnitude, like

$$k_{in} > n_{EML}k_0 \tag{1.36}$$

The wave vector will gain an imaginary component, leading to the radiation evanescent in the near field, which is a phenomenon of the SPP mode.

1.2.4 Emitter Dipole Orientation

The orientation of the emitting molecule's transition dipole moment vector (TDMV) with respect to the plane of the PeLED substrate has a significant impact on light extraction. [60-61] A horizontally oriented dipole with its axis perpendicular to the substrate plane maximizes light extraction since dipole radiation is strongest perpendicular to its axis. A vertically oriented dipole will strongly couple to the metallic cathode's TM-polarized SPP modes owing to the SPP electric field's full overlap with the dipole vector. And then the effect of emitter dipole orientation on mode contribution in an LED device can be studied. In general, two common approaches can be used to measure the direction of the transition dipole moment of emitter molecules in the film. The first method employs a variable angle spectroscopic ellipsometer to estimate the anisotropic extinction coefficient (k) (VASE) [63]. The second method is to measure the angle-dependent p-polarized photoluminescence of the emitting film layer and fit the measurement findings to the optical simulation, assuming that the emitter's TDMV orientation is different from that of the film layer itself.

1.3 Outline of this thesis

The present thesis is devoted to the simulation and calculation of the coupling of plasmonic structures in multilayer metal and dielectric cavities with semiconductor nanocrystal excitons. We mainly analysed perovskite light-emitting diodes and nanoscale optical sensors.

In chapter 1, I briefly introduced the principles and methods used, such as surface plasmonic polarizations, the spectroscopy ellipsometer, and effective medium theory. Then we introduce the principle of the perovskite light-emitting diode and its simulation mode.

In chapter 2, we study the multiple resonance modes in the metal/insulator/metal (MIM) systems with lateral and vertical gratings. Firstly, through comparing the amplitude component Ψ and the phase shift Δ of the p- and s- waves from our simulation model with the experimental ellipsometry measured ones and its fitting (left figures), the reflectance, transmittance, and absorbance of the vertical grating MIM system can be calculated, and the resonance modes constitute Epsilon-Near-Zero (ENZ) resonances. Similarly, this method is also suitable for the lateral grating MIM systems that maintain the ENZ mode. Furthermore, these two MIM systems are both beneficial for spontaneous emission enhancement and the Purcell effect. The only difference is the strongly coupled ENZ modes of the vertical MIM system can support a wide frequency band that can be exploited for cavity resonances, while the weak uncoupled ENZ mode of the lateral grating MIM system results in uncoupled modes.

In chapter 3, taking a flat perovskite light-emitting diode (PeLED) as an example, we systematically analyse the influence of geometric configuration and dipole orientation on the main characteristics of the LED, such as Purcell factor and external coupling

efficiency. Through theoretical calculations, the optimally configured flat-panel LED can be obtained.

In chapter 4, we explore the effects of interface modifications on the performance of perovskite-based LEDs. Using the multilayer metamaterial nanopatterns to modify the metal-transport interface, the Purcell factor and outcoupling efficiency of the PeLED can be enhanced, and in turn, the external quantum efficiency will be improved with regard to the nanopattern-free PeLED counterpart. Finally, the overall performance of the PeLED will be improved compared to the corresponding flat PeLEDs.

In chapter 5, we investigate an optical pressure/temperature nanosensor by designing and numerically simulating a metal/insulator/metal (MIM) nanopillar array covered by a metal film. The principle involves utilizing the sensitivity of the gap plasmonic resonance to the distance from the nanopillars to the silver film for detecting the pressure or ambient temperature through the variation of the device colour.

Chapter 2: Epsilon-Near-Zero Resonances Based on Metal-Insulator-Metal Gratings for Spontaneous Emission and Purcell Effect Enhancement

Subwavelength layered metal-insulator nanostructures with tuneable resonance provide a versatile and effective platform for various applications in optoelectronics and photonics, attributed to the reason that stacked metal-insulator (MI) metamaterials with hyperbolic isofrequency surfaces are capable of supporting high-k waves and large local density of the state (LDOS), resulting in strong Purcell enhancement of spontaneous emission. In this chapter, the optical properties and the resonance modes of metamaterial systems composed of metal-insulator-metal (MIM) metamaterials, such as planar MIM and MIMIM systems, and or MIM structures where one metal layer is patterned as a grating, are investigated utilizing spectroscopic ellipsometry and COMSOL Multiphysics. For systems with multiple dielectric layers (i.e., MIMIM) or lateral gratings in MIM structures, our calculations demonstrate that multiple cavity modes appear, in particular, resonances with an effective dielectric constant close to zero, the so-called Epsilon-near-zero (ENZ) modes. The high local density states of the ENZ modes in the MIM system result in a strong Purcell effect of the spontaneous radiation. Moreover, the ENZ mode frequency can be adjusted in the whole visible spectrum through the thickness variation of the dielectric layer. In the MIM structure, lateral patterning of a single metal layer results in multiple weakly coupled ENZ resonances, whereas vertical layering results in strongly coupled modes.

2.1 Introduction

Spontaneous emission enhancement of a fluorophore is essential for the advance of single-photon sources [64-65], optical sensor [66], quantum information processing

[67], and plasmonic lasers [68-69]. In these systems, Microcavities and photonic crystals have been extensively investigated for spontaneous emission rate enhancement via the cavity Purcell effect [70-71] in these systems because they utilize a special propagation regime, namely nanometrically restricted evanescent waves arising from the plasmonic characteristics of ultrathin metallic films. Recently, research has found that planar plasmonic multilayer structures with ENZ condition characteristics [72-73], in which metal and dielectric multilayer planar is capable of behaving as absorbers (and resonant cavities), is a feasible option. For example, Dr. Caligiuri and his colleagues have proved that one single MIM structure [74], similar to one quantum well, is capable to maintain the Ferrell-Berreman mode (FB mode, 327nm) and bulk plasmon mode (BPP mode, 563nm), which constitutes Epsilon-Near-Zero (ENZ) resonances (Figure 2.1). And the ENZ mode (BPP mode) can be generated and tailored in the visible range via tuning the insulator thickness. Furthermore, through the finite element modelling and semiclassical model, the properties of the MIM system are studied, extended further to the coupling of the MIMIM system [75-76] with two MIM cavities, similar to double quantum well system, is also analysed, which works as a reference case in this chapter.

Here we investigate one complex MIM system with lateral gratings, which results in multiple cavity modes, and these modes could form ENZ bands at the specific wavelength. Next, we looked at the spontaneous emission of the light emitter, like the perovskite CsPbBr3 nanocrystal film, which was triggered by the MIM systems with vertical layers and systems with lateral gratings, which resonate with the absorption and emission bands of the fluorophore's light.

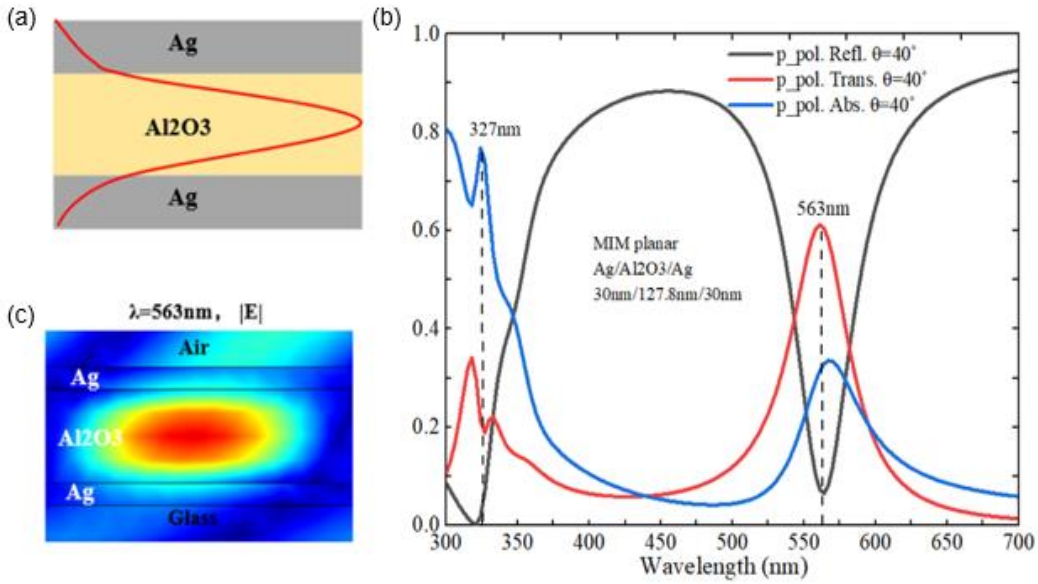

Figure 2.1 Sketch of single MIM system with metal layer much thinner than the skin depth(a). (b) Simulated reflectance (black curve), transmittance (red curve) and absorbance (blue curve). The corresponding MIM system consists of thicknesses of Ag and Al2O3 layers of 30nm and 128nm, respectively. The norm electric field distribution of the MIM is shown in (c). Light is impinging from the top with normal incidence at 40°.

2.2 Simulation Method of the MIM System

Figure 2.2a shows the schematic diagram of the simulated model. A p- /s-polarized plane wave with an incident angle of 40° impinges on the multilayer metal-insulator system from the air, via an internal port. The multilayer metal-insulator system is composed of alternating Ag and Al2O3 films. And then the light passes through the glass substrate through an output port. Floquet periodic boundary conditions (PBCs) are used at all boundaries of the geometry (along the X-axis and Y-axis), to ensure that the simulated system has an infinite length in these directions, while the perfectly matched layer (PML) has been set in the Z direction. For the p-polarized plane wave, we select the "out-of-plane" with $\boldsymbol{H} = (0,0,1)$ configuration, while the "in plane wave-vector" with the $\boldsymbol{E} = (0,0,1)$ is adopted in the s-polarized case. In the frequency

domain, the reflectance (R), transmittance (T), and absorbance (A) of the multilayer metal-insulator system are calculated, with a minimum mesh size of 2 nm. Then, according to the equation $\rho = \frac{r_p}{r_s} = \tan(\Psi)e^{i\Delta}$, where Ψ is the amplitude component and Δ is the phase shift of the p-polarized (TM) and s-polarized (TE) plane waves, we are comparing our results with the measured data (Ψ, Δ, R, T, A) from the spectroscopic ellipsometry, and further retrieve the optical constant of the whole multilayer MIM systems via the Cauchy relationship and mean square error (MSE).

In step 2, as displayed in Figure 2.2b, a typical electromagnetic model is carried out to simulate the spontaneous emission enhancement of the fluorophore in the stacked thin films. A dipole (the red dot in Figure 2.2b) is the light source, and other simulated setting conditions are the same as in the above simulated model.

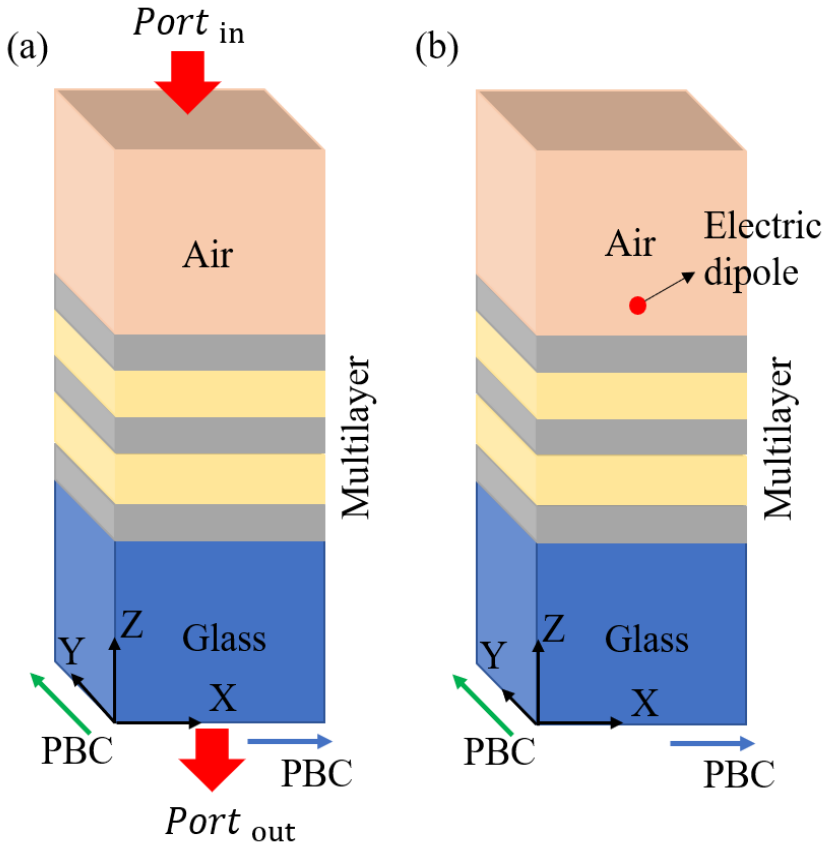

Figure 2.2 Schematical diagram of the simulated model.

2.3 Optical analysis of the multilayer MIM system

To confirm the accuracy of the simulated modelling, we firstly compared the numerical prediction with the measurement results of the corresponding real samples. Here the ellipsometry measured results are from the 20nm/80nm/20nm/80nm/20nm MIMIM system [77], where the metal and insulator are silver and Al2O3, respectively. Figure 2.2 depicts the amplitude component Ψ and the phase shift Δ of the p- and s- waves from the experimental ellipsometry measurements and its fitting (left figures), and the FEM simulations (right figures) for the MIMIM structure with different incident angle (40°, 60°, 80°). It should be noted that we regard the MIMIM structure as a single material to explore its homogenization optical properties here. Compared to the graphics on the left and right in Figure 2.2, the results are consistent in respect of the curve's overall trend but differ in terms of absolute values. This is because it is challenging to accurately control the layer thickness of a real sample in a way that is completely equivalent to the simulated structure. Apart from that, the use of a glass substrate in the actual sample will impact the experimental results, which is partially taken into account in the simulations. The variation in the phase shift Δ between the p- and s- waves indicates this system is an anisotropic considering the multilayer structure as one single material.

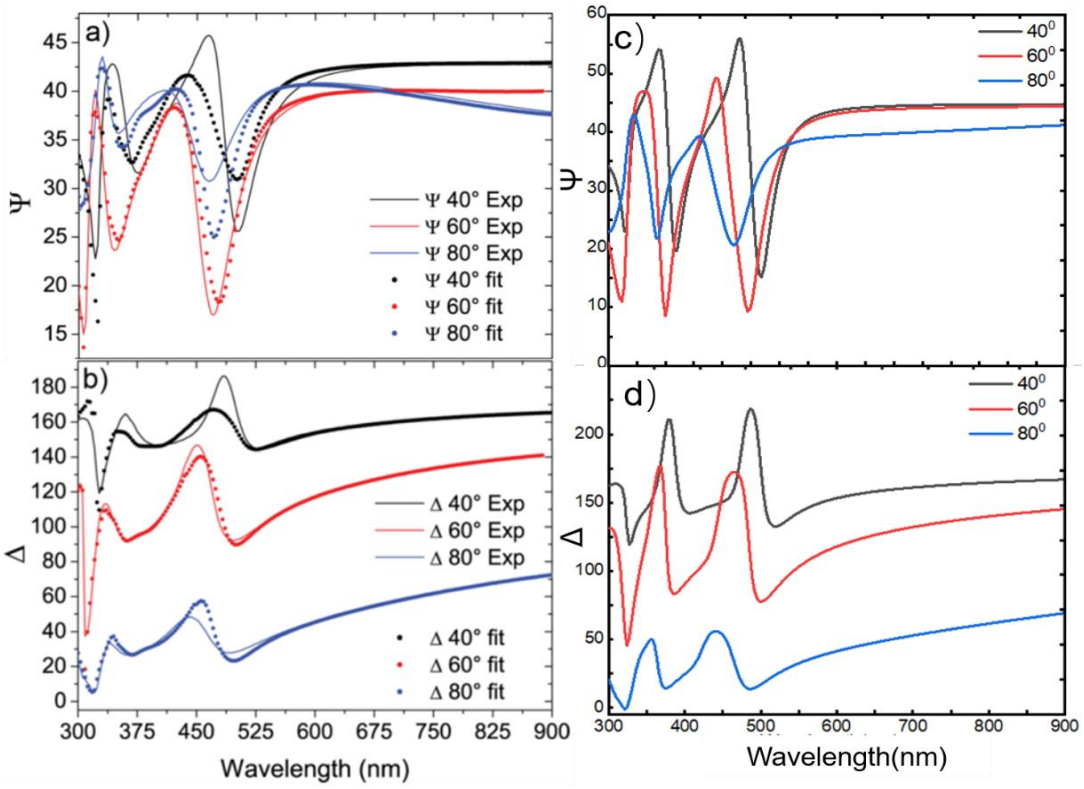

Figure 2.3 Comparison between Ψ and Δ form the experimental (left, solid lines and dotted lines from the ellipsometry measured and its fitting, respectively) and the numerical calculation based on COMSOL simulation(right) for the MIMIM structure (left figure reprinted with permission from ref. [77]. Copyright © 2018 American Chemical Society).

Figure 2.4 shows the reflectance, transmittance, and absorbance of the MIMIM structure are measured and calculated with an incidence angle of 40° for one p-polarized plan wave. It can be seen from this graphic, the results of the experimental ellipsometry are basically consistent with the results of the COMSOL simulation. Moreover, it's interesting to know that the absorbance peaks are near to the reflection dips, which correlates to the modes of bulk plasmon polaritons (BPPs) (e.g., experimental: 373nm and 510nm; simulation:396nm and 510nm), where the difference is caused by the layer thickness of the real samples. According to Dr. Caliguiri's work, these BPP modes exhibit the ENZ characteristics. Thus, using this method, we can predict and design multilayer structures with ENZ nature.

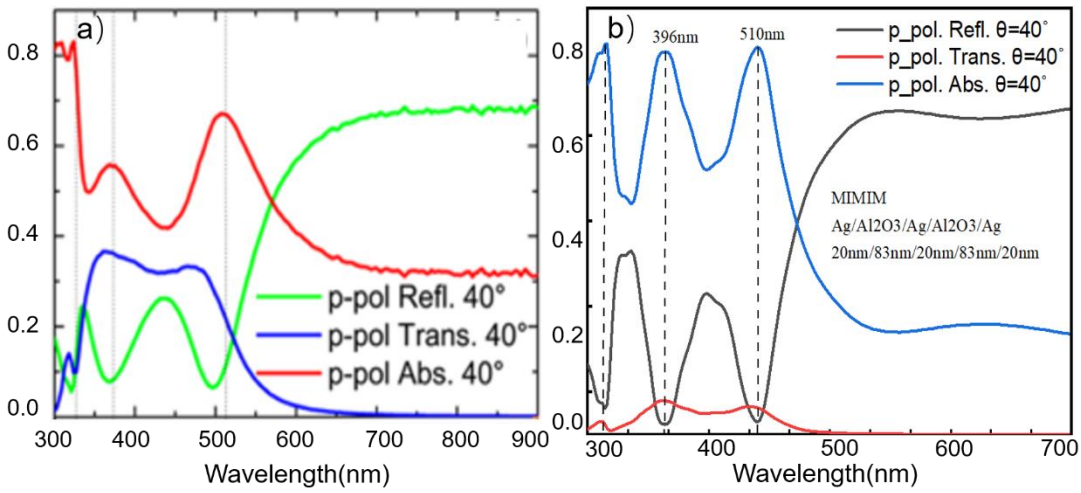

Figure 2.4 The p-polarization reflectance(R), transmittance(T), and Absorbance (A) of the MIMIM system from ellipsometry measured (left) and the numerical calculation based on COMSOL simulation (right) (left figure reprinted with permission from ref. [77]. Copyright © 2018 American Chemical Society).

2.4 Analysis of the MIM Grating

Figure 2.5a illustrates the schematic configuration of one MIM system consisting of 20nm Ag/110nm Al2O3/20nm Ag with the lateral grating. As in the actual MIM lateral grating sample, we defined the period as equal to 3um in our simulation model. For the lateral grating, the bottom metal (Ag) layer as a pillar array is created via optical lithography and successive etching. The insulator film is then deposited in two steps, first filling the gaps between the Ag pillars and then uniformly covering the whole substrate. From the calculated reflectance, transmittance and absorbance for a p-polarized plan wave with an incidence angle of 40°, as it shown in Figure 2.5b, we know that the two absorbance peaks are near to the reflectance dips correspond to the two distinct BPP modes (λ=516nm, λ=645nm) which form in separate lateral regions of the MIM system, and these resonance frequencies are relied on the local thickness of the dielectric (Al2O3) layer (as Figure 2.5 a red and green line area). And these two BPP modes should exhibit classical ENZ properties, similar to the MIMIM system,

where the norm electric field, X and Y component electric field distribution of them shown as Figure 2.5c and 2.5d. It can be seen from these figures, these two weak cavity modes (BBP modes) are formed because of the lateral patterning of one metal layer in the MIM structure, while in the vertically layered MIM system (as Figure 2.6a), strongly coupling cavity modes is capable to form the ENZ bands, in analogy to the Kronig-Penney model in quantum mechanics [11]. For a layered MIMIM system with 20nm/85nm/20nm/85nm/20nm layer thicknesses, the reflectance, transmittance, and absorbance are presented in Figure 2.6b, and the electric field distribution at the resonant wavelength (λ=402nm, Figure 2.6c and λ=516nm, Figure 2.6d) indicates the formation BPP modes. The difference is that the lateral grating method produces uncoupled resonances, whereas the vertical approach creates a strongly coupled ENZ mode, which results in an extensive frequency band that can be used for cavity resonance, thereby overcoming the compatibility issue associated with the two-stage system required for single mode laser applications.

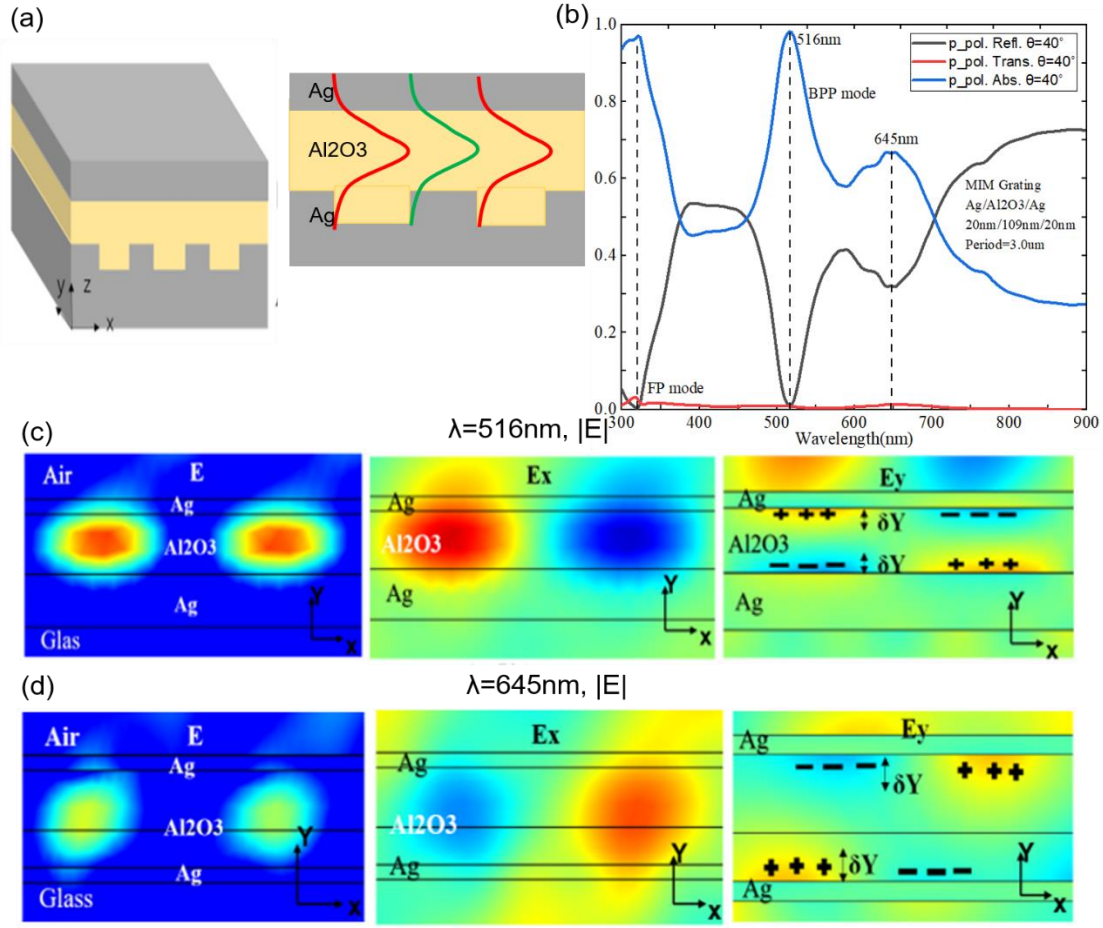

Figure 2.5 (a) 3D schematic configuration MIM grating system with the bottom Ag layer as a pillar array and the multiple cavity modes in the lateral grating MIM structure. (b) Simulated reflectance (green curve), transmittance (blue curve) and absorbance (red curve), corresponding buried grating MIM system consists of 20nm Ag/109nm Al2O3/20nm Ag and the diameter and height of the grating is respectively 1.5um and 50nm, calculated at 40° Simulated norm, X and y component electric field distribution in the MIM at the resonant wavelength 438nm (c) and 591nm (d).

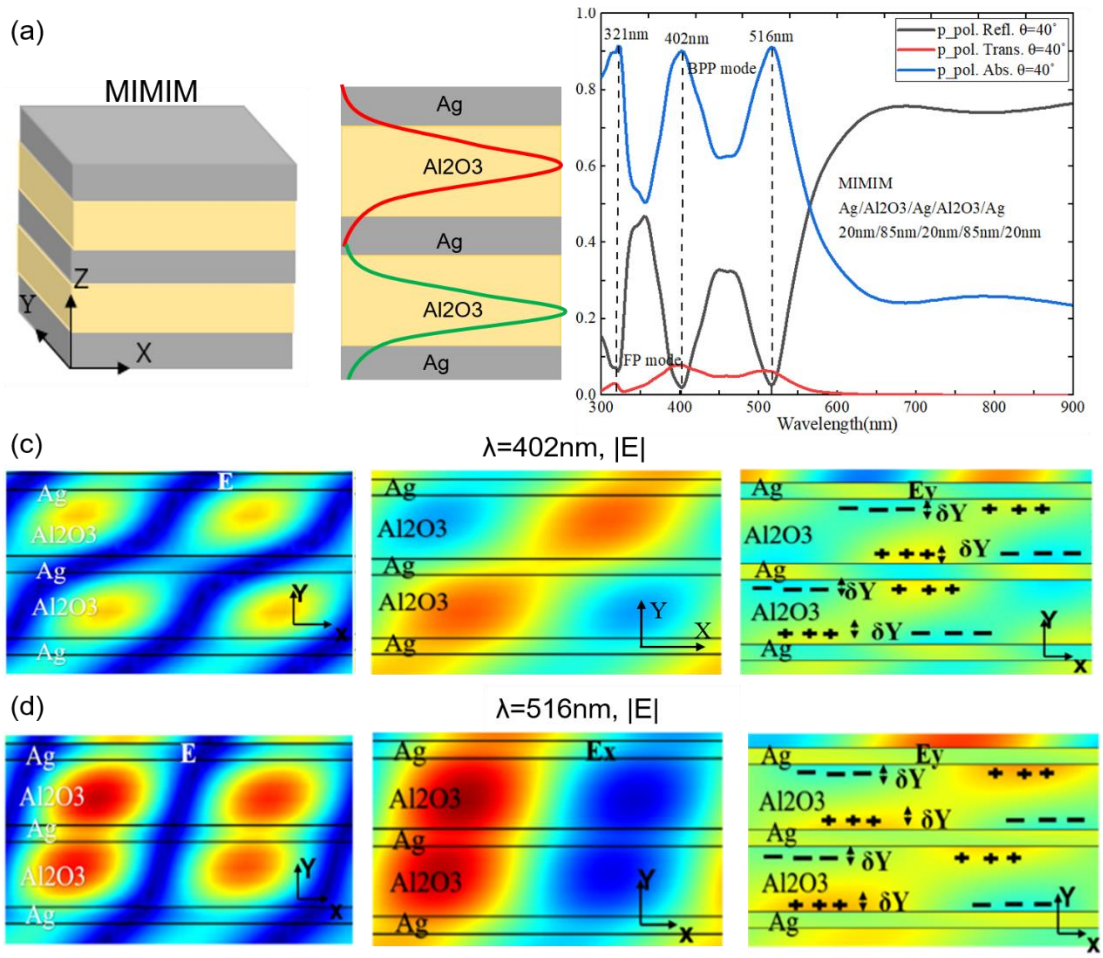

Figure 2.6 (a) 3D schematic configuration MIMIM system. (b) Simulated reflectance (black curve), transmittance (red curve) and absorbance (blue curve) of 20/85/20/85/20 MIMIM structure, calculated at 40°. Simulated norm, X and y component electric field distribution in the MIMIM at the resonant wavelength 402nm (c) and 516nm (d).

Furthermore, these two resonance wavelengths (λ=516nm, λ=645nm) of the MIM grating system correspond to two planar MIM structures with the local Al2O3 thicknesses of 109nm and 149nm. Figure 2.7 shows the absorption spectra of the grating MIM and the corresponding two planar MIMs at an incident angle of 40°. As previously shown [77], the surface plasmon enhanced absorption (SPEA) and the surface plasmon coupled emission (SPCE) of the light emitter, such as perovskite nanocrystal films, placed on top of the nanocavity system, have already been proven to drastically enhance

the spontaneous emission of the emitter. Therefore, we want to explore whether this can also be used with the lateral grating MIM system. Under the same condition (the location of the light emitter and the geometric parameters of the MIM system are the same), the Purcell factor of the lateral MIM grating system for an isotropic dipole (working as a light emitter) is 25 (accurate 25.22), which is higher than that of 25 (accurate 24.98) of the vertical MIM (that is the MIMIM system), reflecting the performance of these two MIM systems in improving the light-emitter interaction. Therefore, both the vertical stack and the lateral structures have the same Purcell enhancement effect.

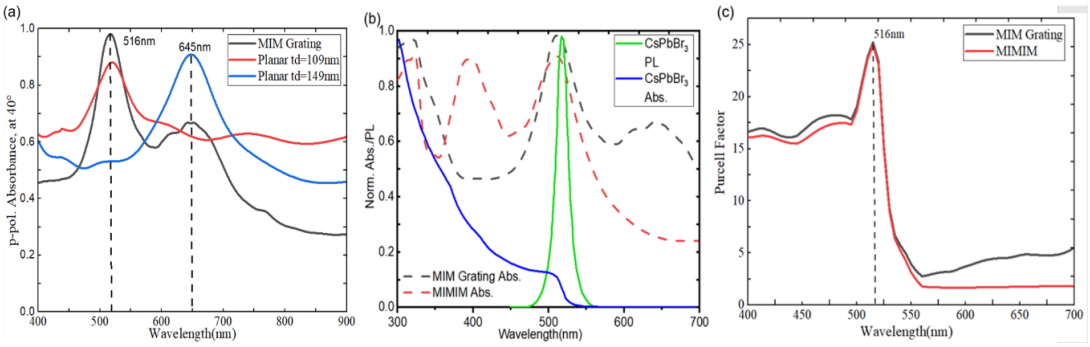

Figure 2.7 (a) Calculated absorbance of the lateral rating MIM and the corresponding planar MIMs. (b) The normalized absorption (blue line) and emission (green line) spectra of the CsPbBr3 nanotube are plotted together with the normalized absorbance of the MIM grating (black dashed line) and MIMIM (black dashed line) structure. (c) The Purcell factor for an isotropic dipole located a distance of 10nm above the MIM grating (black line) and MIMIM structure (red line) (reprinted with permission from ref. [77]. Copyright © 2018 American Chemical Society).

Next, we studied the two absorption peaks of the MIM grating system with regard to the width of the MIM and the Al2O3 thickness. As can be seen from Figure 2.8, these two ENZ cavity modes are sensitive to the Al2O3 thickness in the cavity, while the width of the MIM grating has no obvious influence on the two resonance modes. By tuning the thickness of Al2O3 in the cavity, as illustrated in Figure 2.8b, the low-energy

BPP mode exhibits a noticeable redshift, which can be adjusted throughout the visible spectrum. However, the two-resonance wavelengths change linearly, lacking mode coupling features. Thus, according to the required criteria, we could flexibly select the lateral and vertical grating MIM systems for coupling to the emitter placed there.

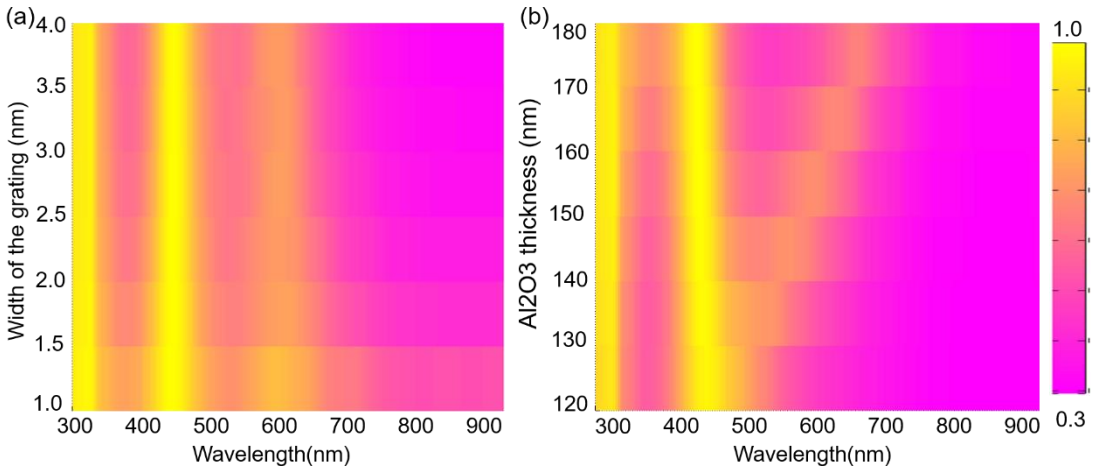

Figure 2.8 The contour plot of the calculated absorbance spectrum with respect to the width of the MIM grating (a) and the Al2O3 thickness (b).

2.5 Chapter Summary

In summary, we designed and compared two complementary MIM grating structures able of sustaining the EZN double resonance. Differently from the vertical grating MIM system that results in coupled resonances, the lateral grating MIM system is equivalent to two uncoupled planar MIM systems. Both systems lead to a similar spontaneous emission enhancement of a dye layer placed on top of them.

Chapter 3: Photonic Cavity Effects for Enhanced Efficiency in Layered Perovskite-based Light-emitting Diodes

The layered light-emitting diodes (LEDs) are the classical method for solution-processable materials as emitters, such as metal-halide perovskites [78-81]. In the last several decades, the metal-halide perovskite LEDs (PeLEDs) have experienced rapid development, because of their excellent optoelectrical properties. However, most research focuses on the optimization of the charge injection and balance to improve the performance of LEDs. In this chapter, we designed and optimized the composition and thicknesses of the layers in the LED structure through systematic theoretical analysis of the optical power dissipation based on the finite element calculations. Under the assumption of the efficient photon generation in the emitting layer with an internal quantum yield of 0.9, we analyse the effect of the geometrical configuration and the dipole orientation on the main characteristics of the LED, such as the Purcell factor and the outcoupling efficiency. Our simulated result shows that the direction of the emitting dipole has a strong influence, where the in-plane dipole leads to a significant increase in external efficiency. Furthermore, the mismatch of refractive index and the different layer thicknesses can be tuned to maximize the Purcell effect and minimize internal losses. The combination optimization of the dipole orientation and layer thicknesses can increase the efficiency of the LED by up to a factor of 10. Therefore, our work emphasizes the importance of considering the photonic properties of LED structures if the goal is to maximize the efficiency of the LED.

3.1 Introduction of LED Development

Inorganic metal halide perovskite light-emitting diodes (PeLEDs) have attracted an

increasing interest in the applications of the next-generation flexible display devices and solid-state lighting owing to the excellent optoelectrical properties of the perovskite, such as high photoluminescence quantum-yield, facile bandgap tunability, large carrier mobility and lifetime, high colour purity, high brightness, and simple solution processability [82-89]. In recent years, PeLEDs have shown remarkable progress, with external quantum efficiencies (EQEs) boosted from 0.1% [86] up to more than 20% [87], catching up with their counterpart LED technologies such as organic and quantum-dot (QD) LEDs. In 2014, the PeLED have been first reported the EQE of 0.76%, 0.1%, and 0.018% for near-infrared, red and green emission at room temperature by Ten et al [90]. Thereafter, through material design, morphology control, composition engineering, and device optimization, tremendous efforts have been dedicated to increasing the efficiency of the PeLED, and the PeLED with an external quantum efficiency of 28.4% has been reported in the scientific literature. However, there are still large margins for further improvement since most of the light emission from the perovskite films remains trapped in the LED structure and is dissipated as heat. The main reasons are the mismatch of the refractive index between the emitter layer and both the ETL (electron transport layer) and HTL (hole transport layer) that causes multiple reflections within the LED, hence limiting the light outcoupling efficiency [85-86], as well as generating plasmonic coupling losses at the metallic cathode. Other important aspects are the dependence of the external quantum efficiency on the dipole orientation of the emitters and the possible light enhancement by the Purcell effect that could be achieved by taking the different film thicknesses into account.

Currently, most research is focusing on analysing and improving the optoelectronic properties of perovskite materials and charge transport layers in order to enhance the light extraction of perovskite LEDs [88]. A few studies have addressed the structure optimization of perovskite LEDs through analysis of the optical power loss in the

PeLED device [91]. In this respect, Shi et al. have quantitatively analysed the effects of the thickness and refractive index of perovskite films on the light outcoupling efficiency of the PeLED [88]. Generally speaking, the external quantum efficiency, namely the ratio between the number of photons emitted from the LED and the number of injected charge carriers, is determined by the internal quantum efficiency (η_{IQE}) and the light extraction efficiency (η, also known as outcoupling efficiency), according to the following expression:

$$\eta_{EQE} = \eta \cdot \eta_{IQE} = \eta \cdot \gamma \cdot \eta_{S/T} \cdot q_{eff} \tag{3.1}$$

Here the outcoupling efficiency η is defined as the ratio between the number of photons emitted to free space from the LED to the number of photons generated in the emitter (perovskite) layer, while the internal quantum yield η_{IQE} is defined as the ratio between the number of photons generated in the emitter layer (not necessarily all reaching free space) to the number of injected charge carriers. Furthermore, η_{IQE} can be decomposed into three factors, with γ describing the balance of the injected charges, $\eta_{S/T}$ is the singlet/triple capture ratio at room temperature (for perovskite films it can be taken equal to one [89, 91]) and q_{eff} is the effective radiative quantum yield of the LED. In particular, γ can be tuned by selecting a suitable transport layer and by adjusting its thickness [92]. q_{eff} depends on defects and trapping of excitons [93], and can be related to the intrinsic quantum yield (q) of the perovskite film [92, 94]:

$$q_{eff} = \frac{q \cdot F}{q \cdot F + 1 - q} \tag{3.2}$$

Where F is the Purcell factor, which describes how the cavity (the perovskite layer) impacts and enhances the electron-hole recombination rate (i.e., the spontaneous emission) [88]. The F can be calculated as:

$$F = \frac{r_{pe}}{r_0} \tag{3.3}$$

While r_{pe} and r_0 are the total radiative decay rates of a dipole emitter inside the PeLED

structure and in free space, respectively [58]. Equation (3.1) to (3.3) show that η_{EQE} is mainly determined by the outcoupling efficiency η and on the Purcell factor *F*, therefore emphasizing the need for a systematic and quantitative analysis, especially of these two factors that limit the generation and emission of photons from a PeLED device.

Nowadays, the typical architecture of such LEDs consists of a planar transparent electrode, coated with charge transport layers, the emitter layer, and the complementary charge transport layers, and is capped with an opaque counter electrode. Figure 3.1 describes such a commonly used structure consisting, from bottom to top, of a glass substrate, indium tin oxide (ITO) as transparent anode, Zinc Oxide (ZnO), $CsPbBr_3$ film, 2,2′,2″-(1,3,5-Benzinetriyl)-tris(1-phenyl-1-H-benzimidazole) (Spiro-OMeTAD) and silver (Ag) as cathode [78, 81, 82]. In this work, we use the metal halide perovskite light-emitting diodes (PeLEDs) as a demonstration example to methodically explore the optical loss mechanism in the layered PeLED device, thereby achieving the enhancement of the η_{EQE} of the PeLED. Our finite element calculation focused on the analysis of the effects of the orientation of the emitting dipole (here representing the generated photon in the active layer) and the Purcell factor F on the performance of the PeLED, which in turn depends on the thickness of the perovskite film.

3.2 PeLED Simulation Model

The structure of the PeLED in this work is shown in Figure 3.1a. The perovskite CsPbBr3 film (here defined by q= 0.9, γ=1, $\eta_{S/T}$=1) [94-96] is sandwiched between ZnO (working as ETL) and Spiro-OMeTAD (working as HTL). All these layers together form the photonic cavity associated with the LED. The real part of the refractive indexes (n_{real}) of the materials composing the PeLED that we adopted in the present study is shown in Figure 3.1b[77, 96-99]. Notably, there is a substantial

difference in the refractive index values of ITO/perovskite versus the other materials. This mismatch is detrimental to the LED performance as it leads to photon-trapping within the LED structure due to total internal reflection (TIR). Figure 3.1c shows the corresponding imaginary part of the refractive index (n_{imag}) that is strictly related to the power dissipated due to ohmic losses in the various layers. Furthermore, the typically small Stokes's shift between the absorbance band edge and emission peaks favours reabsorption of the emitted photons in the perovskite layer, as was also reported for LEDs based on quantum dots [91]. Similarly, the Ag cathode is implemented by following a Drude-Lorentz description [100-102].

All these calculations are performed by the commercial COMSOL Multiphysics software, which is based on the finite element method. As described in Figure 2D of the PeLED model, a hertzian dipole placed in the middle of the emitter layer is used as the excitation source (the red point). All the domain boundaries are surrounded by Perfectly Matched Layers (PML) to absorb the outgoing waves, and outside the PML domains are the scattering boundary conditions. To ensure the accuracy and reliability of the simulated results, the length of the simulation domain in the 2D PeLED model (as Figure 3.1d shows) is set to 8 um, which is much longer than the emission wavelength, and the minimum mesh size for the simulation is 1 nm. Furthermore, in the PeLED device, the generated photons can couple to the various possible channels: outcoupled to the air through the transparent electrode, lost in the substrate, waveguided mode, and the metal electrode-induced surface plasmon polariton (SPP) mode. To calculate the optical power loss in these channels, four power monitors are adopted in the model. The total radiated power radiating to the emitting material is measured by the circle monitor 1, which surrounds the centre dipole source. The light trapped inside the PeLED as waveguide mode is the energy difference between the monitors 2 and 3, while the power outcoupled to the air is collected by monitor 4. Similarly, the optical

power loss in the thick glass substrate is calculated through subtracting the power measured by monitor 4 from that of monitor 3. The SPP loss equals the total radiated power minus the power of monitor 2. Thus, the outcoupling efficiency η_{IQE} of the PeLED could be attained by the optical power measured by monitor 2 over the total radiated power from monitor 1. According to Equation (3.3), the Purcell factor of this PeLED can also be calculated by the ratio of the collected power by monitor 1 with or without the layered PeLED structure.

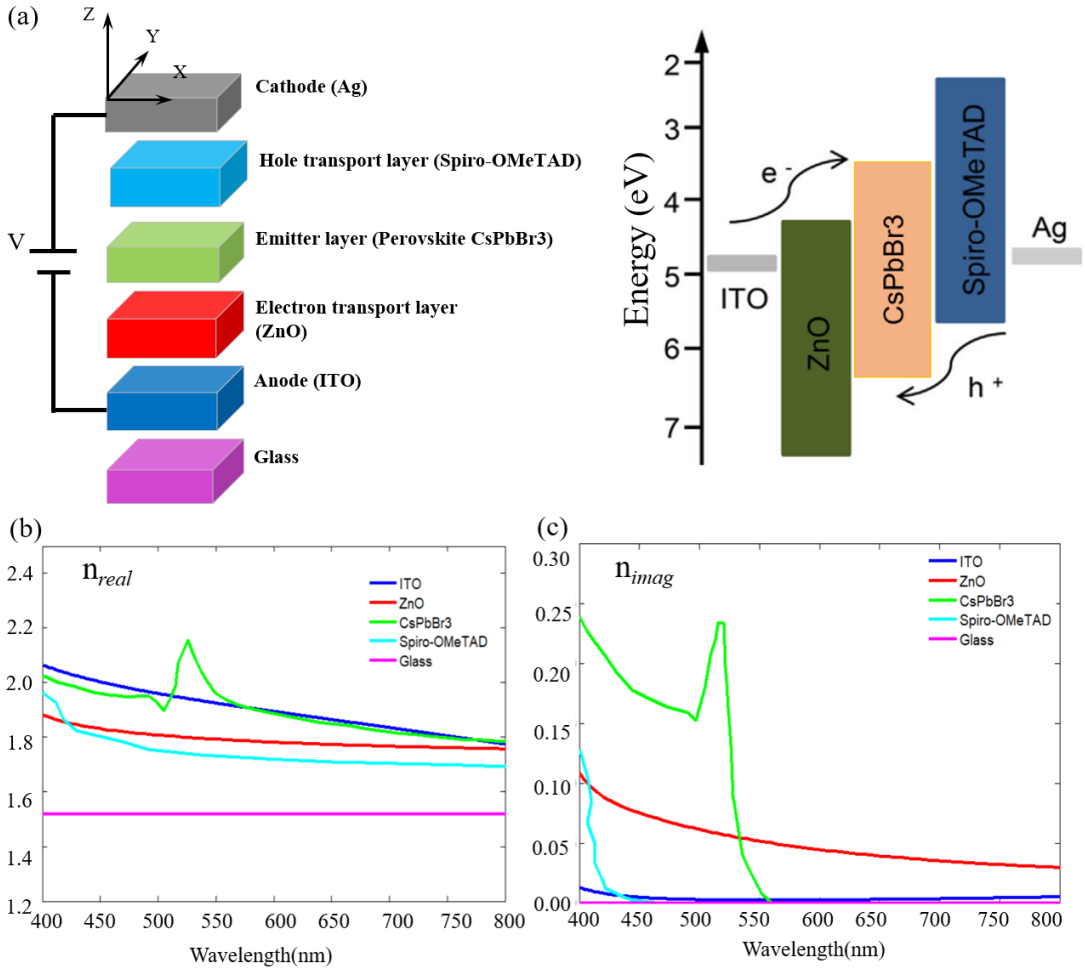

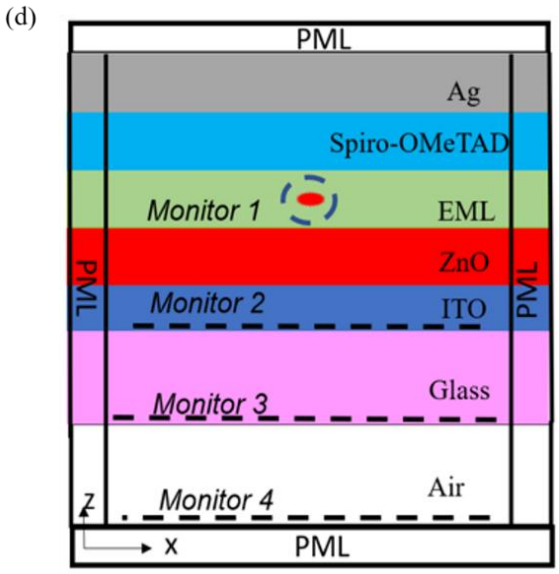

Figure 3.1 (a) Schematic diagram of the PeLED device structure and the energy level of its components used for optical simulations. Real (b) and imaginary (c) of the refractive indexes of various materials in the PeLED. (d) Schematic illustration of the simulation model with boundary conditions and the Hertzian emitter (red dot) representing the photons emission.

3.3 Effects of Dipole orientation & layer thicknesses

As can be seen from Figure 3.1b and c, the refractive index of the $CsPbBr_3$ film is the complex value at its emission wavelength of 540nm, and the Stokes-shift for the CsPbBr3 film (the distance between the absorbance and PL peaks) is small. Thus, the absorption of excitons-generated photons (defined as the reabsorption process) in the emitter layer is a concrete possibility [91], and should be considered in our model. In this way, our description matches with the intrinsic quantum yield q of actual perovskite films, which can be lower than 1, for example, equal to 0.9 [93, 95]. From a simulative point of view, in order to realize a perovskite layer with q=0.9, a sandwich-like structure is adopted to depict the emitter layer [97], which is formed by a loss-free (reabsorption-free, i.e., fully radiative zone) electron-hole recombination zone inside the perovskite film and located at its centre, as shown in the inset of Figure 3.2a. Vice versa, the photon

absorption (reabsorption) can instead occur in the surrounding volume. In order to properly quantify the specific dimensions of the sandwich-like emitter, a quantity ρ (ρ = d/D) is carried out to describe the ratio between the thickness of the radiative zone d and the full emitter thickness. In particular, in Figure 3.2a is plotted the intrinsic quantum yield q at 540 nm occurring in the reabsorption volume (i.e., photons reabsorbed by the emitting layer) vs. the thickness of the full perovskite layer (emitter layer, vertical axis) and the ratio ρ (horizontal axis). As mentioning that the PLQY of the perovskite CsPbBr3 film is 0.8, from Figure 3.2a, it is found that the first suggestion for a suitable perovskite thickness is D=30 nm with ρ equal to 0.6 for an isotropic dipole, values that have been employed in Figure 3.2b and 3.2c.

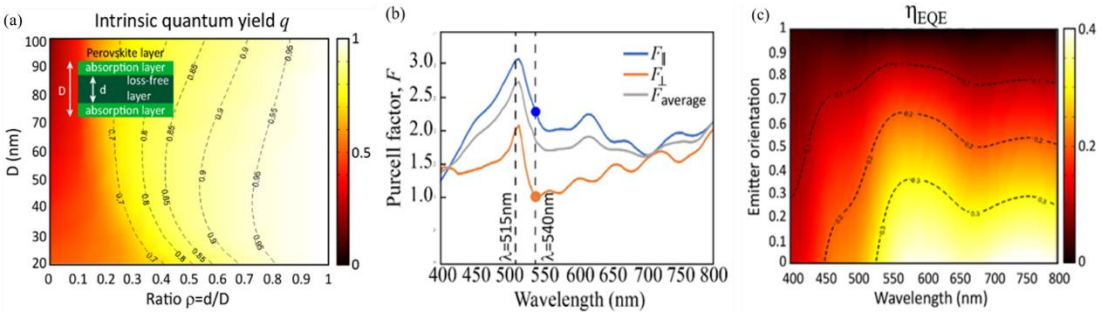

Figure 3.2 (a) Intrinsic quantum yield at the absorption layer vs. the variation of the CsPbBr3 film thickness and the ratio ρ. The chosen wavelength is 540nm. The inset represents the schematic of the emitting layer. (b) Purcell factor for horizontal, vertical and isotropic (average) dipole emitters as a function of wavelength. (c) Profile of η_{EQE} as a function of the emitting dipole orientation and wavelength. Emitter orientation equal to 0 means fully horizontal dipole. The y-axis describes the vertical dipole fraction (anisotropy factor equal to 0 means fully horizontal dipole).

In this work, we adopt a classical oscillating electrical dipole model to represent the light generated in the emitter layer. For an isotropic dipole orientation, the total radiated power and average Purcell factor both follow a linear relationship [89-90]:

$$P_{total} = \frac{P_{\perp} + 2 * P_{\parallel}}{3} \tag{3.4}$$

$$PF_{av} = \frac{PF_{\perp} + 2 * PF_{\parallel}}{3} \tag{3.5}$$

Where ⊥ and || represent the orientation of the dipole, that is, either perpendicular (⊥, vertical) or parallel (||, horizontal) to the flat interface of the PeLED structure. In this regard, Figure 3.2b shows the Purcell factor at different wavelengths for horizontal, vertical, and isotropic (average) dipole emitters located in the perovskite layer of the PeLED structure. The PeLED is defined by layers infinitely extended in X and Y directions with thicknesses (Z direction) equal to 100nm, 50nm, 30nm, 40nm, 200nm for Ag, Spiro-OMeTAD, CsPbBr3 (with ρ= 0.6), ZnO and ITO, respectively. Moreover, the glass substrate is considered semi-infinite along the Z direction.

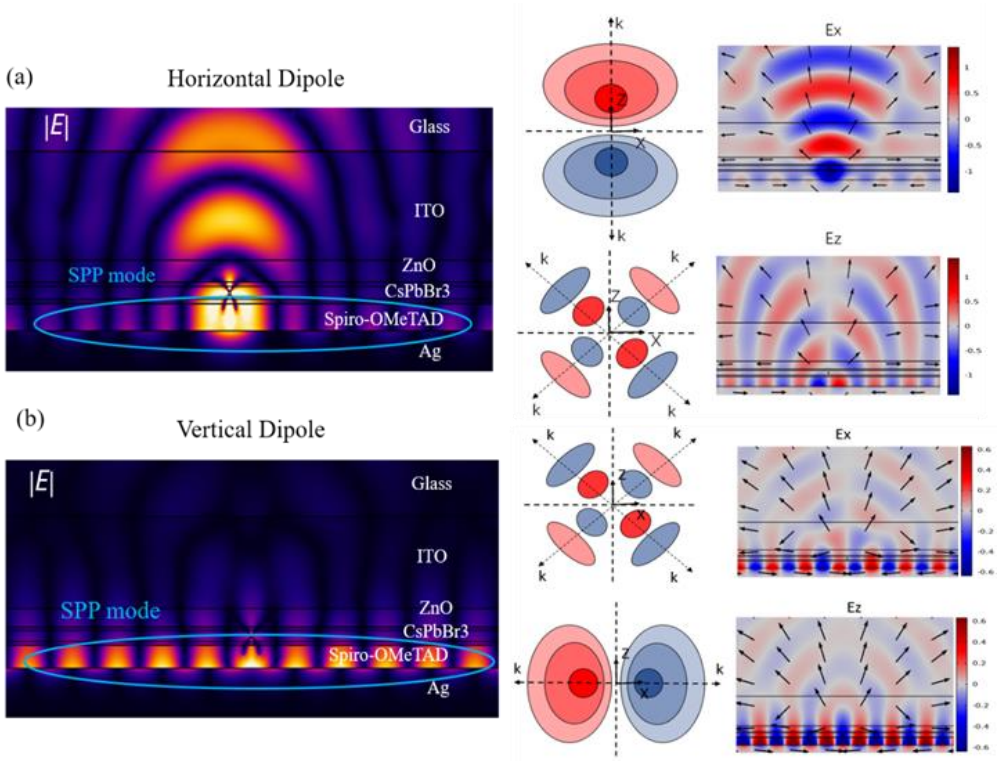

Figure 3.3 The electric field plots describe the modulus of the norm electric field (|E|=sqrt (Ex^2+Ey^2)) and electric field components (Ex、 Ez) in the PeLED in relation to the orientation of the emitting dipole (horizontal dipole (a) and vertical dipole (b)) and calculated at wavelength 540nm (blue frame corresponding to the blue dot in (4.2b). Similarly for the orange frame). The arrows represent the Poynting vector. The schemes show the PeLED (multilayer structure) surrounded (on the top) by air.

For an isotropic dipole emitter, the Purcell factor of the perovskite LED device is 1.86 at an emission wavelength of 540nm, while the maximum Purcell factor is 2.55 at the wavelength of 515nm. In addition, it can be seen from Figure 4.2b, the Purcell factor of the horizontal dipole at 540nm is much higher than that of the vertical dipole, which can be explained by the electromagnetic emission pattern of an electric dipole (see the electric field plots in Figure 3.3). With a horizontal dipole, the relevant electric charge oscillates along the X-axis and the radiation energy mainly propagates along the Z-direction (Figure 3.3a). The Ex-component dominates the radiant energy, and displays a strong transfer of the electromagnetic radiation into the air (outside the PeLED). However, for a vertical dipole, the electric charge oscillates along the Z-axis and the radiation energy mainly propagates along the X-direction. The Ez-component dominates the radiation energy. The electrical field is trapped at the interface of the Spiro-OMeTAD and Ag, and the radiated power is dissipated because of the SPP loss. And the electric field intensity decreases along the Z-axis, with a small transfer of the electromagnetic radiation to air (Figure 3.3b). Obviously, the contribution of horizontal dipoles to the spontaneous emission is well emphasized by these figures. According to Equation (3.4), it is recommended that the high concentration of horizontal dipoles determines the larger η_{EQE}, since the cavity Purcell factor impacts the effective radiative quantum yield of the PeLED device. And this view was verified with the contour figure in Figure 3.2c in this thesis. Especially, η_{EQE} in this contour figure was calculated with respect to the variations in the dipole orientation and emitting wavelength for a flat PeLED structure (here, γ =1, $\eta_{S/T}$=1, q=0.9, ρ=0.6). The dipole direction is defined in the range of 0 to 1, where 0 and 1 represent the dipole direction parallel and orthogonal to the PeLED surface, respectively. For the isotropic case, corresponding to a dipole orientation of 0.33 (see Equation 3.4), the maximum value for η_{EQE} at 540 nm is equal to 31.1%. Therefore, it is confirmed that the η_{EQE} of the illustrated PeLED is mainly determined by the horizontal dipole orientation, where the

η_{EQE} reaches the values of 0.4 for wavelengths 580 nm and 750 nm with completely fully horizontal dipoles.

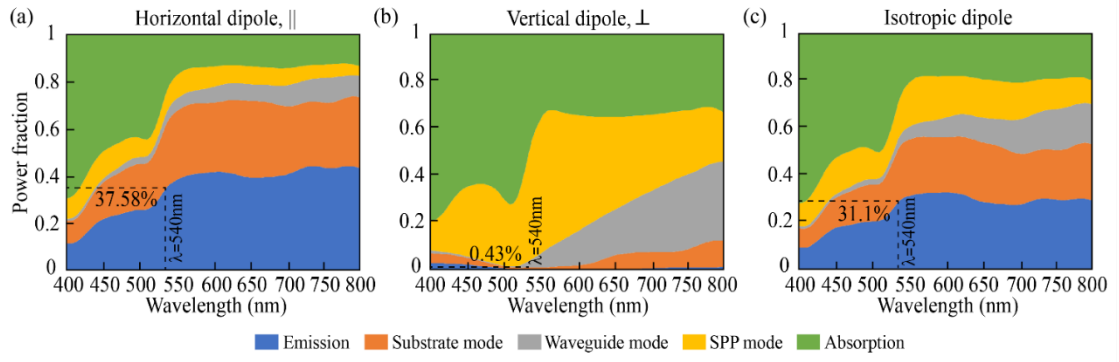

Figure 3.4 Reallocation of the perovskite emitted power in one of the five channels here considered: emission, substrate mode, waveguide mode, SPP mode, and absorption when horizontal (a), vertical (b) and isotropic dipole (c) are considered. The layers thicknesses are: 100nm, 50nm, 30nm, 40nm, 200nm for Ag, Spiro-OMeTAD, CsPbBr3 (with ρ= 0.6), ZnO and ITO, respectively.

Upon emission of radiation by the perovskite layer, the generated photons are able to be coupled into the various possible channels: outcoupled through the transparent electrode (part of the radiation channels into air (emission)); or lost in substrate mode -mode sustained by the glass-; lost as waveguided mode -mode sustained by the different layers but glass-; or lost as surface plasmonic polariton (SPP mode at the interface Spiro-OMeTAD/Ag, as $n_{real,perovskite} > n_{real,Spiro\text{-}OMeTAD}$; and be absorbed by the PeLED (non-radiative loss). The phenomena occurring in the PeLED device are generally descripted and summarized in Figure 3.4, considering the emitting dipoles parallel, orthogonal, and isotropic to the surface of the perovskite layer. It can be seen from Figure 3.4a, almost 38% of the optical power with a horizontal dipole at 540nm escapes from the PeLED device (direct emission), while a high fraction of the optical power is captured in the substrate mode. In contrast, with a vertical dipole, only a small portion of the generated photons couple into the air (as Figure 3.4b shows). This is because most of the optical power generated from a vertical dipole couple the two surface

plasmon polaritons or waveguide modes, as seen in Figure 3.3b. Following Equation 3,4, the total normalized radiation power emitted by an isotropic dipole can be calculated, returning a 31.1% of the direction emission (Figure 3.3c). Therefore, the outcoupling efficiency can be improved by a factor of 1.2 by adopting emitters that are horizontally aligned with respect to the isotropic emitter layer [77]. This discovery is highly relevant to reports on efficient LEDs with dot-in-dot emitters that are typically organized horizontally [104-105].

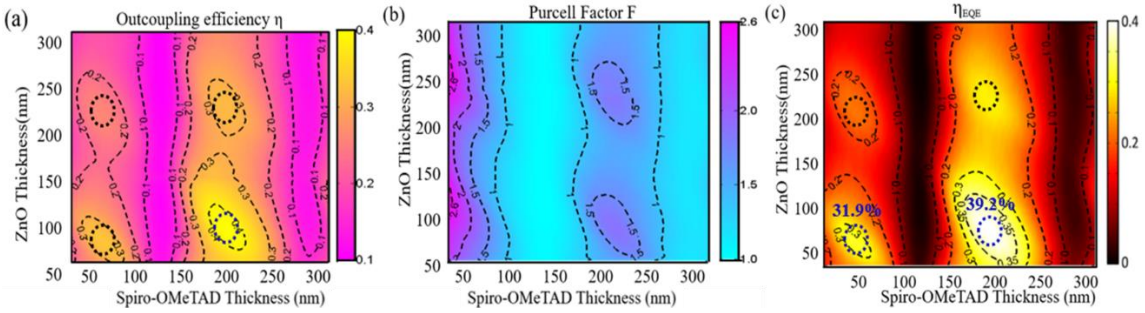

Figure 3.5 (a) Outcoupling efficiency η, (b) Purcell factor F, (c) ηEQE of PeLED as functions of ZnO and Spiro-OMeTAD thicknesses at emission wavelength 540nm (Ag=100nm, ITO=200nm, CsPbBr3=40nm).

In the quest towards a maximized η_{EQE}, the role played by the thickness of each layer forming the PeLED was also carefully analysed (with the exception of Ag, whose thickness, equal to 100nm, is much larger than the photon skin depth in the visible range -around 20nm- which implies full light absorption) while maintaining q=0.9. Here, we analysed in detail how the layer thicknesses impact outcoupling efficiency (η), the Purcell factor, and external quantum efficiency from the various possible coupling channels that the generated photons are coupled to: outcoupled through the transparent electrode, or lost in substrate, plasmonic, or waveguided modes. Firstly, we explored the two charge transport layers thicknesses with respective fixed thicknesses of ITO and perovskite at 200 nm and 4 0nm, because their thicknesses are up to the non-photonic aspects, such as obtaining efficient and balanced charge injection. Figure 3.5

clearly shows that the outcoupling efficiency η (Figure 3.5a), the Purcell factor (Figure 3.5b) and η_{EQE} (Figure 3.5c) can be optimized through the tuning of the layer thicknesses of ZnO and Spiro-OMeTAD, and there are four η_{EQE} maxima (highlighted by the dashed circles in the figure), with two of them being the most important. The first one corresponds to η_{EQE} equal to 31.9% (full blue circle in figure 3.5c), achieved for Spiro-OMeTAD and ZnO thicknesses of 50 nm and 4 0nm, respectively. And the second and most dominant peak is 40% (full blue circle in figure 3.5c) when the thicknesses of Spiro-OMeTAD and ZnO are equal to 190 nm and 55 nm. Moreover, it is apparent from the figures that these photonic parameters are drastically affected by the Spiro-OMeTAD thickness due to the interaction between the emitter dipole and the metal cathode, whereas the influence of ZnO thickness fluctuates slightly. This is because the location of the Spiro-OMeTAD layer is between the perovskite emitter and the metallic cathode. This configuration can represent an ideal cavity, with the cathode (Ag) a good reflector in the visible range. For this reason, the Spiro-OMeTAD thickness plays an important role in the formation of constructive interference in the PeLED cavity. However, it should be remembered that the thicker the ETL (or HTL) the longer the time required for the electrons to reach their destination. Therefore, the thickness of ETL/HTL is required to be as thin as possible. Thus, only the previous values are sufficiently thin for charge injection.

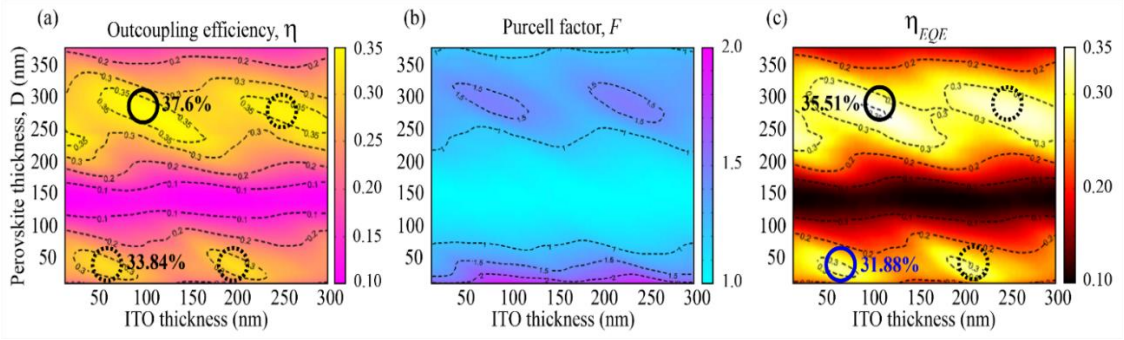

Figure 3.6 (a) Outcoupling efficiency η, (b) Purcell factor F, and (c) η_{EQE} of PeLED as functions of ITO and perovskite thicknesses at emission wavelength 540nm (Ag=100nm, Spiro-

OMeTAD=50nm, ZnO=40nm). Isotropic dipoles distribution is assumed. The circles represent local maxima.

Furthermore, with the fixed thicknesses of the two charge transport layers, we address the effects of the perovskite emitter layer and ITO layer thicknesses on the outcoupling efficiency, Purcell Factor, and external quantum efficiency at emission wavelength 540nm with an isotropic dipole distribution, as described in Figure 3.6. Similarly, there are four local maximums be noticed (highlighted by the continuous/dashed circles in the Figure). These maxima are related to the waveguide mode formed inside the perovskite and ITO layers, and compared with ITO, these values are strongly dependent on the thickness of the perovskite. The variation of the perovskite thickness can lead to the outcoupling efficiency increase remarkable from 0.1 up to 0.38 at resonance (a factor of 3.8, complete circle in Figure 3.6a). This is because the Purcell factor is determined by the layer thicknesses (see Figure 3.6b), and so impact the performance of the LED as photonic cavity. The colour map of the external quantum efficiency in Figure 3.6c manifests maxima in similar regions and it is consolidates that the performance of the LED can be remarkable improved though optimizing the layer thickness, resulting in over 35% efficiency for thick perovskite layers (thickness equal to 280nm, full black circle in Figure 3.6c), 31.88% efficiency for thin perovskite layers (thickness equal to 40nm, full blue circle in Figure 4.6c), while the efficiency of the mismatch configuration is only 10%. Therefore, the performance of the PeLED device can be affected by a factor of 3 through such layer optimization. In addition, the thickness of the ITO layer can be adjusted randomly to get the highest possible external quantum efficiency, while the emitter layer thickness should be as small as possible to limit the light reabsorption process. Another consideration resulting from Figure 3.5 and 4.6 is about the actual role played by the Purcell factor F in the definition of η_{EQE}. In fact, as shown by Equations 3.1 and 3.2, the quantity F influences η_{EQE} through q_{eff}

which also depends on the quantity q ($\eta_{EQE} \propto q_{eff}(F,q)$), hence any consideration regarding the behaviour of η_{EQE} should always take into account both F and q. In particular, it should be noticed that $\lim_{F\to\infty} q_{eff} = 1$, regardless q. In the present case it was assumed q=0.9, with the maxima values obtained for F equal to 2.6 (Figure 3.5b) and 2.0 (Figure 3.6b). Interestingly, it can be observed that both these F values lead to very similar q_{eff}, around 0.95 (to be noticed that the maximum value for q_{eff} is equal to 1), namely F has limited influence on η_{EQE} with respect to q. It is indeed q that determines how fast q_{eff} can approach its own limit 1, namely the higher q is the faster the q_{eff} limit can be reached. In turn, this means also that high values of q determine a fast growth of η_{EQE} upon an increase of the Purcell factor. Vice versa, for low q values, an increase of the Purcell factor would determine only a slight growth of η_{EQE}. In this respect, Table 1 summarizes the state of the art in the PeLED field (few representative examples were chosen from a very vast literature) showing indeed that there is margin for improving the PeLED efficiency.

Furthermore, Figure 3.7 displays the behaviour of the PeLED device (the optical power generated by the dipole is coupled to different optical channels), when perovskite CsPbBr3 thickness equals to 40 nm (corresponding to one of the maxima in Figure 3.6) and 90 nm are considered (taken as comparison term) with different ITP thickness, well confirming the ideal scenario provided by the 40nm thickness. For the 40 nm perovskite CsPbBr3 film (Figure 3.7a), about 34.03% of optical power escapes into the air, which is much higher than the 19.38% of the 90 nm perovskite CsPbBr3 film (Figure 3.7b). In particular, the 40 nm perovskite CsPbBr3 case shows a 33.85% of the generated power coupled to air, with only 16.07% and 12.11% dissipated in the substrate and HTL-EML-ETL layers, respectively. Finally, 14.75% couples to SPPs, while the remaining 23.04% is absorbed by the PeLED. When the 90 nm perovskite CsPbBr3 is

considered, more than 45% of the generated power is lost in waveguide and surface plasmon modes, while only 19.38% has the chance to couple into the air. Figure 3.7c summarizes this situation showing the general PeLED behaviour upon change of the perovskite thickness. As the perovskite CsPbBr3 thickness increases from 15nm to 100nm, the emission to air of the PeLED raises to its maximum value (for perovskite film thickness equal to 40nm) and then gradually reduces.

Table 3.1 Summarizes the state of the art in the PeLED field (few representative examples were chosen from a very vast literature) showing indeed that there is margin for improving the PeLED efficiency

Perovskite emitter	**PLQY (%)**	**Maximum EQE (%)**	**Refs**
CsPbBr3	80	20.3	[106]
FAPbI3	>50	19.6	[85]
FAPbI3	70	20.7	[107]
$FA_{1-x}GA_xPbBr_3$	93.3	23.4	[83]
CsPbBr3	90	31.7 (39% for thick Spiro-OMeTAD)	This work

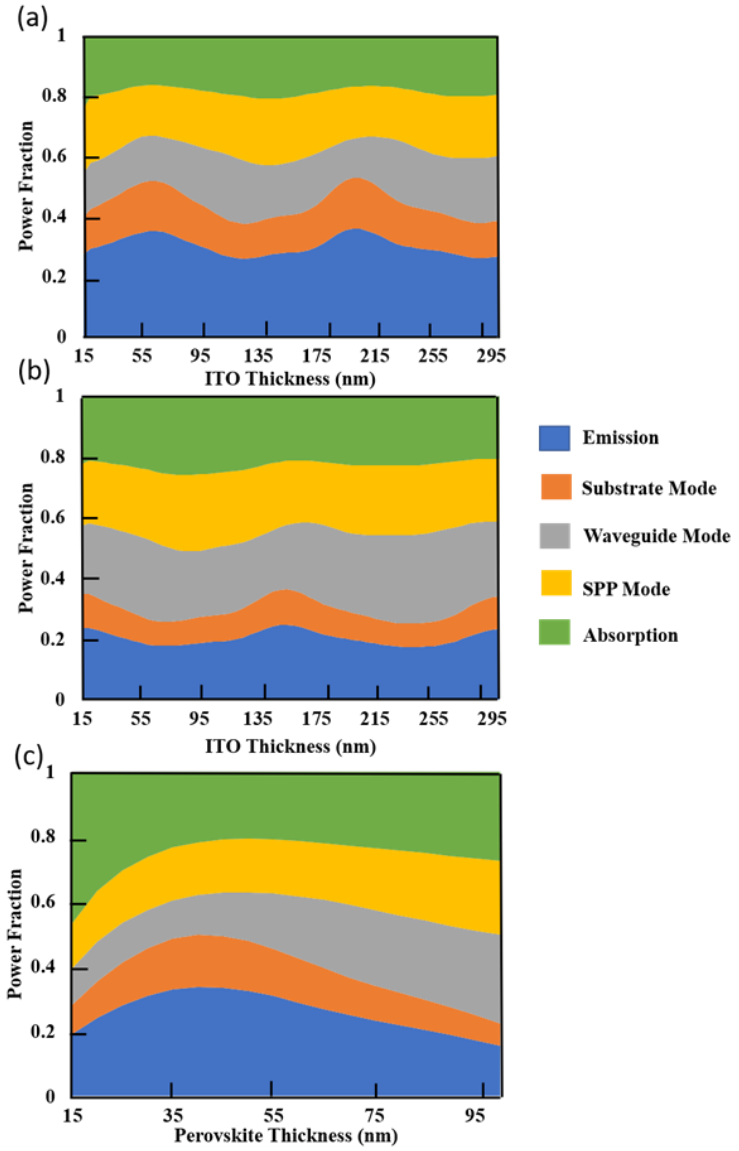

Figure 3.7 Power distribution in different optical modes of the PeLED with an isotropic dipole for various ITO thickness at emission wavelength 540nm. The thickness of the perovskite layer is fixed as 40nm (a) and 90nm (b). (c) Power distribution in different optical modes for various perovskite thicknesses at emission wavelength of 540nm. For all figures an isotropic dipole was considered with ITO thickness equal to 200nm and PLQY equal to 0.9.

Finally, it is emphasized again that the impact of only horizontal dipole excitation on the whole performance of the PeLED device. In this aspect, Figure 3.8 shows that the maximum η_{EQE} of 45.2% for the thick perovskite layer (280 nm) considering all

horizontal dipoles, and around 25% enhancement with regard to the isotropic case (Figure 3.6). The same situation also occurs for the thin perovskite layer (40 nm) with a maximum strong η_{EQE} of 37.8% vs. 31.9% obtained for the isotropic dipole condition. In addition, the significant variation in η_{EQE} with the geometric parameters should be highlighted. The minimum value is around 4%, corresponding to the off-resonance perovskite thickness (about 120 nm) and the aforesaid maxima is 45.2%, therefore the overall variation is close to 10 times.

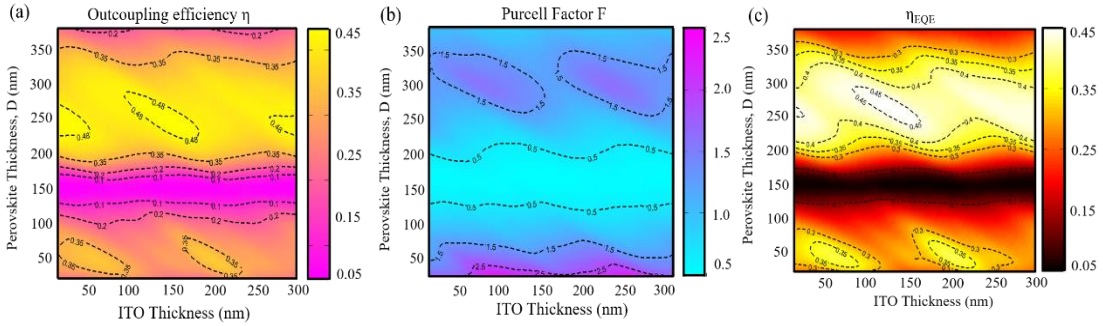

Figure 3.8 (a) Outcoupling efficiency η, (b) Purcell factor F, (c) η_{EQE} of PeLED as functions of ZnO and Spiro-OMeTAD thicknesses at emission wavelength 540nm (Ag=100nm, Spiro-OMeTAD=50nm, ZnO=40nm). For thin perovskite layer (40nm), the maximum for η_{EQE} is 37.8% (ITO layer equal to 200nm) while for thick perovskite layer (280nm) it is found to be equal to 45.2% (ITO layer equal to 110nm). For both situations the thicknesses of the remaining layers are 100nm, 50nm, 40nm for Ag, Spiro-OMeTAD and ZnO, respectively. The quantity ρ= 0.6 for all simulations.

3.4 Chapter Summary

In summary, we carried out a detailed analysis of the photonic characteristics of the layered LEDs, taking a typical PeLED structure as an example. Here the main parameters characterizing the LED, that are the dipole orientation of the emitters, the outcoupling efficiency η, the Purcell factor F, the effective radiative quantum yield q_{eff} and the external quantum efficiency η_{EQE}, are defined and analysed. Our finite element

calculated results indicate that the performance of the LED can be significantly improved via optimize its photonic properties, and we presented a strategy on how to achieve this through careful tuning of the thicknesses of the layers that compose the LED. Taking into account that the improvement of these materials has reached its limit, with the photoluminescence quantum yield of the emitter layer close to unity and efficient and balanced charge injection through cleverly customizing the energy band structure of the LED, our work outlines complementary approaches to further improve the performance of LED series based on solution processable materials that are extremely attractive for low-cost lighting devices.

Chapter 4: Effect of Multilayer Nanopatterning in Perovskite Light-Emitting Diode

Due to a multiple range of detrimental interactions, such as generation of local modes, either surface plasmon-like or optical modes, ohmic losses, or total internal reflection caused by refractive index mismatch, light-emitting diodes (LEDs) are presently not exploited to their full potential. In this work, we investigate the implications of interface modifications emerging at the electron-transport interface on the overall performance of perovskite-based LEDs, called PeLEDs. In particular, we are interested in the integration of photonic nanostructures while maintaining the optical properties of the material. Our simulated results indicate that using specially designed multilayer nanopatterns can dramatically improve the Purcell factor and the outcoupling efficiency, thereby enhancing the external quantum efficiency by a factor of 2 relative to the nanopattern-free PeLEDs. According to these findings, utilizing morphological patterning to improve LED performance is a viable strategy to improve the performance of PeLEDs, analogous to other light emission techniques.

4.1 Introduction of Patterned LED Development

From chapter 3, we know that the EQE of the PeLED device has risen from 0.01 [80] to 28.2% [108] now. However, approximately 70% of the emission power is still wasted in the perovskite LED structure, via secondary energy channels, owing to i) non-radiative recombination, ii) refractive index mismatch between the emitter layer and other transporting layers in the PeLED, and iii) total internal reflection at the substrate (typically glass) and ITO layers, [82, 85, 109-110], and iv) the formation of surface plasmon polaritons (SPPs)-like modes. Currently, most research aimed at improving the quality of PeLED devices is focused on reducing the amount of non-radiative charge recombination by improving the surface morphology and chemical composition of the

perovskite layer.[89,111–112] However, few reports have explored the possibility of preventing power loss due to total internal reflection by embedding photonic structures of various morphologies such as nano-scattering nanopatterns, [113-114] wrinkled substrates, [115] microlens arrays, [82] moth-eye nanopatterns, [116] hyperbolic metamaterials (HMMs), [107] thereby improving the performance of the PeLED device. Furthermore, research on improving the overall performance of LEDs by minimizing loss due to SPP formation is even rarer. In fact, it is proposed that for PeLEDs, the same strategy used in the photoluminescence field, where various nanophotonic methods and nanostructures have been used to enhance photoluminescence, should be utilized [117-119]. Such approaches have been effective in OLEDs [118–119] and in the design of novel light-emitting surfaces, where different nanophotonic approaches and nanostructures have been used to boost photoluminescence.

Within the broader search for improved PeLED performance, it was recently reported that flat PeLED structures with enhanced η_{EQE} in the chapter 3, with layered metal-insulator nanocavities are capable of boosting the spontaneous emission - Purcell effect - of perovskite layers. [77] In this chapter, we investigate the photonic processes that occur in a multilayer PeLED device attributed to the presence of nanopatterns, and we evaluate the conditions under which the PeLED performance can be enhanced over a flat PeLED. For the multilayer PeLED structure, we assume efficient photon generation in the emitting layer defined by an internal quantum yield q of 0.9, [82], a charge injection balance of 1, [110], and a singlet/triplet capture ratio S/T = 1 [82], and the situation changes slightly when a periodic nanopattern is considered. In this respect, the periodic nanopattern is integrated inside the electron transport layer, with the aim of reducing the power leakage caused by the formation of SPPs. This form of power loss is indeed the most challenging to tackle, for example, compared to other radiation losses such as total internal reflection. In this respect, we identify the Purcell factor and the

outcoupling efficiency η_{out} as the two main quantities to be evaluated for minimizing the internal losses of the PeLED and increasing its light emission, all summarized in the η_{EQE}.

4.2 Theoretical Method on Patterned PeLED

4.2.1 Patterned PeLED Diagram

Similar to the flat PeLED device in chapter 3, Figure 4.1a shows the cross section of a standard flat PeLED device composed of different materials, whose thicknesses from the bottom to the top are of 700nm, 200nm, 100nm, 30nm, 100nm, 100nm for glass, ITO, poly-TPD, CsPbBr3(with ρ= 0.6), TPBi and Ag. Here, glass acts as a protective layer. ITO and Ag film are still used as the transparent anode and metal cathode, while the perovskite CsPbBr3 film is sandwiched between TPBi as an electron-transport layer (ETL) and poly-TPD as a hole-transport layer (HTL) in the PeLEDs. The aforementioned geometrical values were chosen with the aim of a maximized η_{EQE}, where the emitting layer was chosen thin enough to minimize the distance between the Hertzian dipole emitter located at its centre (red dot in figure 3.1) and the ETL/HTL layers, condition which realizes an improved Purcell factor, and a TPBi layer whose dimensions had to accommodate the multilayer structure shown in Figure 4.1b, yet falling in the standard thickness values for PeLED devices. Moreover, the refractive indexes of these materials are shown in table 4.1. Herein, Figure 4.1b describes a modified version of the PeLED device depicted in Figure 4.1a, where a metal-insulator multilayer nanopatterns formed by a periodic Ag-Al2O3 configuration is embedded in the electron transport layer (ETL)-to reduce SPP loss, resulting in the performance further enhancement of the PeLED device. In particular, a 2-layers structure (that is, two times Ag-Al2O3) with Ag thickness tm = 10 nm and Al2O3 thickness td ~ 30 nm followed by a final Al2O3 layer of 15 nm, is studied. The periodicity is selected as P =

330 nm with width-periodicity ratio W/P = 0.2 (i.e., W = 66 nm). The reason for selecting P = 330 nm is to realize an energy/momentum mismatch between the radiation emitted by the dipole (λ= 540 nm) and the SPPs at the Ag/TPBi interface, thereby minimizing the formation of SPPs, hence determining an improved performance of the PeLED. Furthermore, a hertzian dipole (red dot) in the centre of the perovskite layer works as the light source of emission wavelength 540nm.[92] All the calculations are also performed through the PeLED simulation model introduced in Chapter 3.

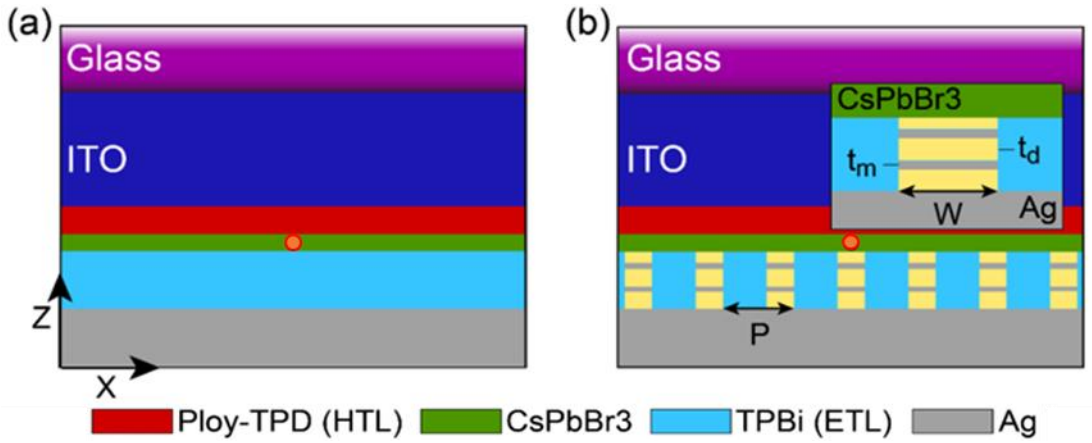

Figure 4.1 Schematics of flat PeLED (a) and Ag-Al2O3 multilayer nanopattern PeLED (b) with, from bottom to top, t_d ~ 30 nm, t_m = 10 nm, t_d ~ 30 nm, t_m = 10 nm, t_d = 15 nm (2-layers structure), together with the emitting dipole located at the centre of the perovskite layer. The insets in (b) illustrate the modification of the TPBi layer through an Ag-Al_2O_3 multilayer.

Table 4.1 The real (n) and imaginary (k) component of the refractive indexes of the material consists of the PeLED device.

Materials	n	k	reference
Ag	0.0982	3.292	[77]
TPBi	1.734	0	[121]
CsPbBr3	2.005	0.0282	[96]
Poly-TPD	1.775	0.0534	[121]
ITO	1.931	0.002	[99]
Glass	1.52	0	[77]

4.2.2 Theoretical Method

To evaluate the overall performance of the PeLED devices, the external quantum efficiency η_{EQE} (e. g., the ratio between the number of photons emitted by the PeLED and the number of injected charge carriers) is adopted, which can be calculated though Equation 3.1. The outcoupling efficiency η_{out} (η in chapter 3) is described as the ratio between the number of photons produced by the emitter (perovskite) that reach the free space around the PeLED to the total number of photons generated by the emitter, which can be computed as:

$$\eta_{out} = \frac{Number\ of\ photons\ reaching\ the\ free\ space\ per\ second}{Number\ of\ photons\ emitted\ from\ the\ emitter\ region\ per\ second} = \frac{P_{out}}{P_{total}} \tag{4.1}$$

Where P_{out} denotes the optical power emitted by the active region (i.e., the dipole in the perovskite layer) and reaching the free space (air) surrounding the PeLED, and P_{total} is the total power emitted by the dipole. In a flat PeLED scenario γ is depended on the materials forming the transport layers and their thickness, with maximum value of 1. However, in this work, we will address the case in which a periodic nanopattern is inserted. within the Electron Transport Layer (ETL), so that we define the charge injection balance γ as:

$$\gamma = 1 - \frac{\mathrm{W}}{\mathrm{P}} \tag{4.2}$$

Where P refers the periodicity and W denotes the width of the modulation. Expression (4.2) accounts for the reduction of transport material caused by the insertion of a periodic nanopattern with regard to a flat design (see Figure 4.1a, b). According to Equation 3.2 and 3.3, the Purcell factor (PF) of the nanopatterned PeLED can be also calculated.

Finally, the enhancements of PF, η_{out} and η_{EQE} are defined as following expression:

$$\mathrm{PF}_{enh} = \frac{\mathrm{PF}_{patterned}}{\mathrm{PF}_{flat}} \tag{4.3}$$

$$\eta_{out,enh} = \frac{\eta_{out,patterned}}{\eta_{out,flat}} \quad (4.4)$$

$$\eta_{EQE,enh} = \frac{\eta_{EQE,patterned}}{\eta_{EQE,flat}} \quad (4.5)$$

Where $PF_{patterned}$, $\eta_{out,patterned}$ and $\eta_{EQE,patterned}$ denote the Purcell factor, outcoupling efficiency, and external quantum efficiency of the multilayer nanopatterned PeLED while PF_{flat}, $\eta_{out,flat}$ and $\eta_{EQE,flat}$ are the Purcell factor, outcoupling efficiency, and external quantum efficiency of the flat PeLED.

4.3 Effect of the Multilayer Patterns

Figure 4.2a-b describes the electric field distributions corresponding to the structures presented in Figure 4.1a-b. As illustrated in Figure 4.2a, the electric field in the flat PeLED device is localized mainly at the Ag/TPBi interface, resulting in the optical energy gradually being dissipated into the metallic Ag film, predominantly by the formation of SPPs. In turn, this means the efficiency of the flat PeLED is decreased since the formation of any localized mode, such as SPPs, reduces the photons available for the outcoupling efficiency. This behaviour particularly true for the vertical dipole, as expected by observing the electric field components in Figure 4.3. Indeed, Both Ex- and Ez- components exhibits an obvious SPPs formation in the case of vertical dipole oscillation. Vice versa, for the horizontal dipole excitation, the SPPs generation is mainly observable in the Ex-component, while the strong far-field emission is related to the Ez-component.

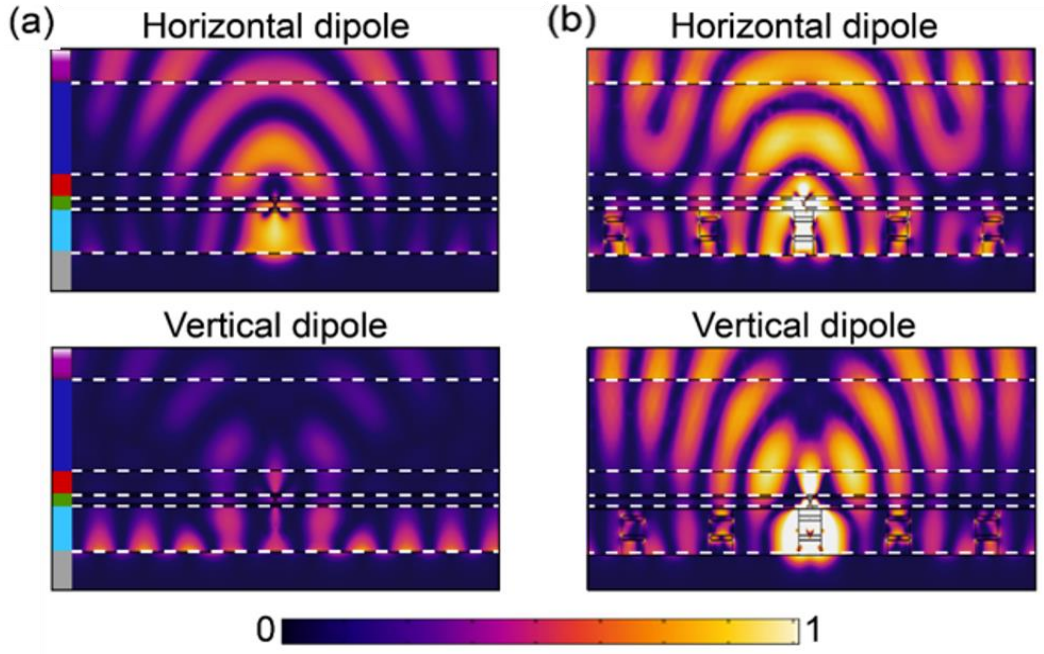

Figure 4.2 The electric field norms distribution of the flat PeLED (a) and Ag-Al_2O_3 multilayer PeLED (b) with, from bottom to top, t_d = 32.5 nm, t_m = 10 nm, t_d = 32.5 nm, t_m = 10 nm, t_d = 15 nm (2-pairs structure). Two different excitation conditions are considered for all structures: horizontal dipole and vertical dipole. The emitting dipoles are located at the centre of the simulative domains (red dots). For all figures is assumed λ= 540 nm, q = 0.9, γ = 1, $\eta_{S/T}$ = 1. The dashed lines highlight the interfaces among the different layer materials. The simulations were run with COMSOL Multiphysics, a finite element method-base software.

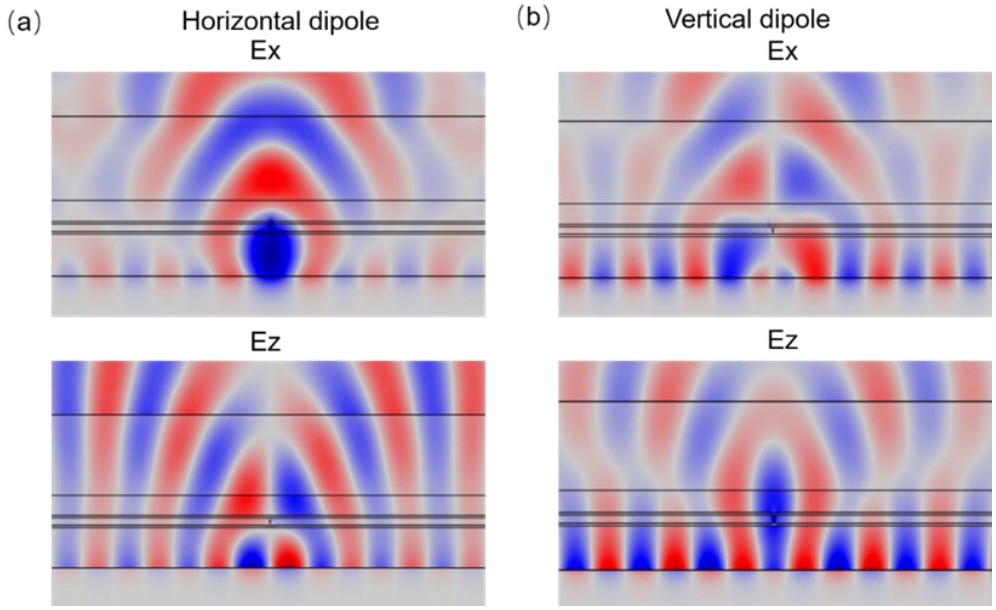

Figure 4.3 Distribution diagram of the electric field components (Ex, Ez) with a horizontal

dipole (a) and vertical dipole (b) at resonance wavelength 540nm. The schemes show the flat PeLED structure. The scale colour is the same for both figures (red: positive, blue: negative).

In comparison to the flat PeLED, Figure 4.2b directly demonstrates the influence of the multilayer-based structure on the formation of the SPPs. For both dipole orientations, the figure illustrates a substantial preference for maintaining an electric field distribution toward the far-field (top of the Figure). This results in a significant decrease in SPPs at the interface when compared to the flat PeLED device, hence minimizing the plasmon-related losses. Indeed, a suitable wavelength-periodicity mismatch, achieved by utilized P = 330 nm at = 540 nm, reduced the coupling into SPPs, therefore increasing the radiation pattern. Furthermore, the radiation pattern highlights the fingerprint of the dipole orientation, with a node along Z direction under vertical excitation.

To understand of the effect of the multilayer metal-insulator nanopattern on the PeLED performance, we performed a theoretical evaluation of the cavity Purcell factor and outcoupling efficiency enhancement when the Ag-Al2O3 multilayer parameters were modified. The results are combined to determine the external quantum efficiency of the PeLED device. Furthermore, in attempt to address actual conditions, an isotropic dipole is considered to reflect the emission of a realistic emitter layer, whose total radiative power can be calculated as follows:

$$P_{total\ rad} = \frac{P_{\perp} + 2 * P_{\parallel}}{3} \tag{4.6}$$

Where ⊥ and || denote the dipole orientation, either perpendicular (⊥, vertical) or parallel (||, horizontal) to the flat interface. In this chapter, we then analysed the contributions of various decay channels in the Ag-Al2O3 multilayer patterned PeLED. Similar to the flat PeLED, different optical channels can be identified in the nanopatterned PeLED structure: direct emission (outcoupled into the air), SPP mode coupling (at the Ag/TPBi interface), and other localized optical modes (e.g., waveguide

mode, absorption, etc.). Here, we will concentrate on first two optical decay channels in this section because we are primarily interested in the impact of the interface modification on SPP loss and direct emission (i.e., outcoupling efficiency). In our numerical calculation, according to Equation (4.1), the outcoupling efficiency under isotropic dipole excitation is proportional to P_{out}, which can be calculated by integrating the power flow through the air-glass interface, and similar the power coupled with the SPPs loss is considered to be divided into two parts: the power concentrated at the Ag/TPBi interface and the power absorbed by the Ag film. Therefore, the SPPs loss is calculated as the ratio of the SPPs power loss P_{spp} to the total emitted power P_{total}, or P_{spp} / P_{total}. As shown in Figure 4.4, our initial calculation results obvious depicts that the SPP loss drops from 19.94% for the flat PeLED to 8.12%, achieved from the 2-layers Ag-Al2O3 multilayer nanopatterned PeLED under the isotropic dipole, whereas outcoupling efficiency has increased from 11.86% to 33.29%. These findings support our previous statement that a pattern modification at the Ag/TPBi interface helps to reduce SPP loss, thereby improving the performance of the PeLED.

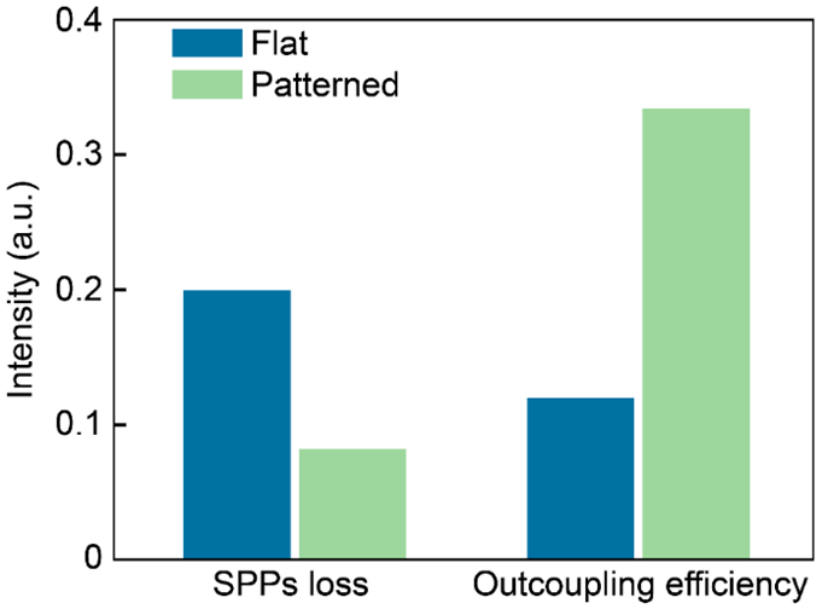

Figure 4.4 The photons lost due to the formation of SPPs in the PeLED is compared to the

outcoupling efficiency for both the flat and patterned (2-layers) PeLED configurations. An isotropic dipole emitting at 540 nm is considered. For the patterned configuration, the Ag thickness is 10 nm, the periodicity P is 330 nm, and the ratio W/P is equal to 0.2.

In special, we explore the impact of the number of metal-insulator layers on the improvements of the Purcell factor (PF), outcoupling efficiency η_{out} and η_{EQE} as compared to the flat PeLED. Figure 4.5a depicts the findings for an isotropic dipole at = 540 nm while maintaining the thickness of the ETL constant and equal to 100 nm with tm = 10 nm. Interestingly, the figures reveal that as the number of metal-insulator layers falls, the maximum of η_{out} grows in amplitude until it reaches a peak at around 2-layers (similar considerations apply to PF and, in turn, to η_{EQE} enhancements). This behaviour can be explained by observing the Poynting vector formed inside the TPBi layer that determining the propagation of the radiation. Particularly, Figure 4.5b illustrates the pointing vector owns a strong component along Z direction (i.e., toward the top of the structure) for the two-layer configuration, which is helpful for maximizing η_{out}. When the number of Ag-Al2O3 layer is varied, it can be seen a strengthening of the pointing vector in X axis (that is, parallel to the interface), a situation preventing the emission of radiation into the far field. As a typical example, Figure 4.5c displays the 5-layer arrangement in which the horizontal orientation of the Poynting vector results in a decrease PF, η_{out}, and η_{EQE} values as compared to the 2-layer configuration. Furthermore, it should be emphasized that for all of the Ag-Al2O3 layers investigated, the η_{EQE} gives a result around twice that of the flat PeLED configuration, indicating a 100% increase.

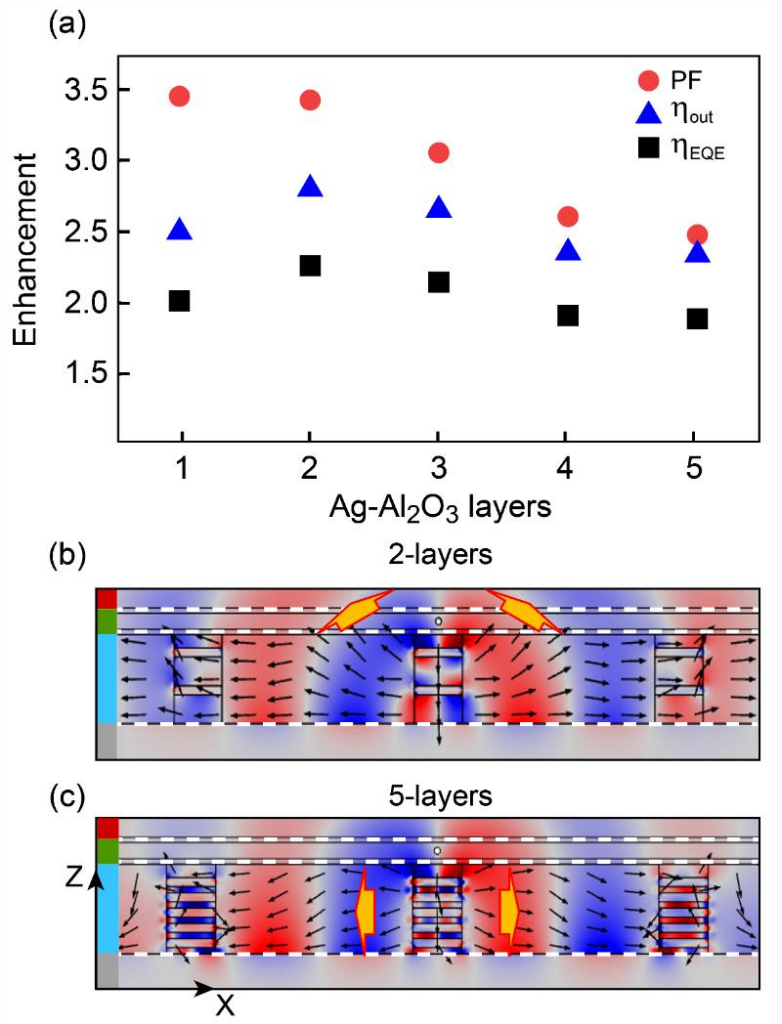

Figure 4.5 (a) Purcell factor PF, outcoupling efficiency η_{out} and external quantum efficiency η_{EQE} enhancements upon change of the number of the Ag-Al_2O_3 layers when an isotropic dipole at 540 nm is considered. The thickness of the Ag layer is kept constant at 10 nm with the total ETL thickness equal to ~ 100 nm. In (b) and (c) are shown the Ez-component of the electric field (blue and red colours) together with the Poynting vector (black arrows) inside and in proximity of the TPBi layer for the 2- and 5-layers configurations, respectively. Similarly, to Figure 4.3, the colour bars at the left-hand side of the figures, define the materials forming the layers whose interfaces are highlighted by the white dashed lines. The yellow arrows summarize the main directions of the Poynting vector (Z direction in (b), X direction in (c)). A horizontal dipole was assumed as light emitter (for the vertical dipole –not shown- both 2- and 5-layers configurations show a Poynting vector mostly oriented in X direction). In (b), the Al_2O_3 thickness is ~30 nm (top layer 15 nm) while in (c) it is ~7 nm (top layer 15 nm). For all cases, a periodicity P = 330 nm and a ratio W/P = 0.2 was assumed.

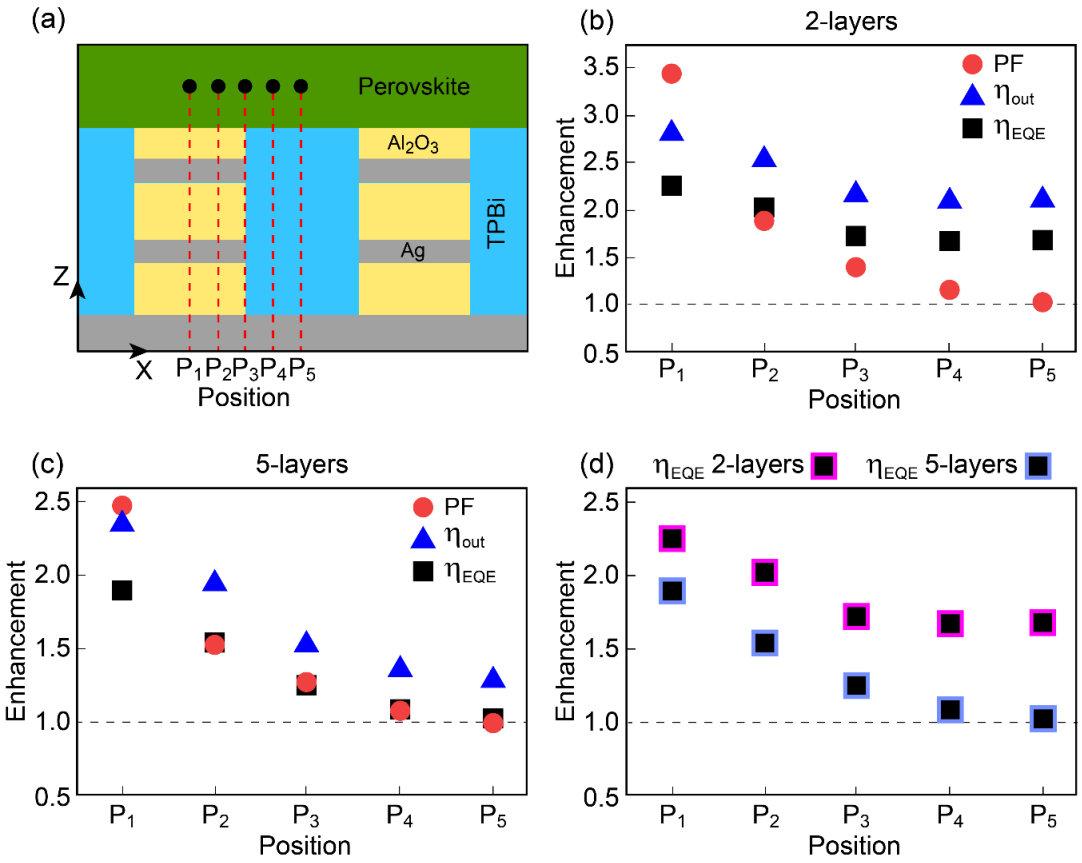

Figure 4.6 Purcell factor PF, outcoupling efficiency η_{out} and external quantum efficiency η_{EQE} enhancements upon modification of the position of the Hertzian dipole. (a) Sketch showing 5 different positions of the dipole, from the centre of the Ag-Al2O3 multilayer (P1) to the centre of TPBi (P5; the dipole is always located in the middle of the perovskite layer but shifting along X direction). (b) and (c) describe the 2-layers and 5-layers configurations, respectively, while in (d) the η_{EQE} for 2- and 5-layers configurations are plotted together for easy comparison. The dashed line represents the flat PeLED values (enhancement equal to 1). The dipole emission wavelength is λ = 540 nm with isotropic orientation, the periodicity P = 330 nm and W/P = 0.2.

A critical assumption for the nanopatterned PeLED is to consider the Hertzian dipole positioned in the centre of the perovskite layer and parallel to the Ag-Al2O3 multilayer's vertical axis. But this assumption is not indicative of an actual scenario, in which a large number of Hertzian dipoles are dispersed uniformly inside the perovskite layer. For this reason, we examined the PeLED performance for five different positions

(from P_1 to P_5), as shown in Figure 4.6a. Particularly, the considered places span the whole periodicity, from the canter of the Ag-Al2O3 multilayer (P_1) to the middle of the TPBi (P_5). The enhancement of the Purcell factor (red circle), η_{out} (blue tringle), and η_{EQE} (black square) of the multilayer nanopatterned PeLED relative to the flat PeLED are shown in Figure 4.6b and 4.6c. Two configurations are considered: 2- layers (b) and 5-layers (c). To comparison easily, Figure 4.6d depicts the η_{EQE} for both configurations. The highest values are achieved at P_1 due to the significant effect of the presence of the Ag-Al2O3 multilayer directly underneath the dipole. In fact, as illustrated in Figure 4.7, the Ag-Al2O3 structure produces a horizontal-like dipole on the top of the structures, which is benefit to boost the radiation emitted by the PeLED. In contrast, when the dipole is placed in between two adjacent multilayers, i.e., Position 5, no local dipole-like mode is formed, determining the decreased radiative emission. Significantly, the η_{EQE} enhancement is always greater than 1 in all five positions, that is positive response are returned at all positions from the nanopatterned PeLED, thereby reflecting a better performance than the flat arrangement (Similar reasoning applies to the Purcell factor and outcoupling efficiency enhancement).

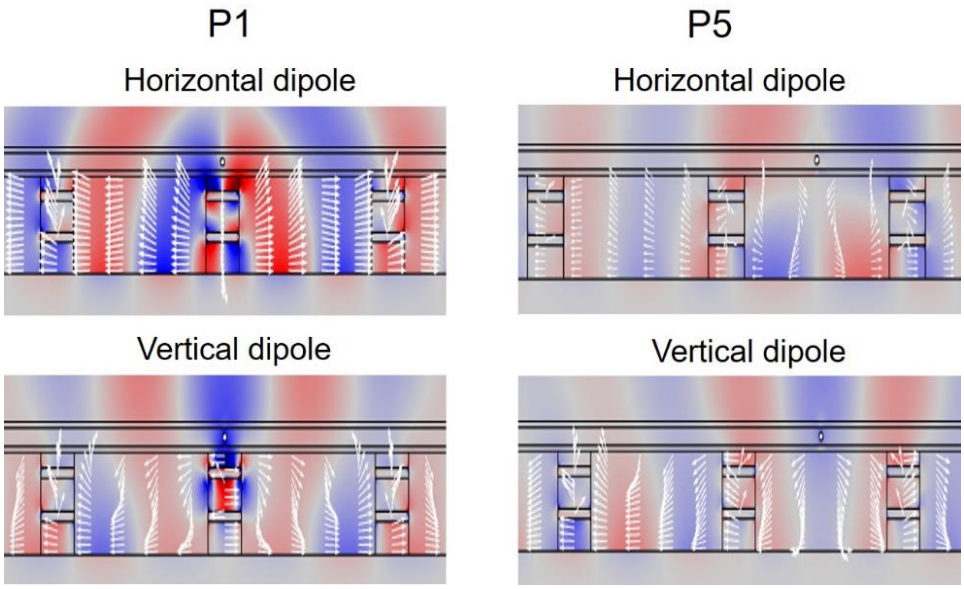

Figure 4.7 Radiation pattern (Ez) and Poynting vector (white arrows) for 2-layers structure

when P1 and P5 positions are considered for the emitting dipole (a similar behaviour occurs for the 5-layers configuration –not shown-).

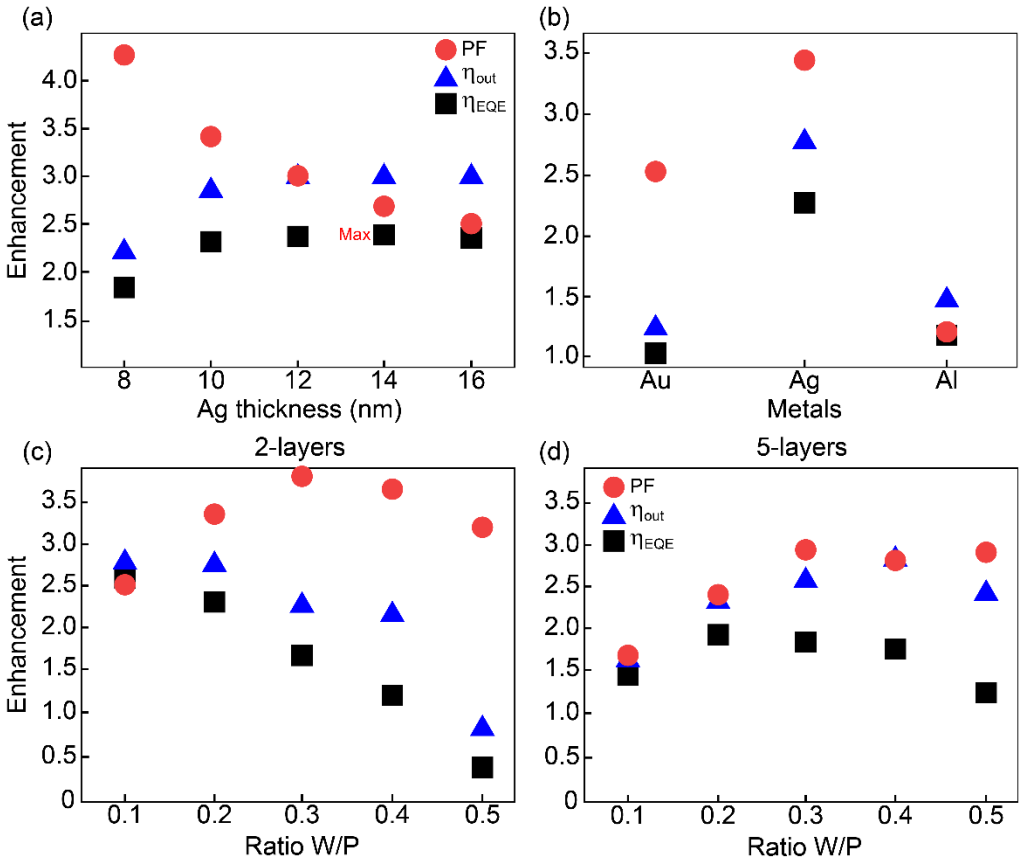

Figure 4.8 Purcell factor PF, outcoupling efficiency η_{out} and external quantum efficiency η_{EQE} enhancements upon modification of geometrical and material parameters. (a) The Ag layer thickness in the Ag-Al2O3 multilayer is modified from 8 nm to 16 nm. (b) Three different metals, Ag, Au and Al, are employed in the multilayer. In both (a) and (b) a 2-layers configuration is assumed with W/P = 0.2. (c) and (d) show the effect of the ratio W/P when tm = 10 nm in the Ag-Al2O3 multilayer, for 2- and 5-layers, respectively. For all figures it is assumed: P1 position, period P = 330 nm, total TPBi thickness constant at 100 nm, and isotropic dipole emitting at 540 nm.

Furthermore, the impact of Ag thickness in the Ag-Al2O3 multilayer was investigated, with keeping a fixed ETL thickness of 100 nm, as well as the influence of the W/P ratio. In this regard, Figure 4.8a compares five different types of Ag-Al2O3 2-layer structures, each with a different Ag thickness ranging from 8 nm to 16 nm (The Al2O3 thickness

was adjusted to keep the ETL thickness constant at 100 nm). This figure not only shows the best performing situation (max η_{EQE}) at tm = 14 nm, but it also displays a significant sensitivity to a little modification of Ag thickness, with η_{EQE} enhancement changing from ~1.8 (tm = 8 nm) to ~2.4 (tm = 14 nm) in only 6 nm Ag variation. In particular, the figure clearly demonstrates a common behaviour well associating the three factors PF, η_{out}, and η_{EQE}, according to Equations (4.1) -(4.4). In this respect, η_{EQE} follows the behaviour of η_{out}, which is only marginally impacted by PF, reaching a maximum at around 10 nm Ag thickness and then starting to decline at 16 nm. Actually, this is an interesting respect, since it might be expected that thick Ag layers would perform worse than thin layers owing to their loss nature. However, as seen in Figure 4.5, the multilayer structure may support local modes that alter the emission of the light from PeLED, modes that are dependent on the layer counts and, as demonstrated here, also on tm.

In addition to the thickness of the metal layer inside the multilayer, we also considered the role of the metal employed. Figure 4.8b compares the PeLED performance when using 2-layers Au-Al2O3, Ag-Al2O3, and Al-Al2O3. There is a noticeable improvement in PF, η_{out}, and η_{EQE} At 540 nm when Ag is used, whereas Au and Al provide similar results (Al being slightly better).

Figures 4.8c and 4.8d demonstrate the effect of the W/P ratio from 0.1 to 0.5 on a 2- and 5 structure, respectively. It's noteworthy to note that η_{EQE} gradually decreases as the W/P ratio increases, regardless of the fact that the maximum value for PF is obtained at W/P = 0.3. The reasoning is attributed to using a charge injection balance that is proportional to the W/P ratio, as defined in Equation (4.3), in order to account for the diminishing TPBi layer (ETL) as W rises.

Consequently, despite the best results obtained at tm = 14 nm and W/P = 0.2, we chose tm = 10 nm and W/P = 0.2 as reference parameters, considering the difficulty in

fabricating multilayer structures with an Ag thickness precise down to the single nanometre and with multilayers as thin as 33 nm (corresponding to P = 330 nm). Therefore, we picked a configuration which is less performant but more feasible than the ideal.

Table 4.2 Performance comparison for the flat and patterned PeLEDs.

Flat PeLED	**Patterned PeLED**	**Enhancement factor**	**Reference**
$\eta_{EQE} = 16.5\%$	$\eta_{EQE} = 18.5\%$	1.12	[113]
$\eta_{EQE} = 13.4\%$	$\eta_{EQE} = 20.3\%$	1.51	[85]
$\eta_{EQE} = 12.29\%$	$\eta_{EQE} = 17.94\%$	1.46	[121]
$\eta_{EQE} = 21.7\%$	$\eta_{EQE} = 27.6\%$	1.27	[115]
$\eta_{EQE} = 15\%$	$\eta_{EQE} = 18\%$	1.2	[122]
$\eta_{EQE} = 11.7\%$	$\eta_{EQE} = 26.5\%$	2.27	**This work**

Our calculations have indicated that when compared to the flat PeLED configuration, the performance of the nanopatterned PeLED is much better, regardless of Ag-Al2O3 layers number used in the ETL nanopattern. Specifically, when isotropic dipoles simulating the perovskite layers are used, the external quantum efficiency η_{EQE} improved to 2.27 when the two-layer configuration utilized. To further understand our findings, Table 4.2 summarizes our results to the enhancement factors achieved in several previous works.

4.4 Chapter Summary

In summary, we have introduced a nanostructured PeLED architecture aiming at understanding whether interface patterning could contribute to the improvement of the PeLED performance. In particular, we have considered a modification of the electron-transport layer, and we have evaluated the response of the PeLED in terms of Purcell factor, outcoupling efficiency and external quantum efficiency. Our calculations reveal the possibility to enhance all these quantities when compared to a flat reference PeLED. In particular, it was found that the best emission parameters, also associated to a feasible structure from a fabrication point of view, lead to an external quantum efficiency about 100 % higher than the corresponding value for the flat PeLED. That said, it is also suggested that for further performance improvement, nanopatterning modification of HTL should be considered as well. These findings indicate that similarly to the nanopatterning strategy adopted in the photoluminescence field, also light emitting diodes could strongly benefit from morphological modifications of the inner interfaces.

Chapter 5: Nanoscale Optical Sensor based on Gap-Plasmonic Resonance

Metallic colorimetric optical nanosensors based on surface plasmon resonances have been the target of an intensive R&D activity, owing to the large number of applications in pressure-, refractive index-, biomolecular-sensing just to mention a few. In this work, we address optical pressure/temperature nanosensors by designing and numerically simulating Metal/Insulator/Metal (MIM) nanopillar arrays covered by a metallic film. The gap plasmon frequency is particularly sensitive to the distance of the pillars to the Ag film, allowing for optical pressure/ambient temperature monitoring via the change in colour of the device. Simulation results show that the profile of the reflectance dip in the spectra, which determines the colour of the structure, strongly shifts with the distance between the nanopillars and the metallic film. Importantly, a noticeable reflectance dip shift can be achieved even upon a nanometric displacements. The colour change could be utilized to indicate the external environmental change, such as monitoring optical pressure or the ambient temperature where the sensor is located. Moreover, the sensor has extensive potential applications in chemical, biological, environmental, and medical sensing, as well as in manufacturing.

5.1 Introduction of Optical Sensors

Thanks to their unique properties, plasmonic-based devices have received growing attention over the last few decades, significantly boosting the sensitivity of the optical sensors [123−124]. The evolving of nano-manufacturing technology (e. g., such as electron beam lithography (EBL) and focus ion beam (FIB)) has completely altered the role of the metal in the creation of optical systems based on plasmonic effects, for example, surface plasmon resonances (SPRs), which is the charge density excitation

oscillation caused by the polarized light along the metal-dielectric interface under the phase-matching condition [125]. These are attractive for numerous applications in pressure- [126-127], refractive index- [128-129], temperature [130-131], gas detector [132-133], biosensing [134-135] and environmental monitoring [123]. When the size of the metallic nanostructure is less than the light wavelength, colorimetric optical sensors based on the SPR can be created [129, 136]. In recent years, plasmonic colours become a key approach and are widely used in the colour filters [137-138], colour printings [139-140], colour holograms [141] and colorimetric sensors [135], because of their advanced merits, such as extraordinary high resolution, broad colour gamut and high saturation. In 2015, Tie sheng Wu and his colleagues developed a nanometric temperature sensor based on a plasmonic waveguide with an ethanol-sealed rectangular cavity [131]. However, despite the rapid advancement of this sensor technology, the majority of optical sensors are limited to the near infrared region and their sensitivity is relatively low. In this study, we present an optical sensor based on gap-plasmonic resonances. The plasmonic resonance, manifested as a well-defined minimum in the reflectance spectra, is particularly sensitive to the distance between the MIM nanopillars and the Ag film, according to our results obtained using finite-elements simulations and finite-difference time-domain calculations. Furthermore, we investigate the impact of the geometrical factor of the sensor structure on the sensor performance. The study demonstrates that the geometrical variation can be employed to detect external parameters that alter this distance on a nanometer scale, such as force/pressure or temperature. And this sensor could also be utilized in real-time and label-free refractive index sensor with a sensitivity of 141 nm/RIU, that exposes unique colorimetric differences between different media.

5.2 Theoretical Method

5.2.1 Simulation Model of MIM Optical Sensors

Figure 5.1a depicts the 3D schematic diagram of the nanosensor. The investigated homogenized structure is composed of the 200nm periodic MIM nanopillar array on a glass substrate and an Ag film with 100 nm thickness covering the pillar array. The radius of the nanopillars is 70nm. Between the MIM nanopillar array and the Ag film, we assume an air gap of 0-15 nm. The probing light as a plane wave perpendicular to the normal direction impinges on the silver film through the substrate. All the numerical simulations are carried out by two commercial software packages (COMSOL Multiphysics based on Finite element method and Lumerical based on finite-difference time-domain method). The gap nanometric layers are meshed with a free triangular pattern with a maximum element size of 2 nm, while the top and bottom boundaries are imposed by swept-meshed Perfectly Matched layers (PML). The top and bottom boundaries are imposed swept-meshed Perfectly Matched layers (PML), while the gap nanometric layers is meshed with a free triangular texture in which the maximum element size is 2 nm. And the periodic boundary conditions are applied to make the structure appear as an array nanopillars. The plan wave excites the probing light via a classical internal port, adjacent to the upper Perfect Matched Layer domain. The dielectric properties of the Ag and Al2O3 are derived from by experimentally measured ellipsometry data. As sketched in Figure 6.1b, this geometry is implemented as an optical force /pressure sensor. A normal force/pressure on the metallic film narrows the air gap d between the MIM nanopillars and metallic film. A red-shift is clearly discernible in the corresponding second and third resonant wavelength. Moreover, the sensor could also be used as a temperature or refractive index- sensor, as shown in Figure 6.1c, when the air gap is replaced by an elastic material, whose shape or refractive index will change with the temperature variation. Additionally, all the

simulated optical reflectance spectra can be translated to the CIE chromaticity using a MATLAB code based on its chromaticity coordinate, confirming the colour gamut of the method.

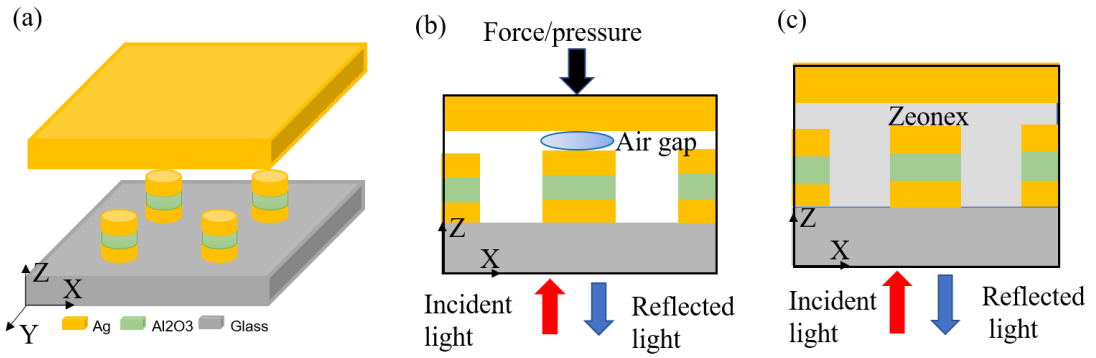

Figure 5.1 (a) A scheme diagram of the MIM nanopillar array with an Ag film reflector. (b) 2D structure of the proposed MIM-metamaterial-based force/pressure sensor. (c) 2D structure of the proposed MIM-metamaterial-based temperature/ refractive index- sensor.

5.2.2 CIE 1931 Chromaticity Coordinate

In order to further confirm the colour of the nanostructure, we calculated the structure colour utilizing the simulated reflectance spectra and the colour-matching functions defined by the International Commission on Illumination (CIE,1931) [142-143]. According to this formula, the spectral power distribution is expressed as follows:

$$P(\lambda) = I(\lambda)R(\lambda) \tag{5.1}$$

Where I(λ) represent the relative radiance spectrum of the white light source. R(λ) express the simulated reflectance spectrum. The tristimulus values X, Y and Z are determined using the following equation:

$$X = \frac{1}{K}\int_{\lambda}^{\infty} \bar{x}(\lambda)\, P(\lambda) d\lambda \tag{5.2}$$

$$Y = \frac{1}{K}\int_{\lambda}^{\infty} \bar{y}(\lambda)\, P(\lambda) d\lambda \tag{5.3}$$

$$Z = \frac{1}{K}\int_{\lambda}^{\infty} \bar{z}(\lambda)\, P(\lambda) d\lambda \tag{5.4}$$

Here, $\bar{x}$, $\bar{y}$, and $\bar{z}$ are the CIE standard observer functions. Over the visible range (from 380 to 780 nm), the integrals are calculated. The normalizing constant K is described as:

$$K = \int_{\lambda}^{\infty} y(\lambda)\, I(\lambda) d\lambda \tag{5.5}$$

The CIE chromaticity coordinate (x, y) can achieve by normalizing:

$$x = \frac{X}{X+Y+Z} \tag{5.6}$$

$$y = \frac{Y}{X+Y+Z} \tag{5.7}$$

$$z = \frac{Z}{X+Y+Z} \tag{5.8}$$

It is noteworthy that only two values of (x, y, z) are independent, because the intensity of the incident light source is normalized. According to x and y, the colour can be fixed.

5.3 Numerical Analysis on MIM-based Nanostructure

In order to study the light-matter interaction inside the nanostructure, numerical simulations are adopted here. The reflectance (R), transmittance (T) and absorbance (A) of this structure, composed of 50nm/80nm/50nm MIM nanopillars, are calculated by using the COMSOL Multiphysics & Lumerical tools, as shown in Figure 6.2a. The resonant plasmonic modes cause three minima in the reflectance spectrum at wavelength of 418nm, 484nm and 766nm. Compared the results from the COMSOL (solid lines) and FDTD (dash lines), they are consistent in the position, but there is slight difference in the values. The difference can be attributed to the dielectric constant fitting of the materials and the meshing. Figure 6.2b-d describes the magnetic field distribution near the nanopillar in ZX-plane at these resonance wavelengths, superposed with grey arrows representing the electric field vector. We can see that not only the magnetic intensity, but also the resonant spatial positions are significant different between these resonant wavelengths, revealing distinct resonant modes. At the

first resonance at 418nm, the magnetic field is mainly dispersed at the interface between the metal and dielectric in the MIM pillars. A considerable portion of the magnetic field is still restricted in at the margins of the metal disks at the second resonance at 484nm, but the field enhancement at the centre of the metal/dielectric interfaces becomes stronger. For the third resonance at 766nm, nearly all the magnetic field is concentrated into the gap between the MIM nanopillars and the Ag film, leading to a substantial local enhancement. And the gap plasmon at this third resonance can be exploited for the visible-infrared sensing.

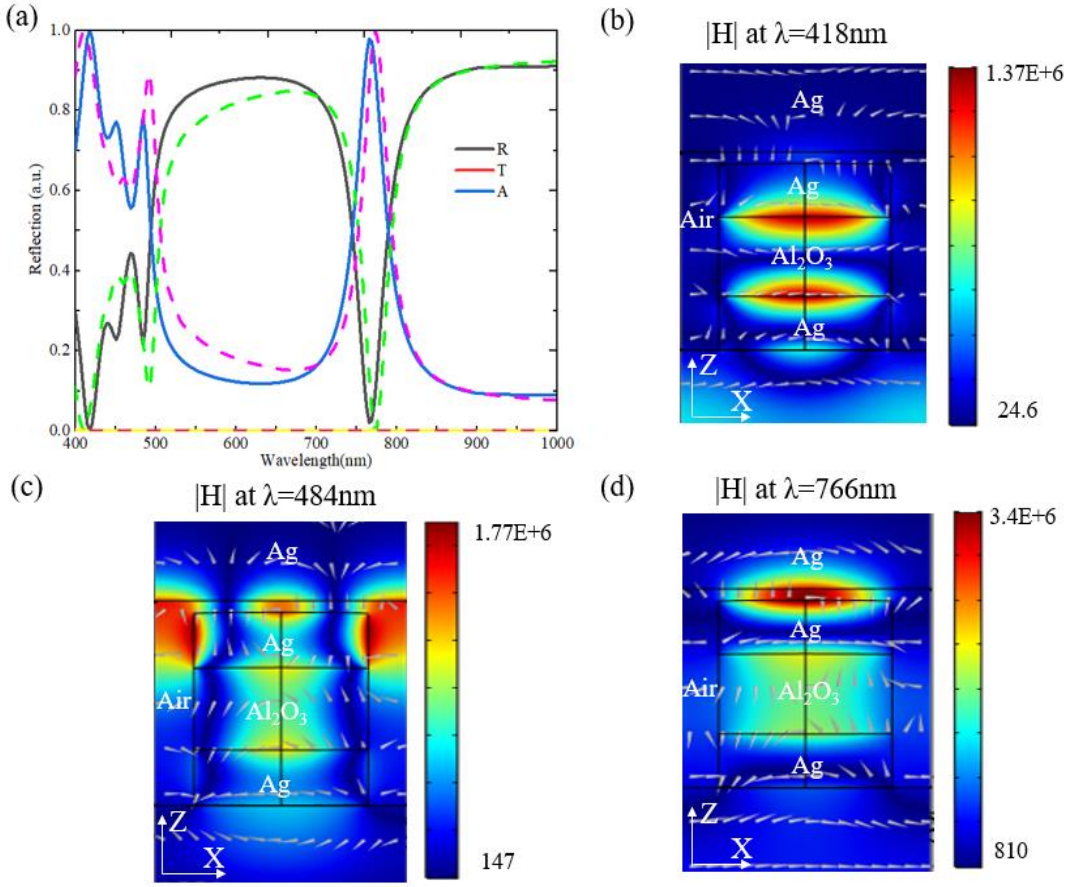

Figure 5.2 (a) Calculated absorbance (A, blue solid line & pink dashed line), reflectance (R, black solid line & green dashed line) and transmittance (T, red solid line & yellow dashed line) for 50nm/75nm/50nm MIM nanopillars (radius=70nm) with a periodicity of 200nm. The solid and dash line represent the result is attained through COMSOL and FDTD, respectively. The distance between the nanopillar array and the Ag film was set to 10nm. The magnetic field

distribution in the cross-section through the centre of the unite nanopillar parallel to the ZX-plane at the resonant wavelengths 418nm (b), 484nm(c) and 766nm(d), respectively. These grey arrows represent the electric vector.

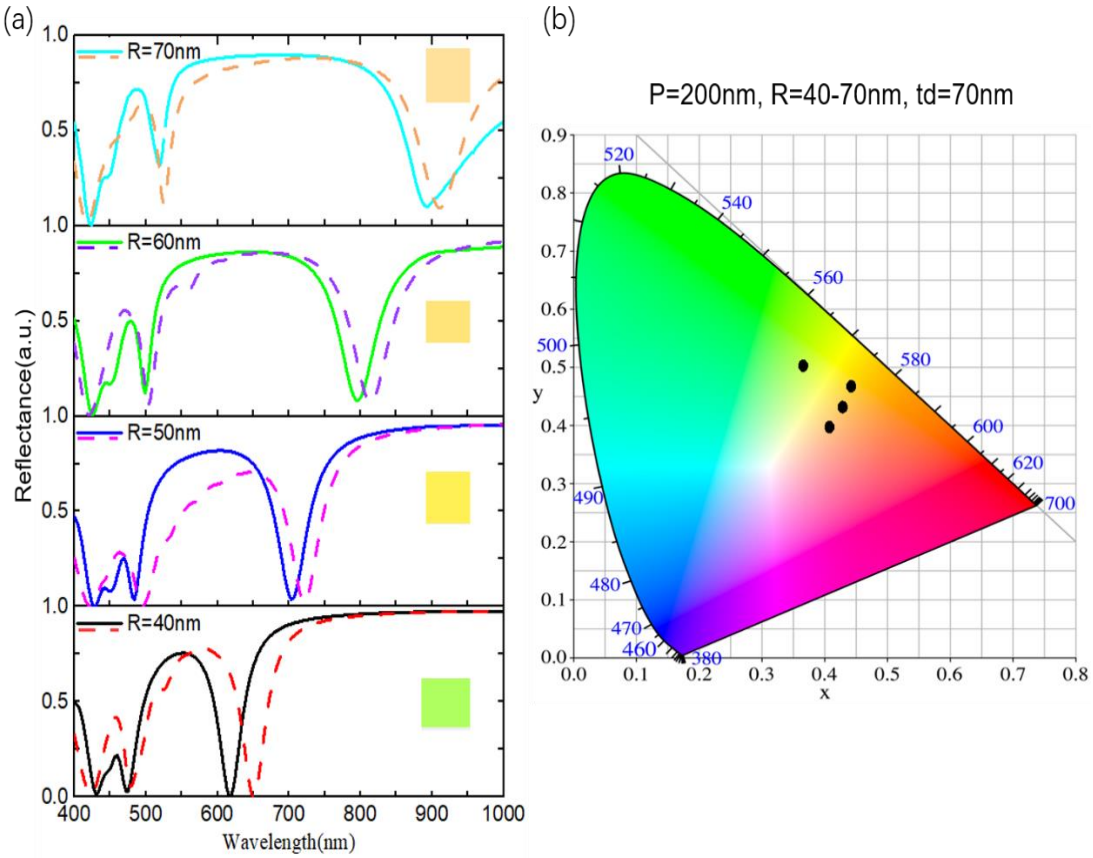

Figure 5.3 Simulated optical reflectance spectrum of the nanostructure vs. the radius of the MIM nanopillar (as specified in the legend) with fixed Al2O3 thickness of 70nm and period of 200nm. The solid and dash line represent the result is attained through COMSOL and FDTD, respectively. The distance between the nanopillar and the Ag film is 5nm. Insets: The mapped structure colours in the CIE 1931 chromaticity coordinate. (b) CIE 1931 chromaticity coordinates of calculated (solid black dots) optical reflectance spectra shown in panel (a).

According to theoretical calculations, the generated electromagnetic resonance within the nanostructure could be tuned through modifying the geometrical parameters, such as the radius of the nanopillar (R) and the thickness of the Al2O3 (td), resulting in the structure colour variation. To begin, a collection of the 50nm/70nm/50nm MIM

nanopillars with radius ranging from 40nm to 70nm is investigated, while the distance between the nanopillar array and the Ag film set at 5nm. The simulated optical reflectance spectra of the nanostructure with variable nanopillar radius (the COMSOL: solid lines and FDTD: dash lines) is presented in Figure 5.3a, as well as its colour loss as represented in the inset of each subfigure. As the radius of the cylinder increases, the second and third resonances redshift, however the first resonance remains constant at 418nm. According to the standard CIE 1931 chromaticity coordinates, these reflectance spectra could be converted to the CIE chromaticity space using a MATLAB method as illustrated in Figure 6.3b (solid black dots), effectively mapping the structure colours. As shown, the structure colour is sensitivity to the radius of the nanopillar arrays.

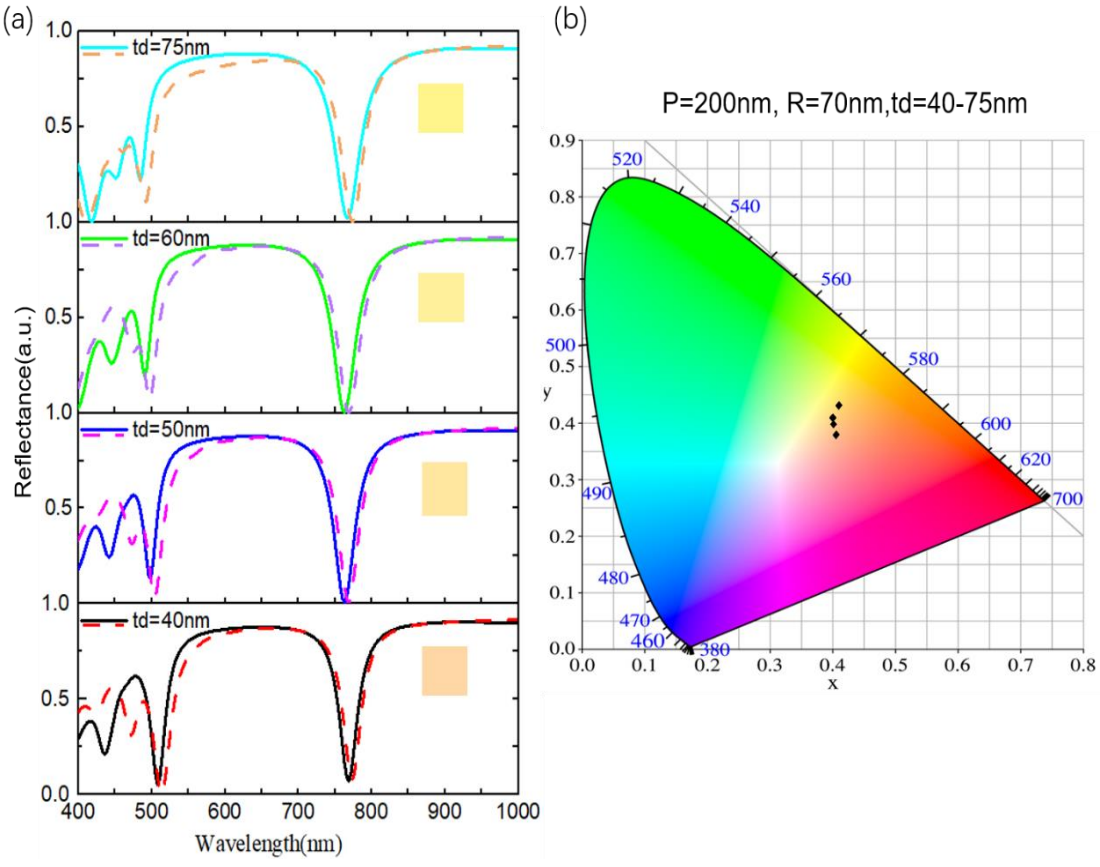

Figure 5.4 Simulated optical reflectance spectrum of the nanostructure vs. the thickness of the Al2O3 (as specified in the legend), with the radius of the nanopillar of 70nm and period of 200nm. The solid and dash line represent the result is attained through COMSOL and FDTD,

respectively. The distance between the nanopillar and the Ag film is 10nm. Insets: The appropriate structure colours in the CIE 1931 chromaticity coordinate. (b) CIE 1931 chromaticity coordinates of calculated (solid dark dots) optical reflectance spectra shown in panel (a).

In the next step, we looked at how the Al2O3 thickness impact on the reflectance spectrum of the nanostructure with a nanopillars radius of 70nm, a period of 200nm, and a gap between the nanopillar array and the Ag film of 10nm. Figure 5.4 describes the calculated optical reflectance spectrum of the nanostructure with the changeable Al2O3 thicknesses (the COMSOL: solid lines and FDTD: dash lines), along with its colour in the inset of each subfigure. Analysing the reflectance spectra in the graph reveals that the reflectance dip positions do not change significantly, with exception of the location of the second resonance mode, which exhibits a slight blue shift with the increasing Al2O3 thickness. The related CIE chromaticity coordinates (x, y), derived from the reflectance spectra through the MTALB tool, also do not alter drastically as shown in Figure 6.4b, and moreover the fluctuating of the mapped structure colours is unobvious. The explanation for this phenomenon is that the changing Al2O3 thickness has little effect on the gap plasmonic resonances (the second and third resonance modes) of the structure, which in turn adjusts the whole structure colours. However, its fluctuation affects the position and field distribution of the second resonance mode, as seen in Figure 6.2c the magnetic field is concentrated at the corner of the nanopillars and Ag-Al2O3 interface. Although the nanopillars are customized by changing Al2O3 thickness, the distance between the nanopillar arrays and the Ag film remains constant. Altering the Al2O3 thickness is equivalent to only changing the nanopillar. This spectral-insensitive Al2O3 thickness-tuning strategy enables the precise colour tuning. Therefore, as an alternative to the pursuit of spectral-sensitive wide gamut colours, the al2O3 thickness is able to be utilized as a spectral-insensitive geometrical parameter to

achieve precise colour adjustment, to improve the performance of this kind of sensor.

5.4 Force/Pressure Sensor

Figure 5.5a show a 2D schematic diagram of the nanostructure-plasmonic-based force/pressure sensor, which is made up of 50nm/75nm/50nm MIM nanopillar array with a periodicity of 200nm, covering by a metallic film. The radius of the MIM nanopillar is 70nm. The metal film is positioned above the MIM nanopillar with air gap d, which is ranging from 0nm to 15nm. To investigate the variation in the optical properties as a function of the air gap d, numerical simulations using two commercial softwares are carried out. The calculated optical reflectance spectrums of the nanostructure for various distances between the nanopillar array and the Ag film is included in Figure 5.5b, where the solid line represents the result from COMSOL and the dashed line indicates that of FDTD. The first resonance maintains a wavelength around 418nm as the air gap goes from 0nm to 15nm, whereas the second and third resonances exhibit apparent blue-shifting. The reflectance dip position of the second resonance mode occurs in the visible range (from 546nm to 445nm), while the third resonance mode is in near infrared spectral range (NIR). The appropriate structure colours are displayed in the illustration of each subfigure, and they are consistent with the colours in CIE 1931 chromaticity coordinate space, which correspond to the CIE chromaticity coordinates (x, y), obtained from the reflectance spectra using the MATALB tool, as shown in Figure 6.5c.

Because the change in force/pressure acting on the sensor is sensed as a modification in the resonance wavelength, the sensitivity of sensor is defined as the rate wherein the resonance wavelength adjustments to the force. Likewise, the sensor's sensitivity can be regarded of as rate of resonance wavelength alteration vs air gap thickness d. Therefore, the acting force/pressure can be evaluated via the calorimetric optical sensor,

and our gap-plasmonic-based nanostructure could be used as force/pressure sensors. And the structure colour alters from dark orange to yellow as the air gap became narrower, indicating the increasing force/pressure. As illustrated in Figure 5.6a, the relationship between the second resonance wavelength and the air gap is nearly linear, with a slope of approximately 6.8, whereas the relationship between the third resonance mode and the air gap is non-linear, and the relationship between the first resonance mode and the air gap is constant.

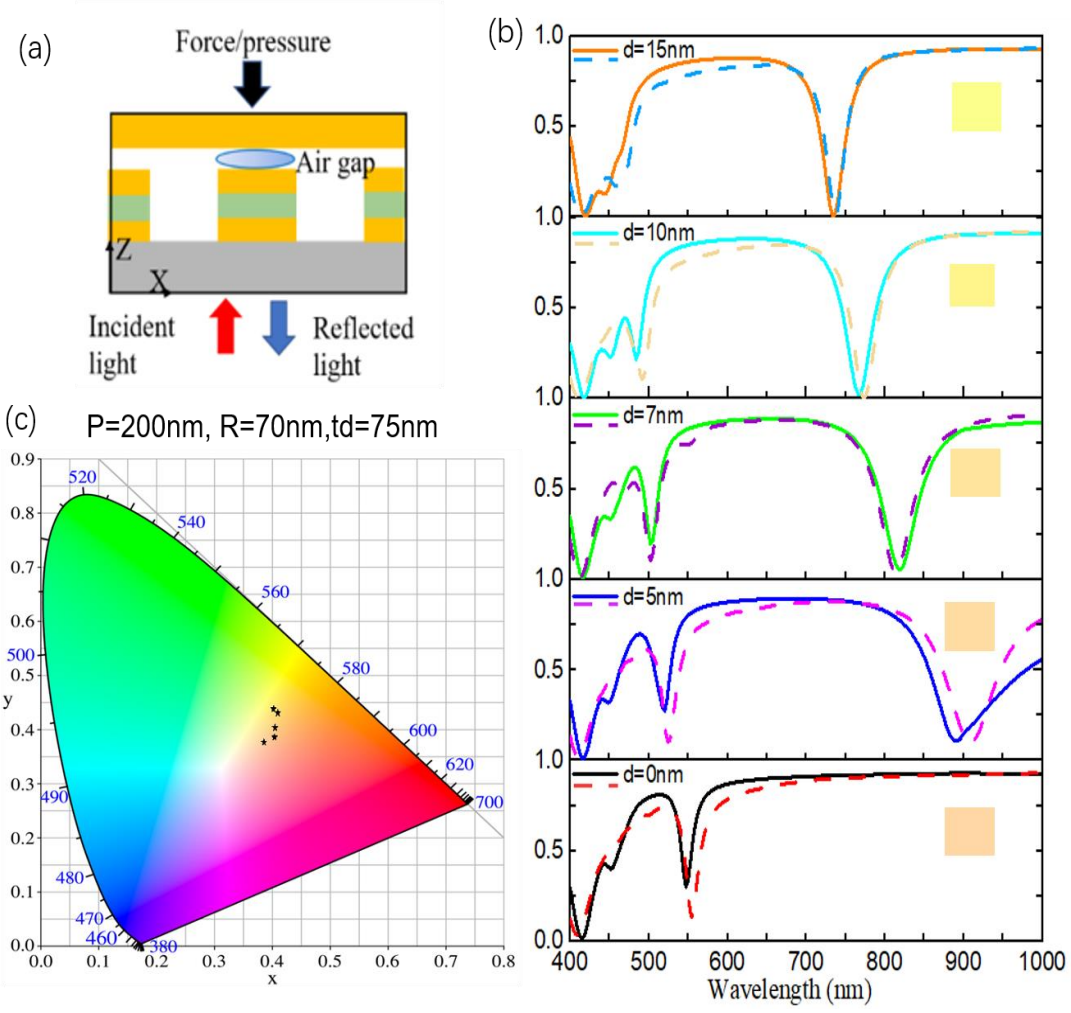

Figure 5.5 (a) The 2D diagram of one unit cell of the MIM nanopillar with the radius of the nanopillar of 70nm and period of 200nm, covered by a metallic film. The thickness of the Al2O3 is 75nm. (b) The calculated reflectance spectra when the thickness of the air gap d is 0, 5, 7, 10 or 15 nm. The solid and dash line represent the result is attained through COMSOL and FDTD, respectively. Insets: The appropriate structure colours in the CIE 1931 chromaticity

coordinate. (c) CIE 1931 chromaticity coordinates of calculated (solid dark dots) optical reflectance spectra shown in panel (b).

Meanwhile, Figure 6.6b highlights the quality factor (Q) for these three resonant modes, defined as Q=λ0/Δλ, where the λ0 is the resonance wavelength and Δλ is the full-with-half-maximum (FWHM). As presented in Figure 6.6b, the quality factor for the second mode (Q2) is always greater than the quality factor for the first and third modes (Q1, Q3), reaching a maximum value of 33 for d=0nm. The Q factor of the device at third resonance (Q3) diminishes as the air gap thickness decreases, although it is always lower than Q2. This is because the strong redshift of the third resonance associated with a smaller air gap d is accompanied by an increase in the FWHM in this case. As a conclusion, the proposed nanostructure, which has a relatively good quality factor at the second wavelength, could be exploited as a colorimetric optical sensor to detect the acting force/pressure.

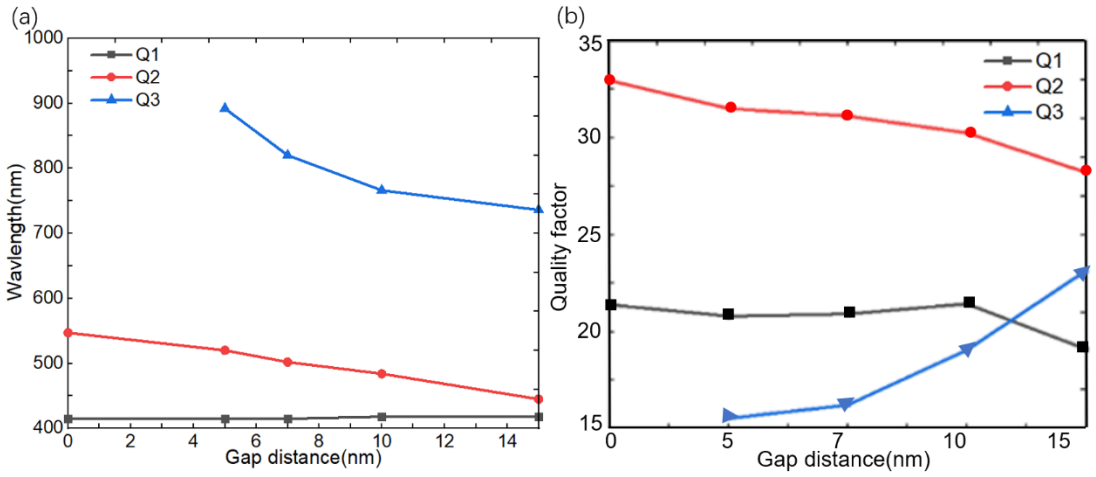

Figure 5.6 (a)The relationship between the three resonance wavelengths and the air gap thickness d. (b) Quality factor Q of these three resonance modes at various air gap thickness. The black, red and blue solid lines represent the quality factor of three resonant modes, respectively.

5.5 Refractive Index Sensor

On the other hand, the unique reflectance dip of the plasmonic-based nanostructures makes it possible to use as a refractive index (RI) sensor. In this work, our gap-plasmonic-based nanostructure may be utilized as a label-free sensor for testing the refractive index in a liquid environment, for example, the glycerin solution with different volume fractions of 10%, 20%, 30%, and 40% with refractive index ranging from 1.333 (water) to 1.389 (40% glycerin solution) [129]. As seen in Figure 5.7a, increasing the surrounding refractive index of the nanostructure, there is noticeable redshift in the reflectance spectra, with primary reflectance dip shifting from 444nm to 452nm. According to Figure 5.7b, the resonance wavelength and refractive index of the liquid environment have a linear relationship, with the slope of the fit line being around 141nm. As a result, the sensitivity of our nanostructure is around 141 nm/RIU, where the standard definition for the sensitivity of refractive index sensing is the spectral shifts (nm)/ refractive index changes. Besides, there is a slight resonant dip around 425 nm indicating a relative low sensitivity, which manifests different resonant modes cause two reflectance dips [144]. Furthermore, because the reflectance spectra shift of our nanostructure is in the visible regime, the structure colour will alter. Consequently, this device is suitable for calorimetric refractive index sensing, and is a good option for naked-eye calorimetric label-free biomedical sensing.

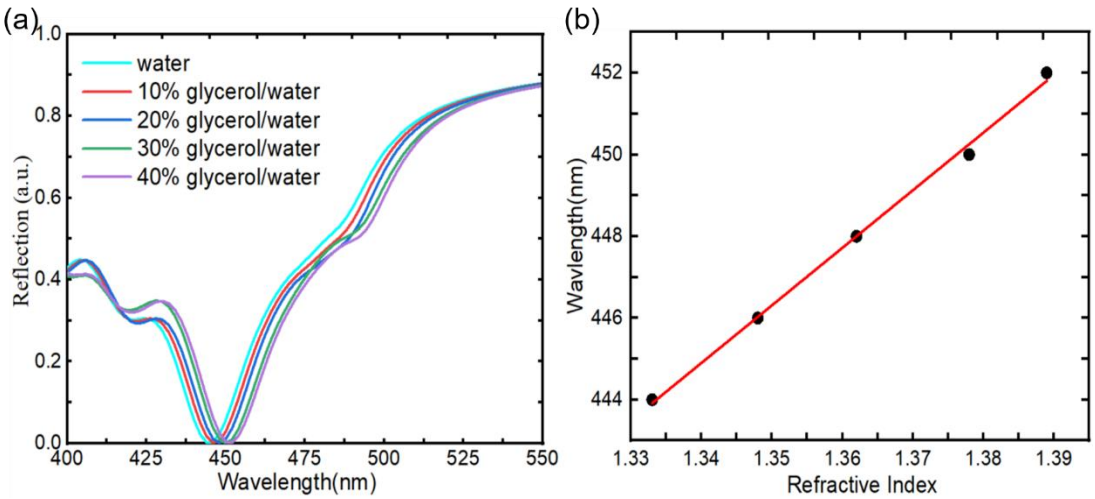

Figure 5.7 (a) The reflectance spectra of the structure with 50/70/50 nm MIM nanopillar, 70nm radius and 200nm period immersed in glycerin solution with the volume fraction of 10%, 20%, 30%, and 40%. The distance between the nanopillar and the Ag film is 0nm. (b) The linear fit curve on the reflectance dip position and the refractive index corresponding to (a).

5.6 Chapter Summary

In summary, we designed an optical sensor based on gap plasmon resonances of a MIM nanopillar array covered by the Ag film that allows highly sensitive detection of external factors that alter the gap distance d and which provides simple readout by its reflectance colour. The proposed device has several potential applications including biosensors, piezoelectric sensors. Concerning temperature sensing, not only changes in the distance d can be exploited, but also temperature induced changes of the refractive index of the gap medium.

Chapter 6: Summary and outlook

In this thesis, we have investigated the optical properties and resonance modes of multilayer MIM nanostructures based on plasmonics, such as MIM nanopillars and MIM structures with lateral or vertical gratings. Our calculations show that MIM systems with vertical or lateral gratings can produce multiple resonances as well as ENZ bands that can be tuned in the visible range by adjusting the geometry parameters. They both contribute to the Purcell enhancement of the spontaneous emission of the fluorophore located on top of the system, due to the large local photonic density of the state at low-energy ENZ resonance. The distinction is that the MIM system with lateral grating generates multiple uncoupled ENZ resonances, whereas the vertical grating MIM structure provides strongly coupled ENZ bands. Furthermore, the applications of the plasmonic MIM-based nanostructures are mainly explored in the field of the PeLED device and the optical sensor in this work. Under the assumption of the effective photon generation in the emitter layer, the effects of the emitter orientation and the functional layer thicknesses on the overall performance of the planar PeLEDs are explored to design specifical flat LED structures, and then we investigated how the MIM-based interface modification affects the performance of the patterned PeLED. Our calculation results demonstrated that specific planar PeLED structures could be designed through systematic analysis, which helps reduce the experimental cost, and that the MIM-based interface modification can improve the Purcell factor and outcoupling efficiency of the patterned PeLED device, thereby enhancing its EQE compared with the nanopattern-free PeLED. Moreover, our research found that the GPR-based optical sensor, composed of MIM nanopillars, can detect the change in the ambient pressure/ temperature/refractive-index according to the micro-variation of the structure colour, because of the variation in the reflection spectrum peak.

Looking to the future, the multilayer metal-insulator metamaterial offers a wide range

of potential applications in optoelectronic devices. As previously stated in this work, MIM nanocavities with lateral or vertical gratings boost the spontaneous emission of fluorescence. For example, the uncoupled resonances of the lateral grating MIM structure can be used to enhance the emission of two fluorophores in the same solution simultaneously, while the strongly coupled resonant mode of the vertical MIM grating can be utilized to design photodetectors, biosensors, and lasers. However, all of these conclusions are based on numerical analysis. In the future, if these numerical calculation approaches are combined with experiments to improve the overall performance of LEDs or solar cells by a study of the physical mechanism, it will be extremely significant and valuable. Furthermore, photodetector devices will also be promising research fields for the MIM-based nanostructure since the response intensity and time of the photodetector could be improved by tailoring the MIM structure. With regards to the light sensor, our calculations show that the range of colour variation triggered by changes in the gap distance is rather minimal. Thus, it is essential to look for materials or methods to increase the colour variation range of the device, which can be read by the naked eye.

Reference

1. Dang, C., Lee, J., Breen, C., Steckel, J. S., Coe-Sullivan, S., Nurmikko, A. Red, Green and Blue Lasing Enabled by Single-Exciton Gain in Colloidal Quantum Dot Films. *Nat. Nanotechnol.* **2012**, *7*, 335−339.

2. Coropceanu, I., Rossinelli, A., Caram, J. R., Freyria, F. S., Bawendi, M. G. Slow-Injection Growth of Seeded CdSe/CdS Nanorods with Unity Fluorescence Quantum Yield and Complete Shell to Core Energy Transfer. *ACS Nano.* **2016**, *10*, 3295–3301.

3. Moon, A., Kim, J. Hybrid QuantumDot Light-Emitting Diodes for White Emission Using Blue Phosphorescent Organic Molecules and Red Quantum Dots. *Micromachines.* **2019**, *10*, 609.

4. Chen, O., Zhao, J., Chauhan, V. P.,Cui, J., Wong, C., Harris, D. K., et. al. Compact High-Quality CdSe−CdS Core−shell Nanocrystals with Narrow Emission Linewidths and Suppressed Blinking. *Nat. Mater.* **2013**, *12*, 445−451.

5. Kim, T.-H., Cho, K.-S., Lee, E. K., Lee, S. J., Chae, J., Kim, J. W., Kim, D. H., et. al. Full-Colour Quantum Dot Displays Fabricated by Transfer Printing. *Nat. Photonics* **2011**, *5*, 176−182.

6. Kim, L., Anikeeva, P. O., Coe-Sullivan, S. A., Steckel, J. S., Bawendi, M. G., Bulović, V. Contact Printing of Quantum Dot Light-Emitting Devices. *Nano Lett.* **2008**, *8*, 4513−4517.

7. Kwak, J., Lim, J., Park, M., Lee, S., Char, K., Lee, C. High-PowerGenuine Ultraviolet Light-Emitting Diodes Based on Colloidal Nanocrystal Quantum Dots. *Nano Lett.* **2015**, *15*, 3793−3799.

8. Shirasaki, Y., Supran, G.J., Bawendi, M.G., Bulovic, V. Emergence of colloidal quantum-dot light-emitting technologies. *Nat. Photonics* **2013**, *7*, 13–23.

9. Moon, A., Kim, J. Hybrid QuantumDot Light-Emitting Diodes for White Emission Using Blue Phosphorescent Organic Molecules and Red Quantum Dots. *Micromachines* **2019**, *10*, 609.

10. Fan, F., Voznyy, O., Sabatini, R. P., Bicanic, K. T., Adachi, M. M., et. al. Continuous-wave lasing in colloidal quantum dot solids enabled by facet-selective epitaxy. *Nature* **2017**, *544*, **7**5.

11. Sargent, E. H., Colloidal quantum dot solar cells. *Nat. Photonics* **2012**, *6*, 133

12. Meinardi, F., McDaniel, H., Carulli, F., Colombo, A., Velizhanin, K. A., et. al. Highly Efficient Large-Area Colourless Luminescent Solar Concentrators Using Heavy-Metal-Free Colloidal Quantum Dots. *Nat. Nanotechnol.* **2015**, *10,* 878−885.

13. Oertel, D.C., Bawendi, M.G. Photodetectors based on treated CdSe quantum-dot films. Appl. *Phys. Lett.* **2005,** *87*, 213505.

14. Lhuillier, E., Scarafagio, M., Hease, P., Nadal, B., Aubin, H., Xu, et. al. Photodetection Based on Colloidal Quantum-Dot Films with High Mobility and Optical Absorption up to THz. *Nano Lett.* **2016**, *16*, 1282−1286.

15. Gil-Escrig, L., Longo, G., Pertegás, A., Roldán-Carmona, C., Soriano, A., Sessolo, M., Bolink, H.J. Efficient photovoltaic and electroluminescent perovskite devices. *Chem. Commun.* **2015**, *51*, 569–571.

16. McDonald, S. A., Konstantatos, G., Zhang, S., Cyr, P. W., et. al. Solution-Processed PbS Quantum Dot Infrared Photodetectors and Photovoltaics. *Nat. Mater.* **2005**, *4*, 138−142.

17. Zito, J. and Infante, I. The Future of Ligand Engineering in Colloidal Semiconductor Nanocrystals. *Accounts of Chemical Research* **2021**, *54* (7), 1555-1564.

18. Razgoniaeva, N., Yang, M., Garrett, P., et. al. Just Add Ligands: Self-Sustained Size Focusing of Colloidal Semiconductor Nanocrystals. *Chemistry of Materials* **2018**. *30* (4), 1391-1398.

19. Ievgen Levchuk, Andres Osvet, Xiaofeng Tang, et.al. Brightly Luminescent and Color-Tunable Formamidinium Lead Halide Perovskite FAPbX3 (X=Cl, Br, I) Colloidal Nanocrystals. *NanoLetters* **2017**, *17*(5), 2765–2770.

20. Hamm, L., Gee, A., De Silva Indrasekara, A.S. Recent Advancement in the Surface-Enhanced Raman Spectroscopy-Based Biosensors for Infectious Disease Diagnosis. *Appl. Sci.* **2019**, *9*, 1448.

21. Jarvis, M. R.and Goodacre, R., Discrimination of Bacteria Using Surface-Enhanced Raman Spectroscopy. *Analytical Chemistry* **2004**, *76*, 40-47.

22. Huang, X., El-Sayed, M. A., Plasmonic photo-thermal therapy (PPTT). *Alexandria Journal of Medicine.* **2011**, 47, 1-9.

23. Hiep, H. M., Endo, T., Kerman, K., Chikae, M., et. Al, A localized surface plasmon resonance based immunosensor for the detection of casein in milk. *Science and Technology of Advanced Materials* **2007**, *8*, 331-338.

24. Debasu, M.L., Ananias, D., Pastoriza-Santos, I., Liz-Marzán, L.M., Rocha, J. and Carlos, L.D., All-In-One Optical Heater-Thermometer Nanoplatform Operative From 300 to 2000 K Based on Er3+ Emission and Blackbody Radiation. *Adv. Mater.*, **2013**, *25*, 4868-4874.

25. Das, G., Coluccio, M. L., Alrasheed, S., Giugni, A., et. al., Plasmonic nanostructures for the ultrasensitive detection of biomolecules. *Rivista Del Nuovo Cimento*. **2016**, *39*, 547-586.

26. Zafar, R., Investigation of Optical Buffering and Refractive Index Sensing characteristcis in Fano resonance-based metal-insulator-metal Plasmonic waveguide. *India*, **2016**

27. Campione, S., Brener, I., Marquier, F., Theory of epsilon-near-zero modes in ultrathin films. *Phys. Rev. B* **2015**, *91*, 121408.

28. Caligiuri, V., et al. Hybridization of epsilon-near-zero modes via resonant tunneling in layered metal-insulator double nanocavities. *Nanophotonics* **2019**, *8*, 1505-1512.

29. Drude, P. *The Theory of Optics*. **1902**

30. Irene, Eugene A., Applications of spectroscopic ellipsometry to microelectronics. *Thin Solid Films* **1993**, *233*, 96-111.

31. Li, K.,Wang, S., Wang, L., Yu, H., Jing, N., Xue, R., Wang, Z., Fast and Sensitive Ellipsometry-Based Biosensing. *Sensors* **2018**, *18*, 15.

32. Wolf, S. D., Holovsky, J., Moon, S.-J., Löper, P., Niesen, B.,et. Al., Organometallic Halide Perovskites: Sharp Optical Absorption Edge and Its Relation to Photovoltaic Performance. *The Journal of Physical Chemistry Letters* **2014**, *5*, 1035-1039.

33. https://www.jawoollam.com

34. https://en.wikipedia.org/wiki/Ellipsometry

35. Dorywalski, K., Maciejewski, I. And Krzyżyński, T., Spectroscopic ellipsometry technique as a materials characterization tool for mechatronic systems—The case of composition and doping concentration monitoring in SBN crystals, *Mechatronics* **2016**, *37*, 33-41.

36. https://en.wikipedia.org/wiki/Fluorescence

37. Lee, J.W., *Bioluminescence.* **2017**.

38. Glazov, M. M., Ivchenko, E.L., Poddubny, A.N. et al. Purcell factor in small metallic cavities. *Phys. Solid State* **2011**, *53*, 1753.

39. Rogobete, L., Kaminski, F., Agio, M. and Sandoghdar, V. Design of plasmonic nanoantennae for enhancing spontaneous emission. *Opt. Lett.* **2007**, *32*, 1623-1625.

40. Morozov, K.M., Ivanov, K.A., de Sa Pereira, D. et al. Revising of the Purcell effect in periodic metal-dielectric structures: the role of absorption. *Sci. Rep.* **2019**, *9*, 9604.

41. Renaud A. L. Vallée, Ferrié, M., Saadaoui, H., and Ravaine, S. Broadband spontaneous emission rate enhancement through the design of plasmonic nanoantennas. *Opt. Mater. Express* **2012**, *2*, 566-577.

42. Choy, J.T., Bulu, I., Hausmann, Birgit J. M., Janitz, E., et. al., Spontaneous emission and collection efficiency enhancement of single emitters in diamond via plasmonic cavities and gratings. *Appl. Phys. Lett.* **2013**, *103*, 161101

43. Nikitin, A. Y., Guinea, F., Garcia-Vidal, F. J., Martin-Moreno, L. Surface Plasmon Enhanced

Absorption and Suppressed Transmissionin Periodic Arrays of Graphene Ribbons. *Phys. Rev. B.* **2012,** *85*, 081405.

44. Gryczynski, I., Malicka, J.,Jiang, W., Fischer, H., at.al., Surface-Plasmon-Coupled Emission of Quantum Dots. *The Journal of Physical Chemistry B* **2005**, *109*, 1088-1093.

45. Ford, G.W. & Weber, W. H. Electromagnetic interactions of molecules with metal surfaces. *Physics Reports* **1984**, *113*, 195-287.

46. Barnes, W. L. Fluorescence near interfaces: the role of photonic mode density. *Journal of Modern Optics* **1998**, *45*, 661-699.

47. Lu, D., Kan, J., Fullerton, E.E. & Liu, Z. Tunable surface plasmon polaritons in Ag composite films by adding dielectrics or semiconductors. *Appl. Phys. Lett.* **2011**, *98*, 243114.

48. Troparevsky, M. C., Sabau, A. S., Lupini, A. R. and Zhang, Z., Transfer-matrix formalism for the calculation of optical response in multilayer systems: from coherent to incoherent interference. *Opt. Express* **2010**, *18*, 24715-24721.

49. Ford, G. W.; Weber, W. H. Electromagnetic interactions of molecules with metal surfaces. *Phys. Rep.* **1984**, *113*, 195−287.

50. Newman, W. D., Cortes, C. L., Jacob, Z. Enhanced and directional single-photon emission in hyperbolic metamaterials. *J. Opt. Soc. Am. B* **2013**, *30*, 766−775.

51. Wylie, J. M., Sipe, J. E. Quantum electrodynamics near an interface. II. *Phys. Rev. A* **1985**, *32*, 2030.

52. https://www.comsol.it

53. Zhao, C., Zhang, D. And Qin, C. Perovskite Light-Emitting Diodes. *CCS Chem.* **2020**, *2*, 859–869.

54. Shin, H., Lee, J.-H., Moon, C.-K., Huh, J.-S., Sim, B. and Kim, J.-J. Sky-Blue Phosphorescent OLEDs with 34.1% External Quantum Efficiency Using a Low Refractive Index Electron Transporting Layer. *Adv. Mater.* **2016**, *28*, 4920-4925.

55. W. L. Barnes, Fluorescence near interfaces: the role of photonic mode density. *J. Mod Opt.* **1998**, *45*, 661–699.

56. Chance, R. R., Prock, A. and Silbey, R. Lifetime of an emitting molecule near a partially reflecting surface. *J. Chem. Phys.*, **1974**, *60*, 2744–2748.

57. Prigogine, I. and Rice, S. A. *Advances in Chemical Physics,* **2009**, *37*.

58. Furno, M., Meerheim, R., Hofmann, S., Lussem, B. and Leo, K. Efficiency and rate of spontaneous emission in organic electroluminescent devices. *Physical Review B* **2012**, *85*(11), 115205

59. Gather, M. C. & Reineke, S. Recent advances in light outcoupling from white organic light-emitting diodes. *Journal of Photonics for Energy* **2015**, *5* (1), 057607.

60. Kim, K., Moon, C., Lee, J., Kim, S. Highly Efficient Organic Light-Emitting Diodes with Phosphorescent Emitters Having High Quantum Yield and Horizontal Orientation of Transition Dipole Moments. *Adv. Mater.* **2014**, *26*(23), 3844-7.

61. Frischeisen, J., Yokoyama, D., Endo, A., Adachi, C. and Brütting,W. Increased light outcoupling efficiency in dye-doped small molecule organic light-emitting diodes with horizontally oriented emitters. *Org. Electron.*, **2011**, *12*(5), 809–817.

62. Cho, H., Chung, J.,Song, J., Lee, J., et. Al. Importance of Purcell factor for optimizing structure of organic light-emitting diodes. *Opt. Express* **2019**, *27*, 11057-11068.

63. Tenopala-Carmona, F., Lee, O. S., Crovini, E., Neferu, A. M., Murawski, C., et. al., Identification of the Key Parameters for Horizontal Transition Dipole Orientation in Fluorescent and TADF Organic Light-Emitting Diodes. *Adv. Mater.* **2021**, *33*, 2100677.

64. Jeantet, A., Chassagneux, Y., Raynaud, C., Roussignol, P., Lauret, J. S., Besga, B., Estève, J., Reichel, J., Voisin, C. Widely Tunable Single-Photon Source from a Carbon Nanotube in the Purcell Regime. *Phys. Rev. Lett.* **2016**, *116*, 247402

65. Somaschi, N., Giesz, V., De Santis, L., Loredo, J. C., Almeida, M. P., Hornecker, G., Portalupi, S. L., Grange, T., Antón, C., Demory, J. Near-Optimal Single-Photon Sources in the Solid State. *Nat. Photonics* **2016**, *10*, 340– 345,

66. Rosi N. L. And Mirkin C. A. Nanostructures in biodiagnostics. *Chem. Rev.* **2005**, *105*, 1547-62.

67. Roth, D. J., Krasavin, A. V., Wade, A., et. al. Spontaneous Emission inside a Hyperbolic Metamaterial Waveguide. *ACS Photonics* **2017**, *4*, 2513-2521.

68. Zhou, W., Dridi, M., Suh, J. Y., Kim, C. H.; Co, D. T., Wasielewski, M. R.; Schatz, G. C.; Odom, T. W. Lasing Action in Strongly Coupled Plasmonic Nanocavity Arrays. *Nat. Nanotechnol.* **2013**, *8*, 506– 511

69. Noginov, M.; Zhu, G.; Belgrave, A.; Bakker, R.Demonstration of a Spaser-Based Nanolaser. *Nature* **2009**, *460*, 1110– 1112

70. Zhang, Q., Li, G., Liu, X., Qian, F., Li, Y., Sum, T. C., Lieber, C. M., Xiong, Q. A Room Temperature Low-Threshold Ultraviolet Plasmonic Nanolaser. *Nat. Commun.* **2014**, *5*, 4953– 4962,

71. Wu, S., Buckley, S., Schaibley, J. et al. Monolayer semiconductor nanocavity lasers with ultralow thresholds. Nature **2015**, 520, 69–72.

72. Gerard, J. -M. and Gayral, B. Strong Purcell effect for InAs quantum boxes in three-

dimensional solid-state microcavities. IEEE Journal of Lightwave Technology **1999**, 17(11), 2089-2095.

73. Reshef, O., De Leon, I., Alam, M.Z. et al. Nonlinear optical effects in epsilon-near-zero media. *Nat. Rev. Mater.* **2019**, *4*, 535–551.

74. Maas, R., Parsons, J., Engheta, N. et al. Experimental realization of an epsilon-near-zero metamaterial at visible wavelengths. *Nature Photon* 2**013**, *7*, 907–912.

75. Caligiuri, V., Palei, M., Biffi, G., Artyukhin, S. and Krahne, R. A Semi-Classical View on Epsilon-Near-Zero Resonant Tunneling Modes in Metal/Insulator/Metal Nanocavities. *Nano Letters* **2019**, *19*, 3151-3160.

76. Caligiuri, V., Palei, M., Biffi, G.and Krahne, R. Hybridization of epsilon-near-zero modes via resonant tunneling in layered metal-insulator double nanocavities. *Nanophotonics* **2019**, *8*,1505-1512.

77. Caligiuri, V., Palei, M.,Imran, M., Manna, L. and Krahne, R. Planar Double-Epsilon-Near-Zero Cavities for Spontaneous Emission and Purcell Effect Enhancement. *ACS Photonics* **2018**, *5*, 2287-2294

78. Kang, S.W., Baek, D. H., Ju, B. K., et. al. Green phosphorescent organic light-emitting diode exhibiting highest external quantum efficiency with ultra-thin undoped emission layer. *Sci. Rep.* **2021**, *11*, 8436.

79. Won, Y. H., Cha, O., Kim, T., et al. Highly efficient and stable InP/ZnSe/ZnS quantum dot light-emitting diodes. *Nature* **2019**, *575*, 634-638.

80. Kar, S., Jamaludin, N. F., Yantara, N., et al. Recent advancements and perspectives on light management and high performance in perovskite light-emitting diodes. *Nanophotonics* **2020**, *10*, 2103-2143.

81. Karlsson, M., Yi, Z., Reichert, S., et al. Mixed halide perovskites for spectrally stable and high-efficiency blue light-emitting diodes. *Nat. Commun.* **2021**,*12*, 361.

82. Park, M. H., Kim, J. S., Heo, J. M., et al. Boosting Efficiency in Polycrystalline Metal Halide Perovskite Light-Emitting Diodes. *ACS Energy Lett.* **2019**,*4*, 1134-1149.

83. Kim, Y. H., Kim, S., Kakekhani, A., et al. Comprehensive defect suppression in perovskite nanocrystals for high-efficiency light-emitting diodes. *Nat. Photonics* **2021**, *15*, 148–155.

84. Kumawat, N. K., Liu, X. K., Kabra, D., et al. Blue perovskite light-emitting diodes: progress, challenges and future directions. *Nanoscale* **2019**, *11*(5), 2109-2120.

85. Shen, Y., Cheng, L. P., Li, Y. Q., et al. High-Efficiency Perovskite Light-Emitting Diodes with Synergetic Outcoupling Enhancement. *Adv. Mater.* **2019**,*31*, 1901517.

86. Park, C.H., Kang, S.W., Jung, SG. et al. Enhanced light extraction efficiency and viewing angle characteristics of microcavity OLEDs by using a diffusion layer. *Sci. Rep.* **2021**,*11*, 3430.

87. Xu, B., Wang, W., Zhang, X. et al. Electric Bias Induced Degradation in Organic-Inorganic Hybrid Perovskite Light-Emitting Diodes. *Sci. Rep.* **2018**,*8*, 15799.

88. Meng, S.S., Li, Y. Q. & Tang, J. X. Theoretical perspective to light outcoupling and management in perovskite light-emitting diodes. *Organic Electronics* **2019**,*61*, 351-358.

89. Shi, X. B., Liu, Y., Yuan, Z., et al. Optical Energy Losses in Organic–Inorganic Hybrid Perovskite Light-Emitting Diodes. *Adv. Optical Matter.* **2018**,*6*, 1800667..

90. Mac Ciarnain, R., Michaelis, D., Wehlus, T. et al. Plasmonic Purcell effect reveals obliquely ordered phosphorescent emitters in Organic LEDs. *Sci. Rep.* **2017**,*7*, 1826.

91. Zou, C. & Lin, L. Effect of emitter orientation on the outcoupling efficiency of perovskite light-emitting diodes. *Opt. Lett.* **2020**, *45*, 4786-4789.

92. Zhu, R., Luo, Z. & Wu, S. Light extraction analysis and enhancement in a quantum dot light emitting diode. *Opt. Express* **2014**, *22*, A1783-A1798.

93. Abdi-Jalebi, M., Andaji-Garmaroudi, Z., Cacovich, S., et al. Maximizing and stabilizing luminescence from halide perovskites with potassium passivation. *Nature* **2018**, *555*, 497–501.

94. Liang, H., Zhu R., Dong Y., et al., Enhancing the outcoupling efficiency of quantum dot LEDs with internal nanoscattering pattern. *Opt. Express* **2015**, *23*, 12910-12922.

95. Braly, I. L., deQuilettes, D. W., Pazos-Outón, L. M., et al. Hybrid perovskite films approaching the radiative limit with over 90% photoluminescence quantum efficiency. *Nat. Photonics* **2018**, 12, 355-361.

96. Yan, W., Mao, L., Zhao, P., et al. Determination of complex optical constants and photovoltaic device design of all-inorganic CsPbBr3 perovskite thin films. *Opt. Express* **2020**, *28*, 15706-15717.

97. Aguilar, O., de Castro, S., Godoy, M. & Rebello Sousa Dias M. Optoelectronic characterization of Zn1-xCdxO thin films as an alternative to photonic crystals in organic solar cells. *Opt. Mater. Express* **2019**, *9*, 3638-3648.

98. Senes, A., Meskers, S. C. J., Dijkstra, W. M., et al. Transition dipole moment orientation in films of solution processed fluorescent oligomers: investigating the influence of molecular anisotropy. *J. Mater. Chem. C.* **2016**, *4*, 6302-6308.

99. Moerland, R. & Hoogenboom, J. Subnanometer-accuracy optical distance ruler based on fluorescence quenching by transparent conductors. *Optica* **2016**, *3*, 112-117.

100. Rakić, A. D., Djurišic, A. B., Elazar, J. M. & Majewski, M. L. Optical Properties of Metallic Films for Vertical-Cavity Optoelectronic Devices. *Appl. Opt.* **1998**, *37,* 5271/

101. Raja, W., Bozzola, A., Zilio, P., et al. Broadband absorption enhancement in plasmonic nanoshells-based ultrathin microcrystalline-Si solar cells. *Sci. Rep.* **2016**, *6*, 1-11/

102. Alabastri, A., Toma, A., Malerba, M., De Angelis F. & Proietti Zaccaria R. High temperature nanoplasmonics: the key role of nonlinear effects. *ACS Photonics* **2015**, *2*, 115-120.

103. van Mensfoort S. L. M., Carvelli, M., Megens, M., et al. Measuring the light emission profile in organic light-emitting diodes with nanometre spatial resolution. *Nat. Photonics* **2010**, *4*, 329-335.

104. Castelli, A., Meinardi, F., Pasini, M., et al. High-Efficiency All-Solution-Processed Light-Emitting Diodes Based on Anisotropic Colloidal Heterostructures with Polar Polymer Injecting Layers. *Nano Lett.* **2015**, *15*, 5455–5464.

105. Rastogi, P., Palazon, F., Prato, M., et al. Enhancing the Performance of CdSe/CdS Dot-in-Rod Light-Emitting Diodes via Surface Ligand Modification. *ACS Appl. Mater. Interface* **2018**, *10*, 5665-5672.

106. Lin, K., Xing, J., Li N. Perovskite light-emitting diodes with external quantum efficiency exceeding 20 percent. *Nature Letter* **2018**, *562*, 245-248.

107. Cao, Y., Wang, N., Tian, H., et al., Perovskite light-emitting diodes based on spontaneously formed submicrometre-scale structures. *Nature* **2018**, *562*, 249-353.

108. Liu, M., Jiang, N., Wang, Z., Zheng, Y., Hong, J., Du, S. and Chen, D., Mn2+-Doped CsPbI3 Nanocrystals for Perovskite Light-Emitting Diodes with High Luminance and Improved Device Stability. *Adv. Photonics Res.* **2021**, 2100137

109. Tan, Z. K., Moghaddam, R. S., Lai, M. L., et al., Bright light-emitting diodes based on organometal halide perovskite. *Nat. Nanotechnol.* **2014**, *9*, 687-92.

110. Zhao, L., Lee, K. M., Roh, K., et al., Improved Outcoupling Efficiency and Stability of Perovskite Light-Emitting Diodes using Thin Emitting Layers. *Adv. Mater.* **2019**, *31*, 1805836.

111. Laxmi, and Kabra, D., Optimization of Composition with Reduced Phase Impurity in Quasi-2D Perovskite for Electroluminescence. *Adv. Photonics Res.* **2021**, *2*, 2000164.

112. Liu, M., Grandhi, G. K., Matta, S., et al., Halide Perovskite Nanocrystal Emitters. *Adv. Photonics Res.* **2021**, 2, 2000118

113. J. Lin, Sun, Q., Feng, W., Guo, S., Liu, Z., Liang, H. and Li, J. Enhancing the Light Extraction Efficiency in Micro-Organic Light-Emitting Diodes with Metalens. Adv. *Photonics Res.*, **2021**, *2*, 2000145.

114. Park, J. H., Chu, W. S., Oh, M. C., et al., Outcoupling Efficiency Analysis of OLEDs Fabricated on a Wrinkled Substrate. *Journal of Display Technology* **2016**,*12*, 801.

115. Yue, Q., Li, W., Kong, F., Li, F., Enhancing the Out-Coupling Efficiency of Organic Light-Emitting Diodes Using Two-Dimensional Periodic Nanostructures. Advances in Materials Science and Engineering, **2012**, *2012*, 1.

116. Yang, J. P., Bao, Q. Y., Xu, Z. Q., et al., Light out-coupling enhancement of organic light-emitting devices with microlens array. *Appl. Phys. Lett.* **2010**, *97*, 223303.

117. Beliaev, L. Y., Takayama, O., et al., Photoluminescence control by hyperbolic metamaterials and metasurfaces: a review. *Opto-Electron Adv.* **2021**, *4*, 210031.

118. Iorsh, I., Poddubny, A., et al., Hyperbolic transmission-line metamaterials. *Phy. Lett. A,* **2012**, *376*,185.

119. Smalley, J., Vallini, F., Montoya, S. et al., Luminescent hyperbolic metasurfaces. *Nat Commun.*, **2017**, *8*, 13793.

120. Jung, Y. J., Cho, S.Y., Jung, J. W., Kim, S. Y. and Lee, J. H., Influence of indium-tin-oxide and emitting-layer thicknesses on light outcoupling of perovskite light-emitting diodes. *Nano. Converg.* **2019**, 6(1): 26.

121. Wang, S., Li, C., Xiang, Y., Qi, H., et. al., Light extraction from quantum dot light emitting diodes by multiscale nanostructures. *Nanoscale Adv.*, **2020**, *2*, 1967-1972

122. Zhang, Q., Gu, X., Chen, Z., Jiang, J., et. al., Enhancing extraction efficiency of quantum dot light-emitting diodes by surface engineering. *Opt. Express,* **2017**, *25*, 17683-17694.

123. Butt, M.A., Khonina, S.N., Kazanskiy, N.L. Plasmonics: A necessity in the field of sensing—A review (invited). *Fiber Integr. Opt.* **2021**, *40*, 14–47.

124. Sakai, H., Okahisa, S., Nakayama, Y.,Nakayama, K.,Fukuhara, M., Kimura, Y., Ishii, Y., Fukuda, M. Plasmonic and electronic device-based integrated circuits and their characteristics. *Solid State Electron.* **2016**, *125*, 240–246.

125. Mahmood, A. I., Kadhim, S. A., Mohammed, N. F., & Naseef, I. A. Simulation design of silver nanoparticle coated photonic crystal fiber sensor based on surface plasmon resonance. *Exp. Theo. NANOTECHNOLOGY.* **2021**, *5*, 57-64.

126. Rifat, A. A.,Ahmed, R.,Yetisen, A. K., Butt, H.,Sabouri, A.,Mahdiraji, G. A., et al., Photonic crystal fiber based plasmonic sensors. *Sensors and Actuators B: Chemical.* **2017**, *243*, 311-325.

127. Okatani, T., Sekiguchi, S., Hane, K. et al. Surface-plasmon-coupled optical force sensors based on metal–insulator–metal metamaterials with movable air gap. *Sci Rep*. **2020**, *10*, 14807.

128. Zheng, G.G., Xu, L.H., Liu, Y.Z., Su, W. Optical filter and sensor based on plasmonic-gap-waveguide coupled with T-shaped resonators. International Journal for Light and Electron *Optics.* **2015**, *126*, 4056-4060.

129. Huang, Y., Zhu, J., Fan, J., Chen, Z., Chen, X., Jin, S., Wu, W., Plasmonic color generation and refractive index sensing with three-dimensional air-gap nanocavities. *Opt. Express.* **2019**, *27*, 6283-6299.

130. Kazanskiy, N.L., Khonina, S.N., Butt, M.A., Kaźmierczak, A., Piramidowicz, R. A Numerical Investigation of a Plasmonic Sensor Based on a Metal-Insulator-Metal Waveguide for Simultaneous Detection of Biological Analytes and Ambient Temperature. *Nanomaterials*. **2021**, *11*, 2551.

131. Wu, T., Liu, Y., Yu, Z., Ye, H., Peng, Y., Shu, C., et al., A nanometeric temperature sensor based on plasmonic waveguide with an ethanol-sealed rectangular cavity. *Optics Communications.* **2015**, 339, 1-6.

132. Bo, L., Claes, N., Ingemar, L., Surface plasmon resonance for gas detection and biosensing. *Sensors and Actuators.* **1983**, *4*, 299-304.

133. Zhou, H., Li, D. X., Hui, X. D., et al., Metamaterial Gas Sensing Platform Based on Surface-Enhanced Infrared Absorption. *2020 IEEE 33rd International Conference on Micro Electro Mechanical Systems (MEMS).* **2020**, 717-720.

134. Butt, M.A., Kazanskiy, N.L., Nanoblocks embedded in L-shaped nanocavity of a plasmonic sensor for best sensor performance. *Opt. Appl.* **2021**, *51*, 109–120.

135. Chao, C.-T., Chau, Y.-F.C., Huang, H., Kumara, N., Kooh, M., Lim, C., Chiang, H.-P. Highly sensitive and tunable plasmonic sensor based on a nanoring resonator with silver nanorods. *Nanomaterials* **2020**, *10*, 1399.

136. Jia, Z., Li, Z., Chen, J., High-sensitivity plasmonic sensor by narrowing Fano resonances in a tilted metallic nano-groove array. *Opt. Express* **2021**, *29*, 21358-21368.

137. Kristensen, A., Yang, J., Bozhevolnyi, S. et al. Plasmonic colour generation. *Nat. Rev. Mater.* **2017**, *2*, 16088.

138. Yokogawa, S., Burgos, S. P. & Atwater, H. A. Plasmonic color filters for CMOS image sensor applications. *Nano Lett.* **2012**,*12*, 4349–4354.

139. Jiang, H. and Kaminska, B., Scalable Inkjet-Based Structural Color Printing by Molding Transparent Gratings on Multilayer Nanostructured Surfaces. *ACS Nano.* **2018**, *12*, 3112–3125.

140. Franklin, D., Chen, Y., Vazquez-Guardado, A. et al. Polarization-independent actively tunable colour generation on imprinted plasmonic surfaces. *Nat. Commun.* **2015**, *6*, 733.

141. Song, Q., Baroni, A., Sawant, R. et al. Ptychography retrieval of fully polarized holograms from geometric-phase metasurfaces. *Nat. Commun.* **2020**, *11*, 2651.

142. Duan, X., Kamin, S. & Liu, N. Dynamic plasmonic colour display. *Nat Commun.* **2017**, *8*, 14606.

143. Hunt, R. W. G. & Pointer, M. R. Measuring Colour (*John Wiley & Sons, 2011*), **2011**.

144. Artar, A., Yanik, A. A. and Altug H. Fabry–Pérot nanocavities in multilayered plasmonic crystals for enhanced biosensing. *Appl. Phys. Lett.* **2009**, *95*, 051105.